PHYSICS OF COLLOIDAL DISPERSIONS IN NEMATIC LIQUID CRYSTALS

Holger STARK

ELSEVIER

AMSTERDAM – LONDON – NEW YORK – OXFORD – PARIS – SHANNON – TOKYO


ELSEVIER

Physics Reports 351 (2001) 387–474

PHYSICS REPORTS

www.elsevier.com/locate/physrep

Physics of colloidal dispersions in nematic liquid crystals

Holger Stark

Fachbereich Physik, Universität Konstanz, D-78457 Konstanz, Germany

Received December 2000; editor: M.L. Klein

Contents

Abstract

This article reviews the physics of colloidal dispersions in nematic liquid crystals as a novel challenging type of soft matter. We first investigate the nematic environment of one particle with a radial anchoring of the director at its surface. Three possible structures are identified and discussed in detail; the dipole, the Saturn-ring and the surface-ring configuration. Secondly, we address dipolar and quadrupolar two-particle

E-mail address: holger.stark@uni-konstanz.de (H. Stark).

0370-1573/01/$ - see front matter
PII: S0370-1573(00)00144-7

interactions with the help of a phenomenological theory. Thirdly, we calculate the anisotropic Stokes drag of a particle in a nematic environment which determines the Brownian motion of particles via the Stokes–Einstein relation. We then turn our interest towards colloidal dispersions in complex geometries where we identify the dipolar configuration and study its formation. Finally, we demonstrate that surface-induced nematic order above the nematic-isotropic phase transition results in a strongly attractive but short-range two-particle interaction. Its strength can be controlled by temperature and thereby induce flocculation in an otherwise stabilized dispersion.

PACS: 77.84.Nh; 61.30.Jf; 61.30.Cz; 82.70.Dd

Keywords: Colloidal dispersions; Nematic liquid crystals; Topological defects; Two-particle interactions; Stokes drag; Complex geometries; Flocculation

1. Motivation and contents

Dispersions of particles in a host medium are part of our everyday life and an important state of matter for fundamental research. One distinguishes between emulsions, where surfactant-coated liquid droplets are dispersed in a fluid environment, colloidal suspensions, where the particles are solid, and aerosols, with fluid or solid particles floating in a gaseous phase. Colloidal dispersions, whose particle size ranges from 10 nm to 10 μm, appear in food, with milk being the best-known fat-in-water emulsion, in drugs, cosmetics, paints, and ink. As such, they are of considerable technological importance. In nature, one is confronted by both the bothering and appealing side of fog, and one can look at the beautiful blue-greenish color of berg lakes in the Canadian Rockies, caused by light scattering from a fine dispersion of stone flower in water. The best-known example of an ordered colloid, a colloidal crystal, is the opal, formed from a uniform array of silica spheres compressed and fused over geological timescales. In fundamental research, colloidal dispersions are ideal systems to study Brownian motion and hydrodynamic interactions of suspended particles [202,110]. They provide model systems [134,89] for probing our understanding of melting and boiling, and for checking the Kosterlitz–Thouless–Halperin–Nelson–Young transition in two-dimensional systems [233,238,23]. The main interest in colloidal dispersions certainly focusses on the problem how to prevent the particles from flocculation, as stated by Russel, Saville and Schowalter [202]:

> Since all characteristics of colloidal systems change markedly in the transition from the dispersed to the aggregated state, the question of stability occupies a central position in colloid science.

There exists a whole zoo of interactions between the particles whose delicate balance determines the stability of a colloidal dispersion. Besides the conventional van der Waals, screened Coulombic, and steric interactions [202], fluctuation-induced Casimir forces (e.g., in binary fluids close to the critical point [116,157]) and depletion forces in binary mixtures of small and large particles [202,56,55,196] have attracted a lot of interest. Entropic effects play a major role in the three latter types of interactions. In a subtle effect, they also lead to an attraction between like-charged macroions [109,45,125] by Coulomb depletion [4].

The present work focusses on the interesting question of how particles behave when they are dispersed in a nematic solvent. In a nematic liquid crystal, rodlike organic molecules align on average along a unit vector $\boldsymbol{n}$, called director. The energetic ground state is a uniform director field throughout space. Due to the anchoring of the molecules at the surface of each particle, the surrounding director field is elastically distorted which induces additional long-range two-particle interactions. They are of dipolar or quadrupolar type, depending on the symmetry of the director configuration around a single particle [22,190,200,182,140]. The forces were confirmed by recent experiments in inverted nematic emulsions [182,179,183]. On the other hand, close to the suspended particles, topological point and line defects in the orientational order occur which strongly determine their behavior. For example, point defects give rise to a short-range repulsion [182,183]. Colloidal dispersions in a nematic environment are therefore an ideal laboratory for studying the statics and dynamics of topological defects.

Before we deal with the physics of such dispersions in the following, we review the phenomenological description of the nematic phase in Section 2. We introduce the total free energy

and the Ericksen–Leslie equations governing, respectively, the statics and dynamics of the director field. We also provide the basic knowledge of topological point and line defects in the orientational order necessary for the understanding of different director configurations around a single spherical particle. In Section 3 we review the work performed on colloidal dispersions in nematic liquid crystals relating it to recent developments in the liquid crystal field. Furthermore, with nematic emulsions, we introduce one particular model system which motivated the present investigation. In Section 4 we investigate, what I consider the paradigm for the understanding of nematic colloidal dispersions, i.e., the static properties of one particle. We concentrate on a radial anchoring of the director at its surface, for which we identify three different types of nematic environment; the dipole configuration, where the particle and a companion point defect form a tightly bound topological dipole, the Saturn-ring configuration, where the particle is surrounded by a ring defect and a structure with an equatorial surface ring, which appears for decreasing anchoring strength of the molecules at the surface of the particle. In Section 5 we address colloidal interactions with the help of a phenomenological theory and illustrate how they depend on the overall symmetry of the director configuration around a single particle. Then, in Section 6 we calculate the Stokes drag of one particle moving in a nematic environment. Via the Stokes–Einstein relation, one immediately has access to the diffusion constant which determines the Brownian motion of spherical objects. In Section 7 we turn our interest towards colloidal dispersions in complex geometries. In particular, we consider particles, e.g., droplets of water, in a large nematic drop. We identify the dipole configuration and illustrate possible dynamic effects in connection with its formation. Finally, in Section 8 we demonstrate that surface-induced nematic order above the nematic-isotropic phase transition leads to another novel colloidal interaction which strongly influences the stability of dispersions. It is easily controlled by temperature and can, e.g., induce flocculation in an otherwise stabilized system.

2. Phenomenological description of nematic liquid crystals

Typical liquid crystalline compounds consist of organic molecules. According to their elongated or disc-like shape one distinguishes between calamatic and discotic liquid crystals. Fig. 1a presents the molecular structure of the well-studied compound *N*-(*p*-methoxybenzylidene)-*p*-butylaniline (MBBA). Its approximate length and width are 20 and 5 Å. At sufficiently high temperatures, the liquid crystalline compound behaves like a conventional isotropic liquid; the molecules do not show any long-range positional and orientational order, as illustrated in the right box of Fig. 1b for rod-like molecules. Cooling below the clearing point T_c, the liquid becomes turbid, which indicates a phase transition to the liquid crystalline state. Finally, below the melting point T_m the system is solid. There exists a wealth of liquid crystalline phases [29,51,27]. Here we concentrate on the simplest, i.e., the nematic phase, which consists of non-chiral molecules. Their centers of mass are disordered as in the isotropic liquid, whereas their main axes align themselves on average parallel to each other, so that they exhibit a long-range orientational order. The average direction is given by a unit vector $\boldsymbol{n}$, called *Frank director*. However, $\boldsymbol{n}$ merely characterizes an axis in space, e.g., the optical axis of the birefringent nematic phase. As a result, all physical quantities, which we formulate in the following, have to be invariant under the inversion of the director ($\boldsymbol{n} \to -\boldsymbol{n}$). From the topological point

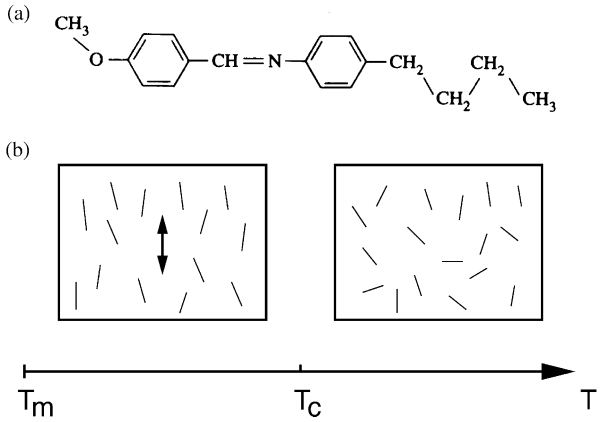

Fig. 1. (a) The compound MBBA. (b) The nematic liquid-crystalline phase below the clearing point T_c. The average direction of the molecules is indicated by the double arrow $\{\boldsymbol{n}, -\boldsymbol{n}\}$.

of view, the order parameter space of the nematic phase is the projective plane $P^2 = S^2/Z_2$, i.e., the unit sphere S^2 in three dimensions with opposite points identified [226]. Unlike the magnetization in ferromagnets, the nematic order parameter is not a vector. This statement can be understood from the following argument. Organic molecules often carry a permanent electric dipole moment along their main axis but so far no ferroelectric nematic phase with a spontaneous polarization has been found. Therefore, the same number of molecules that point into a certain direction in space also have to point into the opposite direction.

In *thermotropic* liquid crystals, the phase transitions are controlled by temperature. On the other hand, increasing the concentration of rod- or disc-like objects in a solvent can lead to the formation of what is called *lyotropic* liquid crystalline phases. The objects can be either large macromolecules, like the famous tobacco mosaic virus [78], or micelles, which form when amphiphilic molecules are dissolved, e.g., in water.

All directions in the isotropic fluid are equivalent. The phase transition to the nematic state breaks the continuous rotational symmetry of the isotropic liquid. As a result, domains with differently oriented directors appear like in a ferromagnet. These domains strongly scatter light and are one reason for the turbidity of the nematic phase. Hydrodynamic Goldstone modes appear in systems with a broken continuous symmetry [76,27]. They are "massless", i.e., their excitation does not cost any energy for vanishing wave number. In the nematic phase, the Goldstone modes correspond to thermal fluctuations of the director about its equilibrium value. Such fluctuations of the local optical axis also scatter light very strongly.

In the next four Sections 2.1–2.4 we will lay the basis for an understanding of the static and dynamical properties of the nematic phase, and we will apply it in the following sections to nematic colloidal dispersions. Sections 2.1 and 2.2 provide the necessary knowledge for determining the spatially non-uniform director field in complex geometries (e.g., around particles) under the influence of surfaces and external fields and in the presence of topological defects. Furthermore, with the help of the dynamic theory in Section 2.3, we will calculate the Stokes drag of a particle in a nematic environment, and we will demonstrate that it is influenced by

the presence of topological defects close to the particle. Finally, in Section 2.4 we will review the basic knowledge of point and line defects in nematics.

2.1. Free energy

Thermodynamics tells us that a complete knowledge of a system on a macroscopic level follows from the minimization of an appropriate thermodynamic potential [25]. We use the free energy, which consists of bulk and surface terms,

$$F_{\boldsymbol{n}} = F_{\rm el} + F_{24} + F_H + F_S = \int \mathrm{d}^3 r\,(f_{\rm el} + f_{24} + f_H) + \int \mathrm{d}S\, f_S\,, \tag{2.1}$$

and discuss them in order.

The energetic ground state of a nematic liquid crystal is a spatially uniform director field; any deviation from it costs elastic energy. To describe slowly varying spatial distortions of the director field $\boldsymbol{n}(\boldsymbol{r})$, one expands the free energy density into the gradient of $\boldsymbol{n}(\boldsymbol{r})$, $\nabla_i n_j$, up to second order, and demands that the energy density obeys the local point symmetry $D_{\infty h}$ of the nematic phase. The point group $D_{\infty h}$ contains all the symmetry elements of a cylinder, i.e., all rotations about an axis parallel to $\boldsymbol{n}(\boldsymbol{r})$, a mirror plane perpendicular to $\boldsymbol{n}(\boldsymbol{r})$, and an infinite number of two-fold axes also perpendicular to $\boldsymbol{n}(\boldsymbol{r})$. The result is the Oseen–Zöcher–Frank free energy density [167,242,79], which consists of two parts,

$$f_{\rm el} = \tfrac{1}{2}[K_1(\operatorname{div}\boldsymbol{n})^2 + K_2(\boldsymbol{n}\cdot\operatorname{curl}\boldsymbol{n})^2 + K_3(\boldsymbol{n}\times\operatorname{curl}\boldsymbol{n})^2] \tag{2.2}$$

and

$$f_{24} = -\frac{K_{24}}{2}\operatorname{div}(\boldsymbol{n}\operatorname{div}\boldsymbol{n} + \boldsymbol{n}\times\operatorname{curl}\boldsymbol{n})\,, \tag{2.3}$$

where K_1, K_2, K_3, and K_{24} denote, respectively, the *splay*, *twist*, *bend*, and *saddle-splay* elastic constants. Fig. 2 illustrates the characteristic deformations of the director field. The splay and bend distortions can be viewed, respectively, as part of a source or vortex field. In the twist deformation, the director rotates about an axis perpendicular to itself. In calamatic liquid crystals one usually finds the following relation, $K_3 \geqslant K_1 > K_2$. For example, in the compound pentylcyanobiphenyl (5CB), $K_1 = 0.42\times10^{-6}$ dyn, $K_2 = 0.23\times10^{-6}$ dyn, and $K_3 = 0.53\times10^{-6}$ dyn. In discotic liquid crystals, the relationship $K_2 > K_1 > K_3$ is predicted [216,168,221], which is in good agreement with experiments, where $K_2 \geqslant K_1 > K_3$ is observed [232,103].

The saddle-splay term is a pure divergence. It can be transformed into integrals over all surfaces of the system,

$$F_{24} = -\frac{1}{2}K_{24}\int \mathrm{d}\boldsymbol{S}\cdot(\boldsymbol{n}\operatorname{div}\boldsymbol{n} + \boldsymbol{n}\times\operatorname{curl}\boldsymbol{n})\,, \tag{2.4}$$

where it prefers the formation of a saddle (see Fig. 2). A Cauchy relation for K_{24} follows from the Maier–Saupe molecular approach [163],

$$K_{24} = (K_{11} + K_{22})/2\,. \tag{2.5}$$

Exact measurements of K_{24} are still missing but it is of the order of the bulk elastic constants K_1, K_2, and K_3 [41,5,40]. There is also the possibility of another surface term with a free

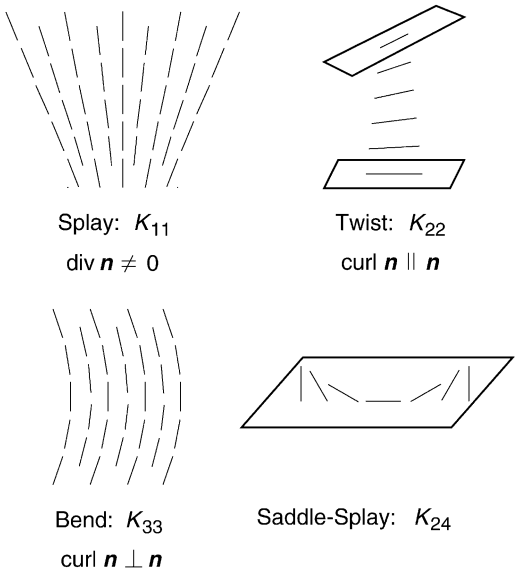

Fig. 2. Illustration of the characteristic deformations in a nematic liquid crystal: *splay*, *twist*, *bend*, and *saddle-splay*.

energy density $K_{13}\,\mathrm{div}(\boldsymbol{n}\,\mathrm{div}\,\boldsymbol{n})$, which we will not consider in this work [163,166,9,172,173]. The controversy about it seems to be solved [174].

In the one-constant approximation, $K = K_1 = K_2 = K_3$, the Frank free energy takes the form

$$F_{\mathrm{el}} = \frac{K}{2}\int \mathrm{d}^3 r(\nabla_i n_j)^2 + \frac{K - K_{24}}{2}\int \mathrm{d}\boldsymbol{S}\cdot(\boldsymbol{n}\,\mathrm{div}\,\boldsymbol{n} + \boldsymbol{n}\times\mathrm{curl}\,\boldsymbol{n})\,. \tag{2.6}$$

It is often used to obtain a basic understanding of a system without having to deal with effects due to the elastic anisotropy. The bulk term is equivalent to the non-linear sigma model in statistical field theory [241,27] or the continuum description of the exchange interaction in a ferromagnet [156].

In nematic liquid crystals we can assume a linear relation between the magnetization $\boldsymbol{M}$ and an external magnetic field $\boldsymbol{H}$, $\boldsymbol{M} = \boldsymbol{\chi}\boldsymbol{H}$, where $\boldsymbol{\chi}$ stands for the tensor of the magnetic susceptibility. The nematic phase represents a uniaxial system, for which the second-rank tensor $\boldsymbol{\chi}$ always takes the following form:

$$\boldsymbol{\chi} = \chi_\perp \mathbf{1} + \Delta\chi(\boldsymbol{n}\otimes\boldsymbol{n})\,; \tag{2.7}$$

$\mathbf{1}$ is the unit tensor, and $\otimes$ means dyadic product. We have introduced the magnetic anisotropy $\Delta\chi = \chi_\parallel - \chi_\perp$. It depends on the two essential magnetic susceptibilities $\chi_\parallel$ and $\chi_\perp$ for magnetic fields applied, respectively, parallel or perpendicular to the director. The general expression for the magnetic free energy density is $-\boldsymbol{H}\cdot\boldsymbol{\chi}\boldsymbol{H}/2$ [123]. A restriction to terms that depend on the director $\boldsymbol{n}$ yields

$$f_H = -\frac{\Delta\chi}{2}[(\boldsymbol{n}\cdot\boldsymbol{H})^2 - H^2]\,. \tag{2.8}$$

In usual nematics $\Delta\chi$ is positive and typically of the order of 10^{-7} [51]. For $\Delta\chi > 0$, the free energy density f_H favors an alignment of the director $\boldsymbol{n}$ parallel to $\boldsymbol{H}$. By adding a term

$-\Delta\chi H^2/2$ on the right-hand side of Eq. (2.8), we shift the reference point in order that the magnetic free energy of a completely aligned director field is zero. This will be useful in Section 4 where we calculate the free energy of the infinitely extended space around a single particle. The balance between elastic and magnetic torques on the director defines an important length scale, the magnetic coherence length

$$\xi_H = \sqrt{\frac{K_3}{\Delta\chi H^2}} \,. \tag{2.9}$$

Suppose the director is planarly anchored at a wall, and a magnetic field is applied perpendicular to it. Then ξ_H gives the distance from the wall that is needed to orient the director along the applied field [51]. The coherence length tends to infinity for $H \to 0$.

Finally, we employ the surface free energy of Rapini–Papoular to take into account the interaction of the director with boundaries:

$$f_S = \frac{W}{2}[1 - (\boldsymbol{n}\cdot\hat{\boldsymbol{v}})^2] \,. \tag{2.10}$$

The unit vector $\hat{\boldsymbol{v}}$ denotes some preferred orientation of the director at the surface, and W is the coupling constant. It varies in the range 10^{-4}–$1\,\mathrm{erg/cm^2}$ as reviewed by Blinov et al. [14]. In Section 4.3.4 we will give a lower bound of W for the interface of water and the liquid crystalline phase of 5CB in the presence of the surfactant sodium dodecyl sulfate, which was used in the experiment by Poulin et al. [182,183] on nematic emulsions. From a comparison between the Frank free energy and the surface energy one arrives at the extrapolation length [51]

$$\xi_S = \frac{K_3}{W} \,. \tag{2.11}$$

It signifies the strength of the anchoring. Take a particle of radius a in a nematic environment with an uniform director field at infinity. (We will investigate this case thoroughly in Section 4.) The Frank free energy of this system is proportional to $K_3 a$ whereas the surface energy scales as Wa^2. At *strong* anchoring, i.e., for $Wa^2 \gg K_3 a$ or $\xi_S \ll a$, the energy to turn the director away from its preferred direction $\hat{\boldsymbol{v}}$ at the whole surface would be much larger than the bulk energy. Therefore, it is preferable for the system that the director points along $\hat{\boldsymbol{v}}$. However, $\boldsymbol{n}$ can deviate from $\hat{\boldsymbol{v}}$ in an area of order $\xi_S a$. In Section 4.3.4 we will use this argument to explain a ring configuration around the particle. *Rigid* anchoring is realized for $\xi_S \to 0$. Finally, $\xi_S \gg a$ means *weak* anchoring, where the influence of the surface is minor. Since in our discussion we have always referred ξ_S to the radius a, it is obvious that the strength of the anchoring is not an absolute quantity but depends on characteristic length scales of the system.

2.2. Routes towards the director field

The director field $\boldsymbol{n}(\boldsymbol{r})$ in a given geometry follows from a minimization of the total free energy $F_{\boldsymbol{n}} = F_{\mathrm{el}} + F_{24} + F_H + F_S$ under the constraint that $\boldsymbol{n}$ is a unit vector:

$$\delta F_{\boldsymbol{n}} = 0 \quad \text{with } \boldsymbol{n}\cdot\boldsymbol{n} = 1 \,. \tag{2.12}$$

Even in the one-constant approximation and under the assumption of rigid anchoring of the director at the boundaries, this is a difficult problem to solve because of the additional constraint. Typically, full analytical solutions only exist for one-dimensional problems, e.g., for the description of the Fréedericksz transition [29,51], or in two dimensions when certain symmetries are assumed [140]. To handle the constraint, one can use a Lagrange parameter or introduce an appropriate parametrization for the director, e.g., a tilt (Θ) and twist (Φ) angle, so that the director in the local coordinate basis takes the form

$$\boldsymbol{n} = (\sin\Theta\cos\Phi, \sin\Theta\sin\Phi, \cos\Theta)\ . \tag{2.13}$$

If an accurate analytical determination of the director field is not possible, there are two strategies. First, an ansatz function is constructed that fulfils the boundary conditions and contains free parameters. Then, the director field follows from a minimization of the total free energy in the restricted space of functions with respect to the free parameters. In Section 4.2 we will see that this method is quite successful.

Secondly, one can look for numerical solutions of the Euler–Lagrange equations corresponding to the variational problem formulated in Eq. (2.12). They are equivalent to functional derivatives of $F_{\boldsymbol{n}}[\Theta, \Phi]$, where we use the tilt and twist angle of Eq. (2.13) to parametrize the director:

$$\frac{\delta F_{\boldsymbol{n}}}{\delta\Theta} = \frac{\delta F_{\boldsymbol{n}}}{\delta n_i}\frac{\partial n_i}{\partial\Theta} = 0\ , \tag{2.14}$$

$$\frac{\delta F_{\boldsymbol{n}}}{\delta\Phi} = \frac{\delta F_{\boldsymbol{n}}}{\delta n_i}\frac{\partial n_i}{\partial\Phi} = 0\ . \tag{2.15}$$

Einstein's summation convention over repeated indices is used. To arrive at the equations above for $\Theta(\boldsymbol{r})$ and $\Phi(\boldsymbol{r})$, we have employed a chain rule for functional derivatives [219]. These chain rules are useful in numerical problems since they allow to write the Euler–Lagrange equations, which can be quite complex, in a more compact form. For example, the bulk and surface equations that are solved in Section 4.3 could only be calculated with the help of the algebraic program Maple after applying the chain rules.

Typically, we take a starting configuration for the director field and relax it on a grid via the Newton–Gauss–Seidel method [187]. It is equivalent to Newton's iterative way of determining the zeros of a function but now generalized to functionals. We illustrate it here for the tilt angle Θ:

$$\Theta^{\mathrm{new}}(\boldsymbol{r}) = \Theta^{\mathrm{old}}(\boldsymbol{r}) - \frac{\delta F_{\boldsymbol{n}}/\delta\Theta(\boldsymbol{r})}{\text{“}\delta^2 F_{\boldsymbol{n}}/\delta\Theta^2(\boldsymbol{r})\text{”}}\ . \tag{2.16}$$

There are two possibilities to implement the method numerically. If the grid for the numerical investigation is defined by the coordinate lines, one determines the Euler–Lagrange equations analytically. Then, they are discretized by the method of finite differences for a discrete set of grid points $\boldsymbol{r}$ [187]. Finally, "$\delta^2 F_{\boldsymbol{n}}/\delta\Theta^2(\boldsymbol{r})$" is calculated as the derivative of $\delta F_{\boldsymbol{n}}/\delta\Theta(\boldsymbol{r})$ with respect to $\Theta(\boldsymbol{r})$ at the grid point $\boldsymbol{r}$. We put "$\delta^2 F_{\boldsymbol{n}}/\delta\Theta^2(\boldsymbol{r})$" into quotes because it is not the discretized form of a real second-order functional derivative, which would involve a delta function. If the geometry of the system is more complex, the method of finite elements is appropriate (see Section 7). In two dimensions, e.g., the integration area is subdivided into *finite elements*, which in the simplest case are triangles. In doing so, the boundaries of the complex geometry

are well approximated by polygons. The finite-element technique generally starts from an already discretized version of the total free energy F_n and then applies a numerical minimization scheme, e.g., the Newton–Gauss–Seidel method. Both the first and second derivatives in Eq. (2.16) are performed with respect to $\Theta(\boldsymbol{r})$ at the grid point $\boldsymbol{r}$.

2.3. Hydrodynamic equations

In the last subsection we concentrated on the static properties of the director field. In this subsection we review a set of dynamic equations coupling the flow of the liquid crystal to the dynamics of the Frank director. The set consists of a generalization of the Navier–Stokes equations for the fluid velocity $\boldsymbol{v}$ to uniaxial media and a dynamic equation for the director $\boldsymbol{n}$. We will not provide any detailed derivation of these equations, rather we will concentrate on the explanation of their meaning. The main problem is how to find a dynamic equation for the director. An early approach dates back to Oseen [167]. Ericksen [67–71] and Leslie [128,129] considered the liquid crystal as a Cosserat continuum [73] whose constituents possess not only translational but also orientational degrees of freedom. Based on methods of rational thermodynamics [72], they derived an equation for the fluid velocity from the balance law for momentum density and an equation for the director, which they linked to the balance law for angular momentum. The full set of equations is commonly referred to as the *Ericksen–Leslie equations*. An alternative approach is due to the Harvard group [77,27] which formulated equations following rigorously the ideas of hydrodynamics [76,27]. It only deals with hydrodynamic variables, i.e., densities of conserved quantities, like mass, momentum, and energy, or broken-symmetry variables. Each one obeys a conservation law. As a result, hydrodynamic modes exist whose, in general, complex frequencies become zero for vanishing wave number. Excitations associated with broken-symmetry variables are called hydrodynamic *Goldstone* modes according to a concept introduced by Goldstone in elementary particle physics [92,93]. The director is such a variable that breaks the continuous rotational symmetry of the isotropic fluid. In a completely linearized form the Ericksen–Leslie equations and the equations of the Harvard group are identical.

In the following, we review the Ericksen–Leslie equations and explain them step by step. In a symbolic notation, they take the form [29,51]

$$0 = \operatorname{div} \boldsymbol{v} \,, \tag{2.17}$$

$$\varrho \frac{\mathrm{d}\boldsymbol{v}}{\mathrm{d}t} = \operatorname{div} \boldsymbol{T} \quad \text{with } \boldsymbol{T} = -p\mathbf{1} + \boldsymbol{T}^0 + \boldsymbol{T}' \,, \tag{2.18}$$

$$\mathbf{0} = \boldsymbol{n} \times (\boldsymbol{h}^0 - \boldsymbol{h}') \,, \tag{2.19}$$

where the divergence of the stress tensor is defined by $(\operatorname{div} \boldsymbol{T})_i = \nabla_j T_{ij}$. The first equation states that we consider an incompressible fluid. We also assume constant temperature in what follows. The third equation balances all the torques on the director. We will discuss it below. The second formula stands for the generalized Navier–Stokes equations. Note that

$$\frac{\mathrm{d}}{\mathrm{d}t} = \frac{\partial}{\partial t} + \boldsymbol{v} \cdot \operatorname{grad} \tag{2.20}$$

means the total or material time derivative as experienced by a moving fluid element. It includes the *convective* part $\boldsymbol{v}\cdot\mathrm{grad}$. Besides the pressure p, the stress tensor consists of two terms:

$$T^0_{ij} = -\frac{\partial f_b}{\partial \nabla_j n_k}\nabla_i n_k \quad \text{with } f_b = f_{\mathrm{el}} + f_{24} + f_m \,, \tag{2.21}$$

$$T'_{ij} = \alpha_1 n_i n_j n_k n_l A_{kl} + \alpha_2 n_j N_i + \alpha_3 n_i N_j + \alpha_4 A_{ij} + \alpha_5 n_j n_k A_{ik} + \alpha_6 n_i n_k A_{jk} \,. \tag{2.22}$$

In addition to p, $\boldsymbol{T}^0$ introduces a second, anisotropic contribution in the static stress tensor. It is due to elastic distortions in the director field, where f_b denotes the sum of all free energy densities introduced in Section 2.1. The quantity $\boldsymbol{T}'$ stands for the viscous part of the stress tensor. In isotropic fluids, it is simply proportional to the symmetrized gradient of the velocity field,

$$A_{ij} = \tfrac{1}{2}(\nabla_i v_j + \nabla_j v_i) \,. \tag{2.23}$$

The conventional shear viscosity equals $\alpha_4/2$ in Eq. (2.22). The uniaxial symmetry of nematic liquid crystals allows for further contributions proportional to $\boldsymbol{A}$ which contain the director $\boldsymbol{n}$. There are also two terms that depend on the time derivative of the director $\boldsymbol{n}$, i.e., the second dynamic variable,

$$\boldsymbol{N} = \frac{\mathrm{d}\boldsymbol{n}}{\mathrm{d}t} - \boldsymbol{\omega}\times\boldsymbol{n} \quad \text{with } \boldsymbol{\omega} = \tfrac{1}{2}\mathrm{curl}\,\boldsymbol{v} \,. \tag{2.24}$$

The vector $\boldsymbol{N}$ denotes the rate of change of $\boldsymbol{n}$ relative to the fluid motion, or more precisely, relative to a local fluid vortex characterized by the angular velocity $\boldsymbol{\omega} = \mathrm{curl}\,\boldsymbol{v}/2$. The viscosities $\alpha_1,\ldots,\alpha_6$ are referred to as the Leslie coefficients. We will gain more insight into $\boldsymbol{T}'$ at the end of this subsection.

Finally, Eq. (2.19) demands that the total torque on the director due to elastic distortions in the director field ($\boldsymbol{h}^0$) and due to viscous processes ($\boldsymbol{h}'$) is zero. The elastic and viscous curvature forces are

$$h^0_i = \nabla_j \frac{\partial f_b}{\partial \nabla_j n_i} - \frac{\partial f_b}{\partial n_i} \,, \tag{2.25}$$

$$h'_i = \gamma_1 N_i + \gamma_2 A_{ij} n_j \quad \text{with } \gamma_1 = \alpha_3 - \alpha_2 \text{ and } \gamma_2 = \alpha_2 + \alpha_3 \,. \tag{2.26}$$

De Gennes calls $\boldsymbol{h}^0$ a molecular field reminiscent to a similar quantity in magnetism [51]. In Eq. (2.19) the curvature force $\boldsymbol{h}^0 - \boldsymbol{h}'$ is only defined within an additive expression $\lambda(\boldsymbol{r},t)\boldsymbol{n}(\boldsymbol{r},t)$. It has the meaning of a Lagrange-multiplier term, and $\lambda(\boldsymbol{r},t)$ is to be determined by the condition that the director is normalized to unity. In static equilibrium, we obtain $\boldsymbol{h}^0(\boldsymbol{r}) + \lambda(\boldsymbol{r})\boldsymbol{n}(\boldsymbol{r}) = 0$, i.e., the Euler–Lagrange equation in the bulk which follows from minimizing the total free energy $F_{\boldsymbol{n}}$ introduced in Section 2.1. One can easily show that the saddle-splay energy f_{24} does not contribute to $\boldsymbol{h}^0$. The first term of the viscous curvature force $\boldsymbol{h}'$ describes the viscous process due to the rotation of neighboring molecules with different angular velocities. The coefficient γ_1 is, therefore, a typical rotational viscosity. The second term quantifies torques on the director field exerted by a shear flow. An inertial term for the rotational motion of the molecules is not included in Eq. (2.19). One can show that it is of no relevance for the timescales of

micro-seconds or larger. In the approach of the Harvard group, it does not appear since it results in a non-hydrodynamic mode.

The energy dissipated in viscous processes follows from the entropy production rate

$$T\frac{\mathrm{d}S}{\mathrm{d}t} = \int (\boldsymbol{T}' \cdot \boldsymbol{A} + \boldsymbol{h}' \cdot \boldsymbol{N})\, \mathrm{d}^3 r \,, \tag{2.27}$$

where T is temperature, and S is entropy. The first term describes dissipation by shear flow and the second one dissipation by rotation of the director. Each term in the entropy production rate is always written as a product of a generalized flux and its conjugate force. The true conjugate force to the flux $\boldsymbol{A}$ is the symmetrized viscous stress tensor $T'^{\mathrm{sym}}_{ij} = (T'_{ij} + T'_{ji})/2$. The flux $\boldsymbol{N}$ is conjugate to the generalized force $\boldsymbol{h}'$. Note, that $\boldsymbol{h}'$ corresponds to the dual form of the antisymmetric part of $\boldsymbol{T}'$, i.e., $h'_i = \varepsilon_{ijk}(T'_{jk} - T'_{kj})/2$. The Harvard group calls $\boldsymbol{T}'^{\mathrm{sym}}$ and $\boldsymbol{h}'$ fluxes since they appear in the currents of the respective balance laws for momentum and director [77,27]. In hydrodynamics the viscous forces are assumed to be small, and they are written as linear functions of all the fluxes:

$$\begin{pmatrix} \boldsymbol{T}'^{\mathrm{sym}} \\ \boldsymbol{h}' \end{pmatrix} = \boldsymbol{\Gamma} \begin{pmatrix} \boldsymbol{A} \\ \boldsymbol{N} \end{pmatrix} \,. \tag{2.28}$$

The matrix $\boldsymbol{\Gamma}$ must be compatible with the uniaxial symmetry of the nematic phase, and it must be invariant when $\boldsymbol{n}$ is changed into $-\boldsymbol{n}$. Furthermore, it has to obey Onsager's theorem [52], which demands a symmetric matrix $\boldsymbol{\Gamma}$ for zero magnetic field. Fulfilling all these requirements results in Eqs. (2.22) and (2.26). One additional, important Onsager relation is due to Parodi [170]:

$$\alpha_2 + \alpha_3 = \alpha_6 - \alpha_5 \,. \tag{2.29}$$

It reduces the number of independent viscosities in a nematic liquid crystal to five. The Leslie coefficients of the compound 5CB are [39]

$$\begin{aligned} &\alpha_1 = -0.111\,\mathrm{P}, \quad \alpha_2 = -0.939\,\mathrm{P}, \quad \alpha_3 = -0.129\,\mathrm{P}\,, \\ &\alpha_4 = 0.748\,\mathrm{P}, \quad \alpha_5 = 0.906\,\mathrm{P}, \quad \alpha_6 = -0.162\,\mathrm{P}\,. \end{aligned} \tag{2.30}$$

At the end, we explain two typical situations that help to clarify the meaning of the possible viscous processes in a nematic and how they are determined by the Leslie coefficients. In the first situation we perform typical shear experiments as illustrated in Fig. 3. The director field between the plates is spatially uniform, and the upper plate is moved with a velocity v_0 relative to the lower one. There will be a constant velocity gradient along the vertical z direction. Three simple geometries exist with a symmetric orientation of the director; it is either parallel to the velocity field $\boldsymbol{v}$, or perpendicular to $\boldsymbol{v}$ and its gradient, or perpendicular to $\boldsymbol{v}$ and parallel to its gradient. The director can be firmly aligned in one direction by applying a magnetic field strong enough to largely exceed the viscous torques. For all three cases, the shear forces T' per unit area are calculated from the stress tensor $\boldsymbol{T}'$ of Eq. (2.22), yielding $T' = \eta_i v_0/d$, where d is the separation between the plates. The viscosities as a function of the Leslie coefficients for all three cases are given in Fig. 3. They are known as *Mięsowicz* viscosities after the scientist who first measured them [150,151]. If one chooses a non-symmetric orientation for the director, the viscosity α_1 is accessible in shear experiments too [84].

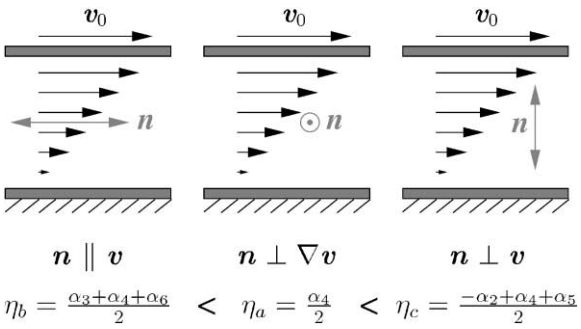

Fig. 3. Definition of the three Mięsowicz viscosities in shear experiments.

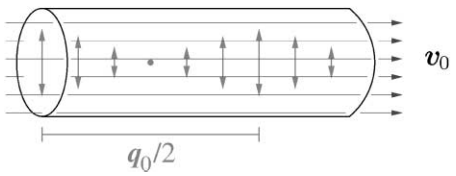

Fig. 4. Permeation of a fluid through a helix formed by the nematic director.

The second situation describes a Gedanken experiment illustrated in Fig. 4 [102]. Suppose the nematic director forms a helical structure with wave number q_0 inside a capillary. Such a configuration is found in cholesteric liquid crystals that form when the molecules are chiral. Strictly speaking, the hydrodynamics of a cholesteric is more complicated than the one of nematics [139]. However, for what follows we can use the theory formulated above. We assume that the velocity field in the capillary is spatially uniform and that the helix is not distorted by the fluid flow. Do we need a pressure gradient to press the fluid through the capillary, although there is no shear flow unlike a Poiseuille experiment? The answer is yes since the molecules of the fluid, when flowing through the capillary, have to rotate constantly to follow the director in the helix, which determines the average direction of the molecules. The dissipated energy follows from the second term of the entropy production rate in Eq. (2.27). The rate of change, $\boldsymbol{N} = \boldsymbol{v}_0 \cdot \operatorname{grad} \boldsymbol{n}$, is non-zero due to the convective time derivative. The energy dissipated per unit time and unit volume has to be matched by the work per unit time performed by the pressure gradient p'. One finally arrives at

$$p' = \gamma_1 q_0^2 v_0 \ . \tag{2.31}$$

Obviously, the Gedanken experiment is determined by the rotational viscosity γ_1. It was suggested by Helfrich [102] who calls the motion through a fixed orientational pattern *permeation*. This motion is always dissipative because of the rotational viscosity of the molecules which have to follow the local director.

Of course, the Gedanken experiment is not suitable for measuring γ_1. A more appropriate method is dynamic light scattering from director fluctuations [99,29]. Together with the shear experiments it is in principle possible to measure all five independent viscosities of a nematic liquid crystal.

2.4. Topological defects

Topological defects [111,146,226,27], which are a necessary consequence of broken continuous symmetry, exist in systems as disparate as superfluid helium 3 [230] and 4 [235], crystalline solids [224,81,160], liquid crystals [30,121,127], and quantum-Hall fluids [204]. They play an important if not determining role in such phenomena as response to external stresses [81,160], the nature of phase transitions [27,164,222], or the approach to equilibrium after a quench into an ordered phase [21]; and they are the primary ingredient in such phases of matter as the Abrikosov flux-lattice phase of superconductors [1,13] or the twist-grain-boundary phase of liquid crystals [193,94,95]. They even arise in certain cosmological models [34]. Topological defects are points, lines or walls in three-dimensional space where the order parameter of the system under consideration is not defined. The theory of homotopy groups [111,146,226,27] provides a powerful tool to classify them. To identify, e.g., line defects, homotopy theory considers closed loops in real space which are mapped into closed paths in the order parameter space. If a loop can be shrunk continuously to a single point, it does not enclose a defect. All other loops are divided into classes of paths which can be continuously transformed into each other. Then, each class stands for one type of line defect. All classes together, including the shrinkable loops, form the *first homotopy* or *fundamental group*. The group product describes the combination of defects. In the case of point singularities, the loops are replaced by closed surfaces, and the defects are classified via the *second homotopy group*.

In the next two subsections we deal with line and point defects in nematic liquid crystals whose order parameter space is the projective plane $P^2 = S^2/Z_2$, i.e., the unit sphere S^2 with opposite points identified. They play a determining role for the behavior of colloidal dispersions in a nematic environment. There exist several good reviews on defects in liquid crystals [111,146,226,27,30,121,127]. We will therefore concentrate on facts which are necessary for the understanding of colloidal dispersions. Furthermore, rather than being very formal, we choose a descriptive path for our presentation.

2.4.1. Line defects = disclinations

Line defects in nematic liquid crystals are also called *disclinations*. Homotopy theory tells us that the fundamental group $\pi_1(P^2)$ of the projective plane P^2 is the two-element group Z_2. Thus, there is only one class of stable disclinations. Fig. 5 presents two typical examples. The defect line with the core is perpendicular to the drawing plane. The disclinations carry a winding number of strength $+$ or $-1/2$, indicating a respective rotation of the director by $+$ or $-360^\circ/2$ when the disclination is encircled in the anticlockwise direction (see left part of Fig. 5). Note that the sign of the winding number is not fixed by the homotopy group. Both types of disclinations are topologically equivalent since there exists a continuous distortion of the director field which transforms one type into the other. Just start from the left disclination in Fig. 5 and rotate the director about the vertical axis through an angle π when going outward from the core in any radial direction. You will end up with the right picture. The line defects in Fig. 5 are called *wedge* disclinations. In a Volterra process [111,27] a cut is performed so that its limit, the disclination line, is perpendicular to the spatially uniform director field. Then the surfaces of the cut are rotated with respect to each other by an angle of $2\pi S$ about the disclination line, and material is either filled in ($S = +1/2$) or removed ($S = -1/2$). In *twist*

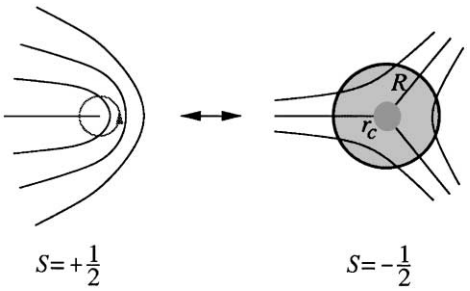

Fig. 5. Disclinations of winding number $\pm 1/2$. For further explanations see text.

disclinations the surfaces are rotated by an angle of π about an axis perpendicular to the defect line. Disclinations of strength $\pm 1/2$ do not exist in a system with an vector order parameter since it lacks the inversion symmetry of the nematic phase with respect to the director. In addition, one finds $\pi_1(S^2) = 0$, i.e., every disclination line of integral strength in a ferromagnet is unstable; "it escapes into the third dimension". The same applies to nematic liquid crystal as demonstrated by Cladis et al. [35,236] and Bob Meyer [149] for $S = 1$.

The director field around a disclination follows from the minimization of the Frank free energy (2.6) [111,29,51]. In the one-constant approximation the line energy F_d of the disclination can be calculated as

$$F_d = \frac{\pi}{4} K \left(\frac{1}{2} + \ln \frac{R}{r_c} \right) . \tag{2.32}$$

The surface term in Eq. (2.6) is neglected. The second term on the right-hand side of Eq. (2.32) stands for the elastic free energy per unit length around the line defect where R is the radius of a circular cross-section of the disclination (see Fig. 5). Since the energy diverges logarithmically, one has to introduce a lower cut-off radius r_c, i.e., the radius of the disclination core. Its line energy, given by the first term, is derived in the following way [111]. One assumes that the core of the disclination contains the liquid in the isotropic state with a free energy density ε_c necessary to melt the nematic order locally. Splitting the line energy of the disclination as in Eq. (2.32) into the sum of a core and elastic part, $F_d = \pi r_c^2 \varepsilon_c + K\pi \ln(R/r_c)/4$, and minimizing it with respect to r_c, results in

$$\varepsilon_c = \frac{K}{8} \frac{1}{r_c^2} , \tag{2.33}$$

so that we immediately arrive at Eq. (2.32). The right-hand side of Eq. (2.33) is equivalent to the Frank free energy density of the director field at a distance r_c from the center of the disclination. Thus r_c is given by the reasonable demand that the nematic state starts to melt when this energy density equals ε_c. With an estimate $\varepsilon_c = 10^{-7}\,\mathrm{erg/cm^3}$, which follows from a description of the nematic-isotropic phase transition by the Landau–de Gennes theory [126], and $K = 10^{-6}\,\mathrm{dyn}$, we obtain a core radius r_c of the order of 10 nm. In the general case ($K_1 \neq K_2 \neq K_3$), an analytical expression for the elastic free energy does not exist. However,

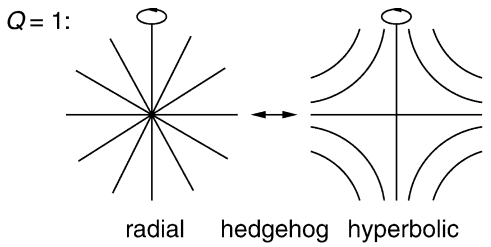

Fig. 6. Radial and hyperbolic hedgehog of point charge $Q = 1$.

a rough approximation for the core energy per unit length, F_c, can be found by averaging over the Frank constants:

$$F_c = \frac{\pi}{8}\frac{K_1 + K_2 + K_3}{3} . \tag{2.34}$$

In Section 4.3 we will make use of this form for F_c.

A more refined model of the disclination core is derived from Landau–de Gennes theory [48,96,212], which employs a traceless second-rank tensor $\boldsymbol{Q}$ as an order parameter (see Section 8.1). The tensor also describes biaxial liquid crystalline order. Investigations show that the core of a disclination should indeed be biaxial [141,144,207], with a core radius of the order of the biaxial correlation length ξ_b, i.e., the length on which deviations from the uniaxial order exponentially decay to zero. Outside of the disclination core, the nematic order is essentially uniaxial. Therefore, the line energy of a disclination is still given by Eq. (2.32) with $r_c \sim \xi_b$, and with a core energy now determined by the energy difference between the biaxial and uniaxial state rather than the energy difference between the isotropic and nematic state.

2.4.2. Point defects

Fig. 6 presents typical point defects in a nematic liquid crystal known as *radial* and *hyperbolic hedgehogs*. Both director fields are rotationally symmetric about the vertical axis. The second homotopy group $\pi_2(P^2)$ of the projective plane P^2 is the set Z of all integer numbers. They label every point defect by a topological charge Q. The result is the same as for the vector order parameter space S^2 since close to the point singularity the director field constitutes a unique vector field. For true vectors it is possible to distinguish between a radial hedgehog of positive and negative charge depending on their vector field that can either represent a source or a sink. In a nematic liquid crystal this distinction is not possible because $\boldsymbol{n}$ and $-\boldsymbol{n}$ describe the same state. Note, e.g., that the directors close to a point defect are reversed if the defect is moved around a $\pm 1/2$ disclination line. Therefore, the sign of the charge Q has no meaning in nematics, and by convention it is chosen positive. The charge Q is determined by the number of times the unit sphere is wrapped by all the directors on a surface enclosing the defect core. An analytical expression for Q is

$$Q = \left| \frac{1}{8\pi} \int \mathrm{d}S_i \, \varepsilon_{ijk} \boldsymbol{n} \cdot (\nabla_j \boldsymbol{n} \times \nabla_k \boldsymbol{n}) \right| , \tag{2.35}$$

where the integral is over any surface enclosing the defect core. Both the hedgehogs in Fig. 6 carry a topological charge $Q=1$. They are topologically equivalent since they can be transformed

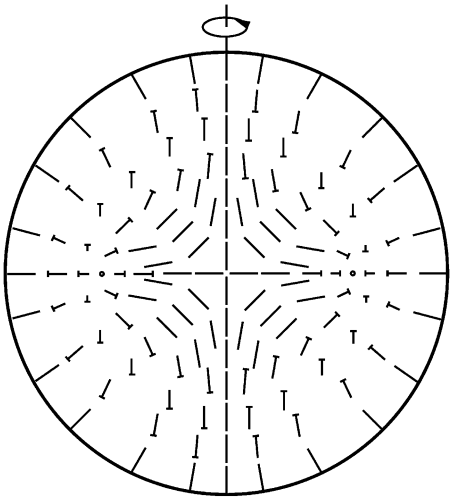

Fig. 7. The hyperbolic hedgehog at the center is transformed into a radial point defect by a continuous distortion of the director field. Nails indicate directors tilted relative to the drawing plane.

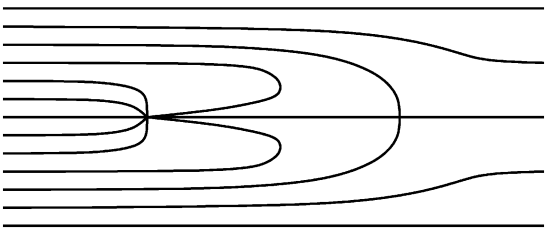

Fig. 8. A radial (left) and a hyperbolic (right) hedgehog combine to a configuration with total charge $0 = |1 - 1|$.

into each other by a continuous distortion of the director field. Just start from the hyperbolic hedgehog and rotate the director about the vertical axis through an angle π when going outward from the core in any radial direction. By this procedure, which is illustrated in Fig. 7 with the help of a nail picture, we end up with a radial hedgehog. The length of the nail is proportional to the projection of the director on the drawing plane, and the head of the nail is below the plane. Such a transition was observed by Lavrentovich and Terentjev in nematic drops with homeotropic, i.e., perpendicular anchoring of the director at the outer surface [126].

In systems with vector symmetry, the combined topological charge of two hedgehogs with respective charges Q_1 and Q_2 is simply the sum $Q_1 + Q_2$. In nematics, where the sign of the topological charge has no meaning, the combined topological charge of two hedgehogs is either $|Q_1 + Q_2|$ or $|Q_1 - Q_2|$.

It is impossible to tell with certainty which of these possible charges is the correct one by looking only at surfaces enclosing the individual hedgehogs. For example, the combined charge of two hedgehogs in the presence of a line defect depends on which path around the disclination the point defects are combined [226]. In Fig. 8 we illustrate how a radial and a hyperbolic hedgehog combine to a configuration with total charge $0 = |1 - 1|$. Since the distance

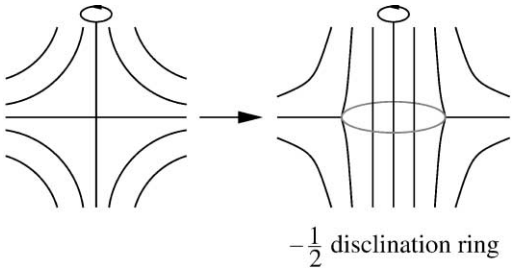

Fig. 9. A hyperbolic hedgehog can be opened up to a $-1/2$ disclination ring.

d of the defects is the only length scale in the system, dimensional arguments predict an interaction energy proportional to Kd [169]. It grows linear in d reminiscent to the interaction energy of quarks if one tries to separate them beyond distances larger than the diameter of a nucleus.

The energies of the hedgehog configurations, shown in Fig. 6, are easily calculated from the Frank free energy $F_{el}+F_{24}$ [see Eqs. (2.2) and (2.3)]. The director fields of these configurations are $\boldsymbol{n}=(x,y,z)/r$ for the radial and $\boldsymbol{n}=(-x,-y,z)/r$ for the hyperbolic hedgehog, where $\boldsymbol{r}=(x,y,z)$ and $r=|\boldsymbol{r}|$. In a spherical region of radius R with free boundary conditions at the outer surface, we obtain for their respective energies:

$$F_{\text{radial}} = 4\pi(2K_1 - K_{24})R \to 4\pi(2K - K_{24})R\,,$$
$$F_{\text{hyper}} = \frac{4\pi}{15}(6K_1 + 4K_3 + 5K_{24})R \to \frac{4\pi}{3}(2K + K_{24})R\,, \tag{2.36}$$

where the final expressions apply to the case of equal Frank constants. When $K_{24}=0$, these energies reduce to those calculated in Ref. [126]. Note that the Frank free energy of point defects does not diverge in contrast to the distortion energy of disclinations in the preceding subsection. The hyperbolic hedgehog has lower energy than the radial hedgehog provided $K_3 < 6K_1 - 5K_{24}$ or $K > K_{24}$ for the one-constant approximation. Thus, if we concentrate on the bulk energies, i.e., $K_{24}=0$, the hyperbolic hedgehog is always energetically preferred, since K_1 is always of the same order as K_3. This seems to explain the observation of Lavrentovich and Terentjev, already mentioned [126], who found the configuration illustrated in Fig. 7 in a nematic drop with radial boundary conditions at the outer surface. However, a detailed explanation has to take into account the Frank free energy of the strongly twisted transition region between hyperbolic and radial hedgehog [126]. In Section 7.4 we will present a linear stability analysis for the radial hedgehog against twisting. In terms of the Frank constants, it provides a criterion for the twist transition to take place, and its shows that the twisting starts close to the defect core. If, in addition to the one-constant approximation, K_{24} also fulfils the Cauchy relation (2.5), i.e., $K=K_{24}$, the energies of the two hedgehog configurations in Eqs. (2.36) are equal, as one could have predicted from Eq. (2.6), which is then invariant with respect to rigid rotations of even a spatially varying $\boldsymbol{n}$.

The twisting of a hedgehog in a nematic drop takes place at a length scale of several microns [26,126,182]. However, point defect also possess a fine structure at smaller length scales, which has attracted a lot of attention. Fig. 9 illustrates how a hyperbolic hedgehog opens up to a $-1/2$

disclination ring by filling in vertical lines of the director field. The farfield of the disclination ring is still given by the hedgehog so that the ring can be assigned the same topological point charge $Q = 1$. Similarly, a radial point defect is topologically equivalent to a $1/2$ disclination ring. Mineev pointed out that the characterization of a ring defect requires two parameters; the index of the line and the charge of the point defect [152]. The classification of ring defects within homotopy theory was developed by Garel [86] and Nakanishi et al. [161]. It can be asked whether it is energetically favorable for a hedgehog to open up to a disclination ring [155,225]. One can obtain a crude estimate of the radius R_0 of the disclination ring with the help of Eqs. (2.32) and (2.36) for disclination and hedgehog energies. When $R_0 \gg r_c$, the director configuration of a charge 1 disclination ring is essentially that of a simple disclination line, discussed in the previous subsection. It extends up to distances of order R_0 from the ring center. Beyond this radius, the director configuration is approximately that of a hedgehog (radial or hyperbolic). Thus, we can estimate the energy of a disclination ring of radius R_0 centered in a spherical region of radius R to be

$$F_{\text{ring}} \approx 2\pi R_0 \left[\frac{\pi}{4} K \left(\frac{1}{2} + \ln\frac{R_0}{r_c}\right)\right] + 8\pi\alpha K(R - R_0) \,, \tag{2.37}$$

where $\alpha = 1$ for a radial hedgehog and $\alpha = 1/3$ for a hyperbolic hedgehog. We also set $K_{24} = 0$. Minimizing over R_0, we find

$$R_0 = r_c \exp\left[\frac{16}{\pi}\left(\alpha - \frac{3\pi}{32}\right)\right] \,. \tag{2.38}$$

Though admittedly crude, this approximation yields a result that has the same form as that calculated in Refs. [155,225] using a more sophisticated ansatz for the director field. It has the virtue that it applies to both radial and hyperbolic far-field configurations. It predicts that the core of a radial hedgehog should be a ring with radius $R_0 \approx r_c e^{3.6}$, or $R_0 \approx 360\,\text{nm}$ for $r_c \approx 100\,\text{Å}$. The core of the hyperbolic hedgehog, on the other hand, will be a point rather than a ring because $R_0 \approx r_c e^{-0.2} \approx r_c$.

As in the case of disclinations, more refined models of the core of a point defect use the Landau–de Gennes free energy, which employs the second-rank tensor $\boldsymbol{Q}$ as an order parameter. Schopohl and Sluckin [208] chose a uniaxial $\boldsymbol{Q}$ but allowed the degree of orientational order, described by the Maier–Saupe parameter S [29,51], to continuously approach zero at the center of the defect. A stability analysis of the Landau–de Gennes free energy demonstrates that the radial hedgehog is either metastable or unstable against biaxial perturbations in the order parameter depending on the choice of the temperature and elastic constants [195,88]. Penzenstadler and Trebin modeled a biaxial defect core [171]. They found that the core radius is of the order of the biaxial correlation length ξ_b, which for the compound MBBA gives approximately 25 nm. This is an order of magnitude smaller than the estimate above. The reason might be that the ansatz function used by Penzenstadler and Trebin does not include a biaxial disclination ring. Such a ring encircles a region of uniaxial order, as illustrated in the right part of Fig. 9, and it possesses a biaxial disclination core. Numerical studies indicate the existence of such a ring [218,87] but a detailed analysis of the competition between a biaxial core and a biaxial disclination ring is still missing. We expect that Eq. (2.37) for a disclination ring and therefore Eq. (2.38) for its radius can be justified within the Landau–de Gennes theory for $R_0 \gg r_c \sim \xi_b$.

However, the Frank elastic constant and the core energy will be replaced by combinations of the Landau parameters. Since the ring radius R_0 varies exponentially with the elastic constants and the core energy, and since r_c is only roughly defined, it is very difficult to predict with certainty even the order of magnitude of R_0. Further investigations are needed.

3. Nematic colloidal dispersions

In this section we first give a historic account of the topic relating it to recent developments in the liquid crystal field and reviewing the work performed on colloidal dispersions in nematic liquid crystals. Then, with nematic emulsions, we introduce one particular model system for such colloidal dispersions.

3.1. Historic account

Liquid crystal emulsions, in which surfactant-coated drops, containing a liquid crystalline material, are dispersed in water, have been a particularly fruitful medium for studying topological defects for thirty years [147,61,26,126,121,60]. The liquid crystalline drops typically range from 10 to 50 μm in diameter and are visible under a microscope. Changes in the Frank director $\boldsymbol{n}$ are easily studied under crossed polarizers. The isolated drops in these emulsions provide an idealized spherical confining geometry for the nematic phase. With the introduction of polymer-dispersed liquid crystals as electrically controllable light shutters [58,60], an extensive study of liquid crystals confined to complex geometries, like distorted drops in a polymer matrix or a random porous network in silica aerogel, was initiated [60,44].

Here, we are interested in the inverse problem that is posed by particles suspended in a nematic solvent. Already in 1970, Brochard and de Gennes studied a suspension of magnetic grains in a nematic phase and determined the director field far away from a particle [22]. The idea was to homogeneously orient liquid crystals with a small magnetic anisotropy by a reasonable magnetic field strength through the coupling between the liquid-crystal molecules and the grains. The idea was realized experimentally by two groups [31,75]. However, even in the highly dilute regime the grains cluster. Extending Brochard's and de Gennes' work, Burylov and Raikher studied the orientation of an elongated particle in a nematic phase [24]. Chaining of bubbles or microcrystallites was used to visualize the director field close to the surface of liquid crystals [191,36]. A bistable liquid crystal display was introduced based on a dispersion of agglomerations of silica spheres in a nematic host [62,118,117,91]. The system was called *filled nematics*. Chains and clusters were observed in the dispersion of latex particles in a lyotropic liquid crystal [181,188,189]. The radii of the particles were 60 and 120 nm. Therefore, details of the director field could not be resolved under the polarizing microscope.

Terentjev et al. [225,119,201,213] started to investigate the director field around a sphere by both analytical and numerical methods, first concentrating on the Saturn-ring and surface-ring configuration. Experiments of Philippe Poulin and coworkers on inverted nematic emulsions, which we describe in the following subsection, clearly demonstrated the existence of a dipolar structure formed by a water droplet and a companion hyperbolic hedgehog [182,179,183,184]. A similar observation at a nematic-isotropic interface was made by Bob Meyer in 1972 [148].

Lately, Poulin et al. [180] were able to identify the dipolar structure in suspensions of latex particles and they could observe an equatorial ring configuration in the weak-anchoring limit of nematic emulsions [153]. In a very recent paper, Gu and Abbott reported Saturn-ring configurations around solid microspheres [97]. Particles in contact with the glass plates of a cell were studied in Ref. [98]. Lubensky, Stark, and coworkers presented a thorough analytical and numerical analysis of the director field around a spherical particle [182,140,219]. It is discussed in Section 4. Ramaswamy et al. [190] and Ruhwandl and Terentjev [200] determined the long-range quadrupolar interaction of particles surrounded by a ring disclination, whereas Lubensky et al. addressed both dipolar and quadrupolar forces [140] (see Section 5). Recently, Lev and Tomchuk studied aggregates of particles under the assumption of weak anchoring [130]. Work on the Stokes drag of a spherical object immersed into a uniformly aligned nematic was performed by Diogo [57], Roman and Terentjev [194], and Heuer et al. [112,105]. The calculations were extended to the Saturn-ring configuration by Ruhwandl and Terentjev [199] and to the dipolar structure by Ventzki and Stark [228], whose work is explored in detail in Section 6. The Stokes drag was also determined through molecular dynamics simulations by Billeter and Pelcovits [10]. Stark and Stelzer [220] numerically investigated multiple nematic emulsions [182] by means of finite elements. We discuss the results in Section 7. It is interesting to note that dipolar configurations also appear in two-dimensional systems including (1) free standing smectic films [132,175], where a circular region with an extra layer plays the role of the spherical particle, and (2) Langmuir films [74], in which a liquid-expanded inclusion in a tilted liquid-condensed region acts similarly. Pettey et al. [175] studied the dipolar structure in two dimensions theoretically. In cholesteric liquid crystals particle-stabilized defect gels were found [239], and people started to investigate dispersions of particles in a smectic phase [80,108,12]. Sequeira and Hill were the first to measure the viscoelastic response of concentrated suspensions of zeolite particles in nematic MBBA [209]. Meeker et al. [143] reported a gel-like structure in nematic colloidal dispersions with a significant shear modulus. Perfectly ordered chains of oil droplets in a nematic were produced from phase separation by Loudet et al. [137]. Very recent studies of the nematic order around spherical particles are based on the minimization of the Landau–de Gennes free energy using an adaptive grid scheme [83], or they employ molecular dynamics simulations of Gay–Berne particles [10,6]. The findings are consistent with the presentation in Section 4.

With two excellent publications [210,211], Ping Sheng initiated the interest in partially ordered nematic films above the nematic-isotropic phase transition temperature T_c using the Landau–de Gennes approach. In 1981, Horn et al. [106] performed first measurements of liquid crystal-mediated forces between curved mica sheets. Motivated by both works, Poniewierski and Sluckin refined Sheng's study [177]. Borštnik and Žumer explicitly considered two parallel plates immersed into a liquid crystal slightly above T_c [18], and thoroughly investigated short-range interactions due to the surface-induced nematic order. An analog work was presented by de Gennes, however, assuming a surface-induced smectic order [50]. The effect of such a presmectic film was measured by Moreau et al. [154]. Recent studies address short-range forces of spherical objects using either analytical methods [15], which we report in Section 8, or numerical calculations [85]. In Section 8 we also demonstrate that such forces can induce flocculation of colloidal particles above the nematic-isotropic phase transition [16,17]. In a more general context, they were also suggested by Löwen [135,136]. Muševič et al. probe these

interactions with the help of an atomic force microscope [158,159,113], whereas Böttger et al. [19] and Poulin et al. [178] are able to suspend solid particles in a liquid crystal above T_c. Even Casimir forces arising from fluctuations in the liquid-crystalline order parameter were investigated both in the nematic [3,2,223] and isotropic phase [240] of a liquid crystal.

3.2. Nematic emulsions

In 1996, Philippe Poulin succeeded in producing inverted and multiple nematic emulsions [182,183]. The notion "inverted" refers to water droplets dispersed in a nematic solvent, in contrast to direct liquid-crystal-in-water emulsions. If the solvent itself forms drops surrounded by the water phase, one has multiple emulsions. We introduce them here since they initiated the theoretical work we report in the following sections.

Philippe Poulin dispersed water droplets of 1 to 5 μm in diameter in a nematic liquid crystal host, pentylcyanobiphenyl (5CB), which formed larger drops ($\sim$ 50 μm diameter) surrounded by a continuous water phase. This isolated a controlled number of colloidal droplets in the nematic host which allowed to observe their structure readily. As a surfactant, a small amount of sodium dodecyl sulfate was used. It is normally ineffective at stabilizing water droplets in oil. Nevertheless, the colloidal water droplets remained stable for several weeks, which suggested that the origin of this stability is the surrounding liquid crystal—a hypothesis that was confirmed by the observation that droplets became unstable and coalesced in less than one hour after the liquid crystal was heated to the isotropic phase. The surfactant also guaranteed a homeotropic, i.e., normal boundary condition of the director at all the surfaces.

The multiple nematic emulsions were studied by observing them between crossed polarizers in a microscope. Under such conditions, an isotropic fluid will appear black, whereas regions in which there is the birefringent nematic will be colored. Thus the large nematic drops in a multiple emulsion appear predominately red in Fig. 10a,[1] whereas the continuous water phase surrounding them is black. Dispersed within virtually all of the nematic drops are smaller colloidal water droplets, which also appear dark in the photo; the number of water droplets tends to increase with the size of the nematic drops. Remarkably, in all cases, the water droplets are constrained at or very near the center of the nematic drops. Moreover, their Brownian motion, usually observed in colloidal dispersions, has completely ceased. However, when the sample is heated to change the nematic into an isotropic fluid, the Brownian motion of the colloidal droplets is clearly visible in the microscope.

Perhaps the most striking observation in Fig. 10a is the behavior of the colloidal droplets when more than one of them cohabit the same nematic drop: the colloidal droplets invariably form linear chains. This behavior is driven by the nematic liquid crystal: the chains break, and the colloidal droplets disperse immediately upon warming the sample to the isotropic phase. However, although the anisotropic liquid crystal must induce an attractive interaction to cause the chaining, it also induces a shorter range repulsive interaction. A section of a chain of droplets under higher magnification (see Fig. 10b) shows that the droplets are prevented from approaching each other too closely, with the separation between droplets being a significant

[1] Reprinted with permission from P. Poulin, H. Stark, T.C. Lubensky, D.A. Weitz, Novel colloidal interactions in anisotropic fluids, Science **275** (1997) 1770. Copyright 1997 American Association for the Advancement of Science.

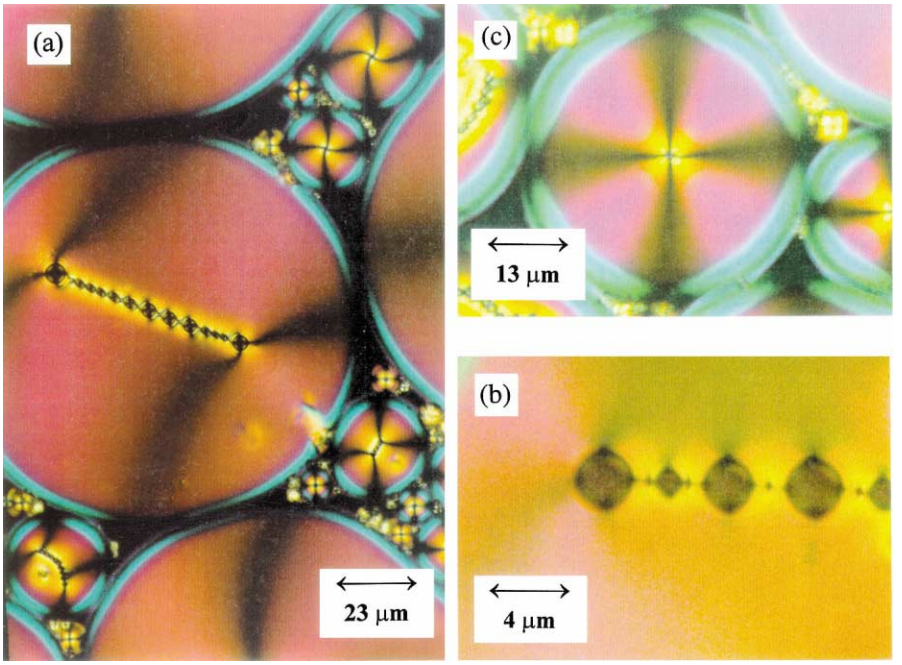

Fig. 10. (a) Microscope image of a nematic multiple emulsion taken under crossed polarizers, (b) a chain of water droplets under high magnification, (c) a nematic drop containing a single water droplet.

fraction of their diameter. A careful inspection of Fig. 10b even reveals black dots between the droplets which we soon will identify as topological point defects. The distance between droplets and these host-fluid defects increases with the droplet radius.

To qualitatively understand the observation, we start with one water droplet placed at the center of a large nematic drop. The homeotropic boundary condition enforces a radial director field between both spherical surfaces. It exhibits a distinctive four-armed star of alternating bright and dark regions under crossed polarizers that extend throughout the whole nematic drop as illustrated in Fig. 10c. Evidently, following the explanations in Section 2.4.2 about point defects, the big nematic drop carries a topological point charge $Q = 1$ that is matched by the small water droplet which acts like a radial hedgehog. Each water droplet beyond the first added to the interior of the nematic drop must create orientational structure out of the nematic itself to satisfy the global constraint $Q = 1$. The simplest (though not the only [140]) way to satisfy this constraint is for each extra water droplet to create a hyperbolic hedgehog in the nematic host. Note that from Fig. 8 we already know that a radial hedgehog (represented by the water droplet) and a hyperbolic point defect carry a total charge zero. Hence, N water droplets in a large nematic drop have to be accompanied by $N - 1$ hyperbolic hedgehogs. Fig. 11 presents a qualitative picture of the director field lines for a string of three droplets. It is rotationally symmetric about the horizontal axis. Between the droplets, hyperbolic hedgehogs appear. They prevent the water droplets from approaching each other and from finally coalescing since this would involve a strong distortion of the director field. The defects therefore mediate a short-range repulsion between the droplets.

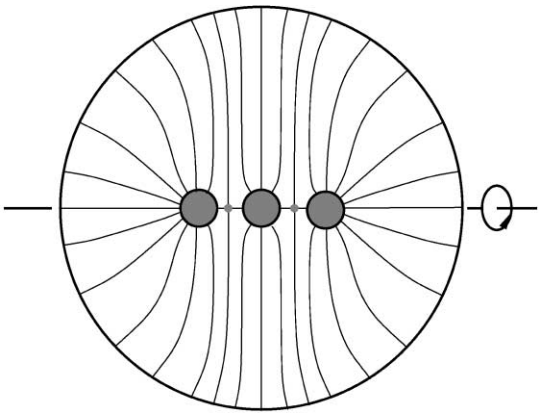

Fig. 11. The director field lines of a nematic drop containing a string of three spherical particles.

In the following sections, we demonstrate the physical ideas which evolved from the experiments on multiple nematic emulsions. We will explain the chaining of droplets by introducing the topological dipole formed by one spherical particle and its companion hyperbolic defect. This leads us to the next chapter where we investigate the simplest situation, i.e., one particle placed in a nematic solvent which is uniformly aligned at infinity.

4. The paradigm—one particle

The multiple nematic emulsions that we introduced in Section 3.2 are already a complicated system. In this section we investigate thoroughly by both analytical and numerical means what I regard as the paradigm for the understanding of inverted nematic emulsions. We ask which director field configurations do occur when one spherical particle that prefers a radial anchoring of the director at its surface is placed into a nematic solvent uniformly aligned at infinity. This constitutes the simplest problem one can think of, and it is a guide to the understanding of more complex situations.

4.1. The three possible configurations

If the directors are rigidly anchored at the surface, the particle carries a topological charge $Q = 1$. Because of the boundary conditions at infinity, the total charge of the whole system is zero; therefore, the particle must nucleate a further defect in its nematic environment. One possibility is a dipolar structure where the particle and a hyperbolic hedgehog form a tightly bound object which we call *dipole* for short (see Fig. 12). As already explained in Fig. 8, the topological charges $+1$ of a radial hedgehog, represented by the particle, and of a hyperbolic point defect "add up" to a total charge of zero. In the *Saturn-ring* configuration, a $-1/2$ disclination ring encircles the spherical particle at its equator (see Fig. 12). Of course, the disclination ring can be moved upward or downward, and by shrinking it to the topologically

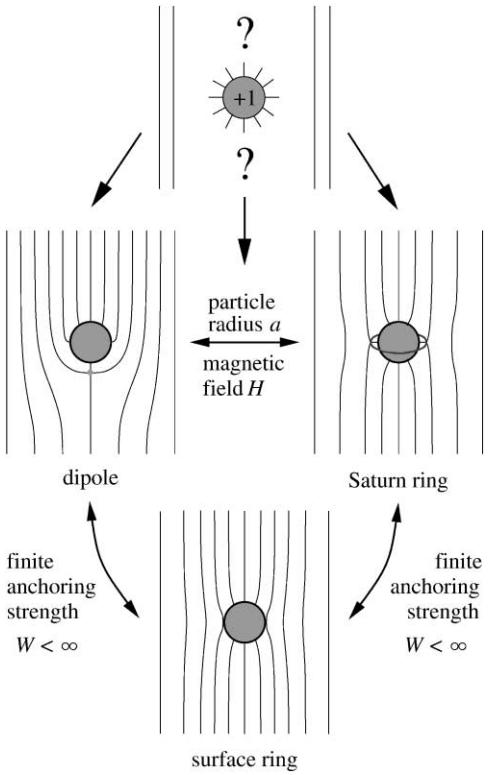

Fig. 12. A spherical particle with a preferred homeotropic anchoring at its surface that is placed into a uniformly aligned nematic liquid crystal exhibits three possible structures: the dipole configuration where the particle is accompanied by a hyperbolic hedgehog, the Saturn-ring configuration where the particle is surrounded by a $-1/2$ disclination ring at the equator, and the surface-ring configuration.

equivalent hyperbolic hedgehog, the Saturn ring is continuously transformed into the dipole configuration. However, our calculations show that a non-symmetric position of the defect ring is never stable. When the surface anchoring strength W is lowered (see Fig. 12), the core of the disclination ring prefers to sit directly at the surface of the particle. For sufficiently low W, the director field becomes smooth everywhere, and a ring of tangentially oriented directors is located at the equator of the sphere. In the case of tangential boundary conditions, there exists only one structure. It possesses two surface defects, called boojums, at the north and south pole of the particle [145,26,120,231]. We will not investigate it further.

It is instructive to first consider the director field far away from the particle, which crucially depends on the global symmetry of the system [22,140]. With its knowledge, ansatz functions for the director configurations around a particle can be checked. Furthermore, the far field determines the long-range two-particle interaction. Let the director $\boldsymbol{n}_0$ at infinity point along the z axis. Then, in the far field, the director is approximated by $\boldsymbol{n}(\boldsymbol{r}) \approx (n_x, n_y, 1)$ with $n_x, n_y \ll 1$. In leading order, the normalization of the director can be neglected, and the Euler–Lagrange equations for n_x and n_y arising from a minimization of the Frank free energy in the one-constant

approximation are simply Laplace equations:

$$\nabla^2 n_\mu = 0 \,. \tag{4.1}$$

The solutions are the well-known multipole expansions of electrostatics that include monopole, dipole, and quadrupole terms. They are all present if the suspended particle has a general shape or if, e.g., the dipole in Fig. 12 is tilted against $\boldsymbol{n}_0$. In the dipole configuration with its axial symmetry about $\boldsymbol{n}_0$, the monopole is forbidden, and we obtain

$$n_x = p\frac{x}{r_3} + 2c\frac{zx}{r^5} \quad \text{and} \quad n_y = p\frac{y}{r_3} + 2c\frac{zy}{r^5} \,, \tag{4.2}$$

where $r = (x^2 + y^2 + z^2)^{1/2}$. We use the expansion coefficients p and c to assign both a dipole ($\boldsymbol{p}$) and quadrupole ($\boldsymbol{c}$) moment to the configuration:

$$\boldsymbol{p} = p\boldsymbol{n}_0 \quad \text{and} \quad \boldsymbol{c} = c(\boldsymbol{n}_0 \otimes \boldsymbol{n}_0 - \mathbf{1}/3) \,. \tag{4.3}$$

The symbol $\otimes$ means tensor product, and $\mathbf{1}$ is the unit tensor of second rank. We adopt the convention that the dipole moment $\boldsymbol{p}$ points from the companion defect to the particle. Hence, if $p > 0$, the far field of Eqs. (4.2) belongs to a dipole configuration with the defect sitting below the particle (see Fig. 12). Note, that by dimensional analysis, $p \sim a^2$ and $c \sim a^3$, where a is the radius of the spherical particle. Saturn-ring and surface-ring configurations possess a mirror plane perpendicular to the rotational axis. Therefore, the dipole term in Eqs. (4.2) is forbidden, i.e., $p = 0$. We will show in Section 6 that the multipole moments $\boldsymbol{p}$ and $\boldsymbol{c}$ determine the long-range two-particle interaction. We will derive it on the basis of a phenomenological theory.

In the present section we investigate the dipole by both analytical and numerical means. First, we identify a twist transition which transforms it into a chiral object. Then, we study the transition from the dipole to the Saturn ring configuration, which is induced either by decreasing the particle radius or by applying a magnetic field. The role of metastability is discussed. Finally, we consider the surface-ring configuration and point out the importance of the saddle-splay free energy F_{24}. Lower bounds for the surface-anchoring strength W are given.

4.2. An analytical investigation of the dipole

Even in the one-constant approximation and for fixed homeotropic boundary conditions, analytical solutions of the Euler–Lagrange equations, arising from the minimization of the Frank free energy, cannot be found. The Euler–Lagrange equations are highly non-linear due to the normalization of the director. In this subsection we investigate the dipole configuration with the help of ansatz functions that obey all boundary conditions and possess the correct far-field behavior. The free parameters in these ansatz functions are determined by minimizing the Frank free energy. We will see that this procedure already provides a good insight into our system.

We arrive at appropriate ansatz functions by looking at the electrostatic analog of our problem [182,140], i.e., a conducting sphere of radius a and with a reduced charge q which is exposed to an electric field of unit strength along the z axis. The electric field is

$$\boldsymbol{E}(\boldsymbol{r}) = \boldsymbol{e}_z + qa^2\frac{\boldsymbol{r}}{r^3} - a^3\frac{r^2\boldsymbol{e}_z - 3z\boldsymbol{r}}{r^5} \,. \tag{4.4}$$

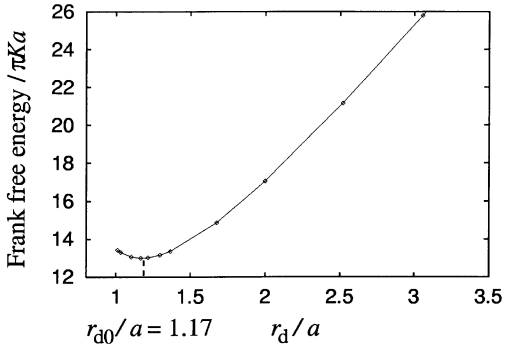

Fig. 13. Frank free energy (in units of πKa) for the topological dipole as a function of the reduced distance r_d/a from the particle center to the companion hedgehog.

In order to enforce the boundary condition that $\boldsymbol{E}$ be normal to the surface of the sphere, an electric image dipole has to be placed at the center of the sphere. The ansatz function for the director field follows from a normalization: $\boldsymbol{n}(\boldsymbol{r}) = \boldsymbol{E}(\boldsymbol{r})/|\boldsymbol{E}(\boldsymbol{r})|$. An inspection of its far field gives

$$\boldsymbol{n}(\boldsymbol{r}) \approx \left(qa^2 \frac{x}{r^3} + 3a^3 \frac{xz}{r^5}, qa^2 \frac{y}{r^3} + 3a^3 \frac{yz}{r^5} \right) , \tag{4.5}$$

in agreement with Eqs. (4.2). The electrostatic analog assigns a dipole moment qa^2 and a quadrupole moment $3a^3/2$ to the topological dipole. The zero of the electric field determines the location $-r_d \boldsymbol{e}_z$ of the hyperbolic hedgehog on the z axis. Thus, q or the distance r_d from the center of the particle are the variational parameters of our ansatz functions. Note that for $q = 3$, the hedgehog just touches the sphere, and that for $q < 3$, a singular ring appears at the surface of the sphere. In Fig. 13 we plot the Frank free energy in the one-constant approximation and in units of πKa as a function of the reduced distance r_d/a. The saddle-splay term is not included, since for rigid anchoring it just provides a constant energy shift. There is a pronounced minimum at $r_{d0} = 1.17a$ corresponding to a dipole moment $p = qa^2 = 3.08a^2$. The minimum shows that the hyperbolic hedgehog sits close to the spherical particle. To check the magnitude of the thermal fluctuations of its radial position, we determine the curvature of the energy curve at r_{d0}; its approximate value amounts to $33\pi K/a$. According to the equipartition theorem, the average thermal displacement δr_{d0} follows from the expression

$$\frac{\delta r_{d0}}{a} \approx \sqrt{\frac{k_B T}{33\pi Ka}} \approx 2 \times 10^{-3} , \tag{4.6}$$

where the final estimate employs $k_B T \approx 4 \times 10^{-14}$ erg, $K \approx 10^{-6}$ dyn, and $a = 1$ μm. These fluctuations in the length of the topological dipole are unobservably small. For angular fluctuations of the dipole, we find $\delta\theta \approx 10^{-2}$, i.e., still difficult to observe [140]. We conclude that the spherical particle and its companion hyperbolic hedgehog form a tightly bound object. Interestingly, we note that angular fluctuations in the 2D version of this problem diverge logarithmically with the sample size [175]. They are therefore much larger and have indeed been observed in free standing smectic films [132].

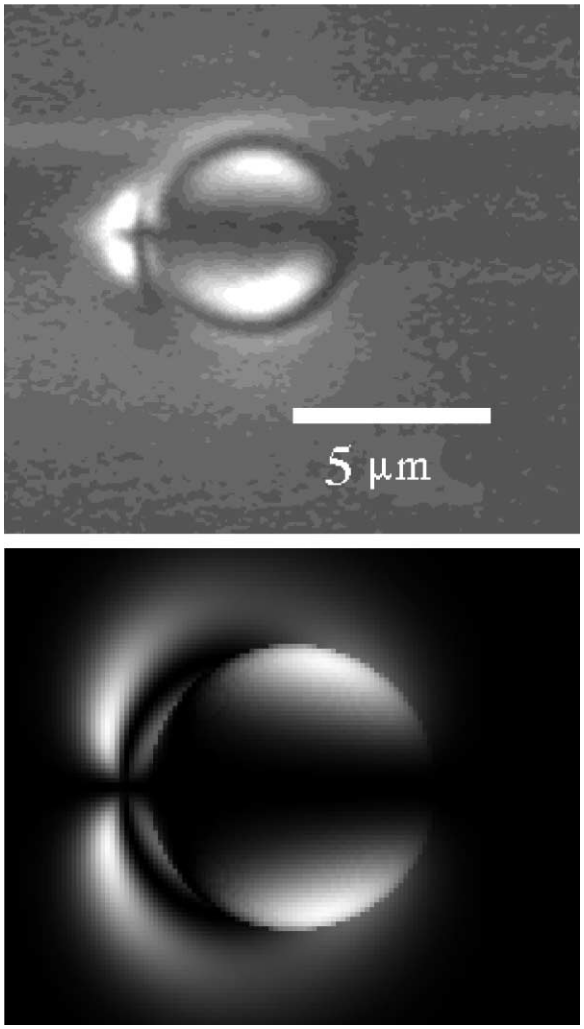

Fig. 14. (Top) Image of a single droplet with its companion defect as observed under crossed polarizers obtained by Poulin [183]. (Bottom) Simulated image of the same configuration using the Jones matrix formalism [140]. The two pictures are very similar. From Ref. [140].

The droplet-defect dipole was observed by Philippe Poulin in inverted nematic emulsions [183]. In the top part of Fig. 14 we present how it looks like in a microscope under crossed polarizers, with one polarizer parallel to the dipole axis. In the bottom part of Fig. 14 we show a calculated image using the Jones matrix formalism [60] based on the director field of the electrostatic analog. Any refraction at the droplet boundary is neglected. The similarity of the two images is obvious and clearly confirms the occurrence of the dipole configuration.

The electric field ansatz is generalized by no longer insisting that it originates in a true electric field. This allows us to introduce additional variational parameters [140]. The Frank free energy at r_{d0} is lowered, and the equilibrium separation amounts to $r_{d0} = 1.26a$. The

respective dipole and quadrupole moments turn out to be $p = 2.20a^2$ and $c = -1.09a^2$. We are also able to construct ansatz functions for the dipole–Saturn ring transition utilizing the method of images for the related 2D problem and correcting the far field [140]. The results agree with the numerical study presented in the next subsection.

4.3. Results and discussion of the numerical study

Before we present the results of our numerical study, we summarize the numerical method. Details can be found in [219].

4.3.1. Summary of numerical details

The numerical investigation is performed on a grid which is defined by modified spherical coordinates. Since the region outside the spherical particle is infinitely extended, we employ a radial coordinate $\rho = 1/r^2$. The exponent 2 is motivated by the far field of the dipole configuration. Such a transformation has two advantages. The exterior of the particle is mapped into a finite region, i.e., the interior of the unit sphere ($\rho \leqslant 1$). Furthermore, equally spaced grid points along the coordinate ρ result in a mesh size in real space which is small close to the surface of the particle. In this area the director field is strongly varying, and hence a good resolution for the numerical calculation is needed. On the other hand, the mesh size is large far away from the sphere where the director field is nearly homogeneous. Since our system is axially symmetric, the director field only depends on ρ and the polar angle θ. The director is expressed in the local coordinate basis $(\mathbf{e}_r, \mathbf{e}_\theta, \mathbf{e}_\phi)$ of the standard spherical coordinate system, and the director components are parametrized by a tilt $[\Theta(\rho,\theta)]$ and a twist $[\Phi(\rho,\theta)]$ angle: $n_r = \cos\Theta$, $n_\theta = \sin\Theta\cos\Phi$, and $n_\phi = \sin\Theta\sin\Phi$.

The total free energy $F_{\boldsymbol{n}}$ of Eq. (2.1) is expressed in the modified spherical coordinates. Then, the Euler–Lagrange equations in the bulk and at the surface are formulated with the help of the chain rules of Eqs. (2.14) and (2.15) and by utilizing the algebraic program Maple. A starting configuration of the director field is chosen and relaxed into a local minimum via the Newton–Gauss–Seidel method [187] which was implemented in a Fortran program.

So far we have described the conventional procedure of a numerical investigation. Now, we address the problem of how to describe disclination rings numerically. Fig. 15 presents such a ring whose general position is determined by a radial (r_d) and an angular (θ_d) coordinate. The free energy $F_{\boldsymbol{n}}$ of the director field follows from a numerical integration. This assigns some energy to the disclination ring which certainly is not correct since the numerical integration does not realize the large director gradients close to the defect core. To obtain a more accurate value for the total free energy F, we use the expression

$$F = F_{\boldsymbol{n}} - F_{\boldsymbol{n}}|_\mathrm{torus} + F_\mathrm{c/d} \times 2\pi r_\mathrm{d} \sin\theta_\mathrm{d} \,, \tag{4.7}$$

where F_c and F_d are the line energies of a disclination introduced in Eqs. (2.32) and (2.34). The quantity $F_{\boldsymbol{n}}|_\mathrm{torus}$ denotes the numerically calculated free energy of a toroidal region of cross section πR^2 around the disclination ring. Its volume is $\pi R^2 \times 2\pi r_\mathrm{d} \sin\theta_\mathrm{d}$. The value $F_{\boldsymbol{n}}|_\mathrm{torus}$ is replaced by the last term on the right-hand side of Eq. (4.7), which provides the correct free energy with the help of the line energies F_c or F_d. We checked that the cross section πR^2 of the cut torus has to be equal or larger than $3\Delta\rho\,\Delta\theta/2$, where $\Delta\rho$ and $\Delta\theta$ are the lattice

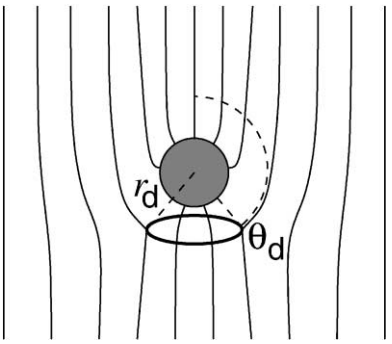

Fig. 15. Coordinates (r_d, θ_d) for a $-1/2$ disclination ring with a general position around the spherical particle. From Ref. [219].

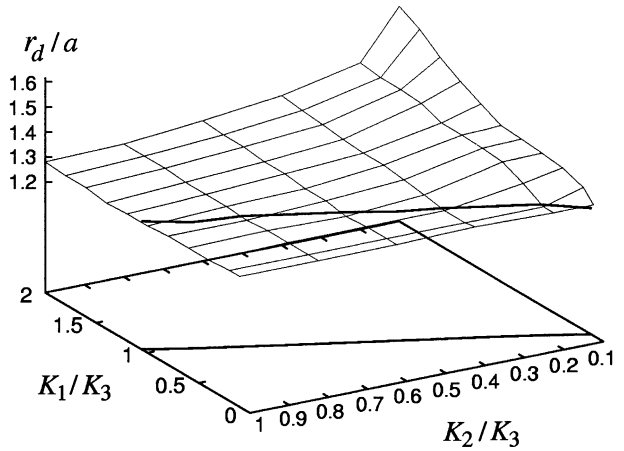

Fig. 16. The reduced distance r_d/a of the hyperbolic hedgehog from the center of the sphere as a function of the reduced splay (K_1/K_3) and twist (K_2/K_3) constants.

constants of our grid. For larger cross sections, the changes in the free energy F for fixed core radius r_c were less than 1%, i.e., F became independent of πR^2. What is the result of this procedure? All lengths in the free energy F_n can be rescaled by the particle radius a. This would suggest that the director configuration does not depend on the particle size. However, with the illustrated procedure a second length scale, i.e., the core radius r_c of a disclination, enters. All our results on disclination rings therefore depend on the ratio a/r_c. In discussing them, we assume $r_c \approx 10\,\text{nm}$ [111] which then determines the radius a for a given a/r_c.

4.3.2. Twist transition of the dipole configuration

In this subsection we present our numerical study of the topological dipole. We always assume that the directors are rigidly anchored at the surface ($W \to \infty$) and choose a zero magnetic field. In Fig. 16 we plot the reduced distance r_d/a of the hedgehog from the center of the sphere as a function of the reduced splay (K_1/K_3) and twist (K_2/K_3) constants. In the

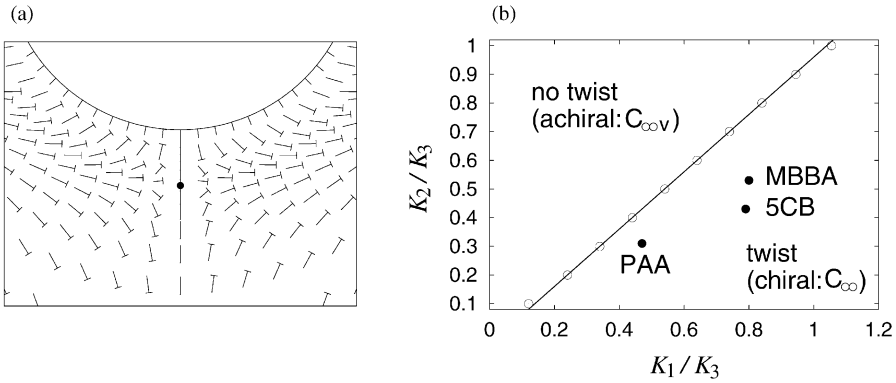

Fig. 17. (a) Nail picture of a closeup of the twisted dipole configuration. Around the hyperbolic hedgehog the directors are tilted relative to the drawing plane. From Ref. [219]. (b) Phase diagram of the twist transition as a function of the reduced splay (K_1/K_3) and twist (K_2/K_3) constants. A full explanation is given in the text.

one-constant approximation, we find $r_d = 1.26 \pm 0.02$, where the mesh size of the grid determines the uncertainty in r_d. Our result is in excellent agreement with the generalized electric-field ansatz we introduced in the last subsection [140]. However, Ruhwandl and Terentjev using a Monte-Carlo minimization report a somewhat smaller value for r_d [200]. In front of the thick line r_d is basically constant. Beyond the line, r_d starts to grow which indicates a structural change in the director field illustrated in the nail picture of Fig. 17a. Around the hyperbolic hedgehog the directors develop a non-zero azimuthal component n_ϕ, i.e., they are tilted relative to the drawing plane. This introduces a twist into the dipole. It should be visible under a polarizing microscope when the dipole is viewed along its symmetry axis.

In Fig. 17b we draw a phase diagram of the twist transition. As expected, it occurs when K_1/K_3 increases or when K_2/K_3 decreases, i.e., when a twist deformation costs less energy than a splay distortion. The open circles are numerical results for the transition line which can well be fitted by the straight line $K_2/K_3 \approx K_1/K_3 - 0.04$. Interestingly, the small offset 0.04 means that K_3 does not play an important role. Typical calamatic liquid crystals like MBBA, 5CB, and PAA should show the twisted dipole configuration.

Since the twist transition breaks the mirror symmetry of the dipole, which then becomes a chiral object, we describe it by a Landau expansion of the free energy:

$$F = F_0 + a(K_1/K_3, K_2/K_3)[n_\phi^{\max}]^2 + c[n_\phi^{\max}]^4 \ . \tag{4.8}$$

With the maximum azimuthal component $n_\phi^{\max}$ we have introduced a simple order parameter. Since the untwisted dipole possesses a mirror symmetry, only even powers of $n_\phi^{\max}$ are allowed. The phase transition line is determined by $a(K_1/K_3, K_2/K_3) = 0$. According to Eq. (4.8), we expect a power-law dependence of the order parameter with the exponent $1/2$ in the twist region close to the phase transition. To test this idea, we choose a constant K_2/K_3 ratio and determine $n_\phi^{\max}$ for varying K_1. As the log–log plot in Fig. 18 illustrates, when approaching the phase transition, the order parameter obeys the expected power law:

$$n_\phi^{\max} \sim (K_1/K_3 - 0.4372)^{1/2} \quad \text{with } K_2/K_3 = 0.4 \ . \tag{4.9}$$

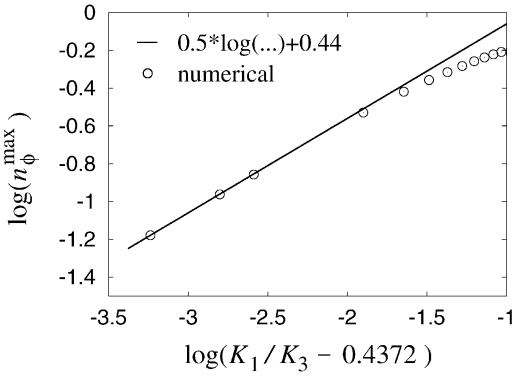

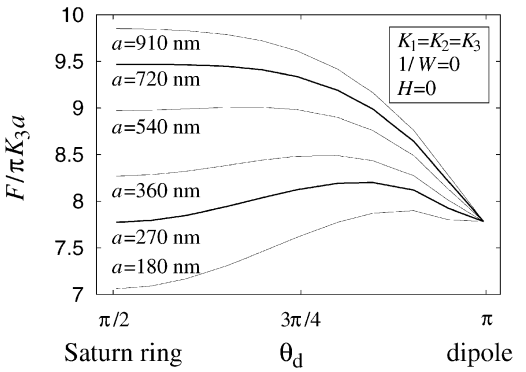

Fig. 18. Log–log plot of the order parameter $n_\phi^{\max}$ versus K_1/K_3 close to the twist transition ($K_2/K_3 = 0.4$); ○ ... numerical values, – ... fit by a straight line.

Fig. 19. The free energy F in units of $\pi K_3 a$ as a function of the angular coordinate θ_d. The parameter of the curves is the particle size a. Further parameters are indicated in the inset.

4.3.3. Dipole versus Saturn ring

There are two possibilities to induce a transition from the dipole to the Saturn-ring configuration; either by reducing the particle size or by applying, e.g., a magnetic field. We always assume rigid anchoring in this subsection, set $K_{24} = 0$, and start with the first point.

4.3.3.1. Effect of particle size. In Fig. 19 we plot the free energy F in units of $\pi K_3 a$ as a function of the angular coordinate θ_d of the disclination ring. For constant θ_d, the free energy F was chosen as the minimum over the radial coordinate r_d. The particle radius a is the parameter of the curves, and the one-constant approximation is employed. Recall that $\theta_d = \pi/2$ and $\theta_d = \pi$ correspond, respectively, to the Saturn-ring or the dipole configuration. Clearly, for small particle sizes ($a = 180\,\text{nm}$) the Saturn ring is the absolutely stable configuration, and the dipole enjoys some metastability. However, thermal fluctuations cannot induce a transition to the dipole since the potential barriers are much higher than the thermal energy $k_B T$. E.g., a barrier of $0.1\pi K_3 a$ corresponds to $1000 k_B T$ ($T = 300\,\text{K}$, $a = 1\,\mu\text{m}$). At $a \approx 270\,\text{nm}$, the dipole assumes the global minimum of the free energy, and finally the Saturn ring becomes absolutely unstable at $a \approx 720\,\text{nm}$. The scenario agrees with the results of Ref. [140] where an ansatz function for the director field was used. Furthermore, we stress that the particle sizes were calculated with the choice of 10 nm as the real core size of a line defect, and that our results depend on the line energy (2.32) of the disclination.

The reduced radial coordinate r_d/a of the disclination ring as a function of θ_d is presented in Fig. 20. It was obtained by minimizing the free energy for fixed θ_d. As long as the ring is open, r_d does not depend on θ_d within an error of ± 0.01. Only in the region where it closes to the hyperbolic hedgehog, does r_d increase sharply. The figure also illustrates that the ring sits closer to larger particles. The radial position of $r_d/a = 1.10$ for 720 nm particles agrees very well with analytical results obtained by using an ansatz function (see Refs. [140]) and with numerical calculations based on a Monte-Carlo minimization [200]. Recent observations of

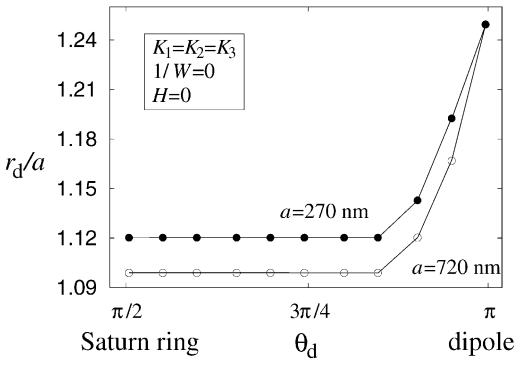

Fig. 20. The reduced radial coordinate r_d/a of a disclination ring as a function of θ_d for two particle sizes. Further parameters are indicated in the inset.

the Saturn-ring configuration around glass spheres of 40, 60, or 100 μm in diameter [97] seem to contradict our theoretical findings. However, we explain them by the strong confinement in 120-μm-thick liquid crystal cells which is equivalent to a strong magnetic field.

4.3.3.2. Effect of a magnetic field. A magnetic field applied along the symmetry axis of the dipole can induce a transition to the Saturn-ring configuration. This can be understood from a simple back-of-the-envelope calculation. Let us consider high magnetic fields, i.e., magnetic coherence lengths much smaller than the particle size a. The magnetic coherence length ξ_H was introduced in Eq. (2.9) as the ratio of elastic and magnetic torques on the director. For $\xi_H \ll a$, the directors are basically aligned along the magnetic field. In the dipole configuration, the director field close to the hyperbolic hedgehog cannot change its topology. The field lines are "compressed" along the z direction, and high densities of the elastic and magnetic free energies occur in a region of thickness ξ_H. Since the field lines have to bend around the sphere, the cross section of the region is of the order of a^2, and its volume is proportional to $a^2\xi_H$. The Frank free energy density is of the order of K/ξ_H^2, where K is a typical Frank constant, and therefore the elastic free energy scales with Ka^2/ξ_H. The same holds for the magnetic free energy. In the case of the Saturn-ring configuration, high free energy densities occur in a toroidal region of cross section $\propto\xi_H^2$ around the disclination ring. Hence, the volume scales with $a\xi_H^2$, and the total free energy is of the order of Ka, i.e., a factor a/ξ_H smaller than for the dipole.

Fig. 21 presents a calculation for a particle size of $a=0.5$ μm and the liquid crystal compound 5CB. We plot the free energy in units of $\pi K_3 a$ as a function of θ_d for different magnetic field strengths which we indicate by the reduced inverse coherence length a/ξ_H. Without a field ($a/\xi_H = 0$), the dipole is the energetically preferred configuration. The Saturn ring shows metastability. A thermally induced transition between both states cannot happen because of the high potential barrier. At a field strength $a/\xi_H = 0.33$, the Saturn ring becomes the stable configuration. However, there will be no transition until the dipole loses its metastability at a field strength $a/\xi_H = 3.3$, which is only indicated by an arrow in Fig. 21. Once the system has changed to the Saturn ring, it will stay there even for zero magnetic field. Fig. 22a schematically illustrates how a dipole can be transformed into a Saturn ring with the help of a magnetic field.

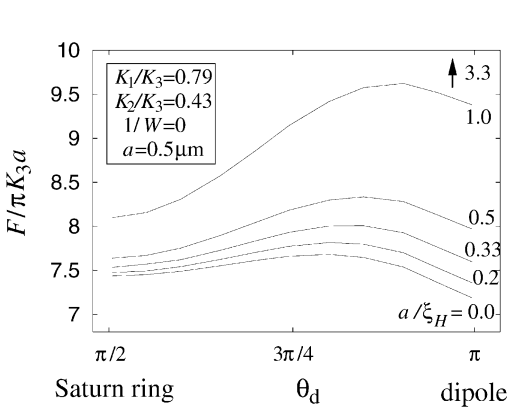

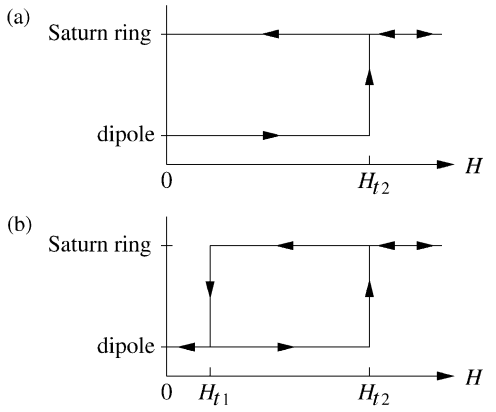

Fig. 21. The free energy F in units of $\pi K_3 a$ as a function of the angular coordinate θ_d. The parameter of the curves is the reduced inverse magnetic coherence length a/ξ_H. Further parameters are indicated in the inset.

Fig. 22. (a) The Saturn ring is metastable at $H=0$. The dipole can be transformed into the Saturn ring by increasing the magnetic field H beyond H_{t2} where the dipole loses its metastability. Turning off the field the Saturn ring remains. (b) The Saturn ring is unstable at $H=0$. When the magnetic field is decreased from values above H_{t2}, the Saturn ring shrinks back to the dipole at H_{t1} where the Saturn ring loses its metastability. A hysteresis occurs. From Ref. [219].

If the Saturn ring is unstable at zero field, a hysteresis occurs (see Fig. 22b). Starting from high magnetic fields, the Saturn ring loses its metastability at H_{t1}, and a transition back to the dipole takes place. In Fig. 19 we showed that the second situation is realized for particles larger than 720 nm. We also performed calculations for a particle size of 1 μm and the liquid crystal compound 5CB and still found the Saturn ring to be metastable at zero field in contrast to the result of the one-constant approximation.

To be more concrete, according to Eq. (2.9), $a/\xi_H=1$ corresponds to a field strength of 4.6 T when 0.5 μm particles and the material parameters of 5CB ($K_3=0.53\times10^{-6}$ dyn, $\Delta\chi=10^{-7}$) are used. Hence, the transition to the Saturn ring in Fig. 21 occurs at a rather high field of 15 T. Assuming that there is no dramatic change in $a/\xi_H=3.3$ for larger particles, this field decreases with increasing particle radius. Alternatively, the transition to the Saturn ring is also induced by an electric field with the advantage that strong fields are much easier to apply. However, the large dielectric anisotropy $\Delta\varepsilon=\varepsilon_\parallel-\varepsilon_\perp$ complicates a detailed analysis because of the difference between applied and local electric fields. Therefore, the electric coherence length $\xi_E=[4\pi K_3/(\Delta\varepsilon E^2)]^{1/2}$, which replaces ξ_H, only serves as a rough estimate for the applied field E necessary to induce a transition to the Saturn ring.

4.3.4. *Influence of finite surface anchoring*

In the last subsection we investigate the effect of finite anchoring on the director field around the spherical particle. The saddle-splay term with its elastic constant K_{24} is important now. We always choose a zero magnetic field. In Fig. 23 we employ the one-constant approximation and plot the free energy versus the reduced surface extrapolation length ξ_S/a for different reduced

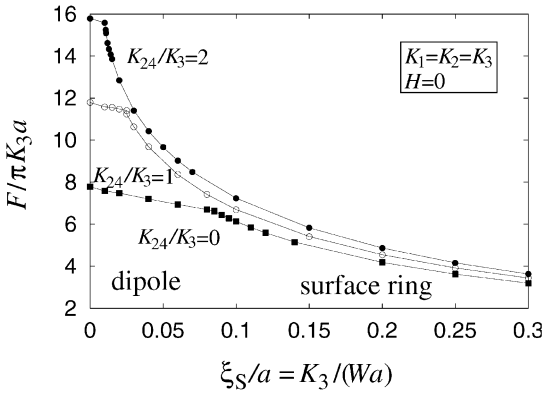

Fig. 23. The minimum free energy F in units of $\pi K_3 a$ as a function of the reduced surface extrapolation length ξ_S/a for different K_{24}/K_3. A first-order phase transition from the dipole to the surface ring occurs. Further parameters are indicated in the inset.

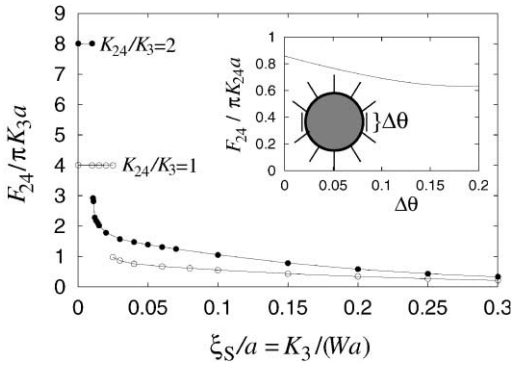

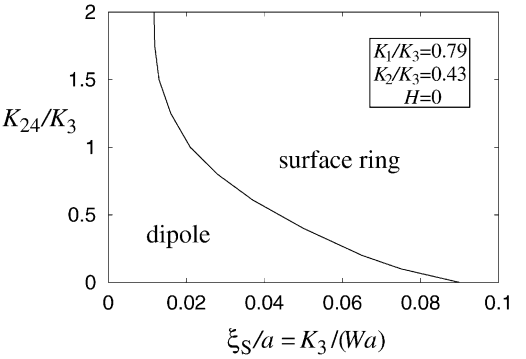

Fig. 24. The saddle-splay free energy F_{24} in units of $\pi K_3 a$ as a function of ξ_S/a for the same curves as in Fig. 23. Inset: F_{24} in units of $\pi K_{24} a$ versus the angular width of the surface ring calculated from the ansatz functions in Eqs. (4.10).

Fig. 25. Phase diagram of the dipole-surface ring transition as a function of ξ_S/a and K_{24}/K_3. Further parameters are indicated in the inset.

saddle-splay constants K_{24}/K_3. Recall that ξ_S is inversely proportional to the surface constant W [see Eq. (2.11)]. The straight lines belong to the dipole. Then, for decreasing surface anchoring, there is a first-order transition to the surface-ring structure. We never find the Saturn ring to be the stable configuration although it enjoys some metastability. For $K_{24}/K_3=0$, the transition takes place at $\xi_S/a \approx 0.085$. This value is somewhat smaller than the result obtained by Ruhwandl and Terentjev [200]. One could wonder why the surface ring already occurs at such a strong anchoring like $\xi_S/a \approx 0.085$ where any deviation from the homeotropic anchoring costs a lot of energy. However, if $\Delta\theta$ is the angular width of the surface ring where the director deviates from the homeotropic alignment (see inset of Fig. 24) then a simple energetical estimate allows $\Delta\theta$ to be of the order of ξ_S/a. It is interesting to see that the transition point shifts to higher anchoring

strengths, i.e., decreasing ξ_S/a when K_{24}/K_3 is increased. Obviously, the saddle-splay term favors the surface-ring configuration. To check this conclusion, we plot the reduced saddle-splay free energy F_{24} versus ξ_S/a in Fig. 24. The horizontal lines belong to the dipole. They correspond to the saddle-splay energy $4\pi K_{24}a$ which one expects for a rigid homeotropic anchoring at the surface of the sphere. In contrast, for the surface-ring configuration the saddle-splay energy drops sharply. The surface ring at the equator of the sphere introduces a "saddle" in the director field as illustrated in the inset of Fig. 24. Such structures are known to be favored by the saddle-splay term. We modeled the surface ring with an angular width $\Delta\theta$ by the following radial and polar director components:

$$n_r = -\tanh\left(\frac{\theta - \pi/2}{\Delta\theta}\right) \quad \text{and} \quad n_\theta = -\left[\cosh\left(\frac{\theta - \pi/2}{\Delta\theta}\right)\right]^{-1}, \tag{4.10}$$

where $\Delta\theta \ll \pi/2$ to ensure that $n_r = 1$ at $\theta = 0, \pi$, and calculated the saddle-splay energy versus $\Delta\theta$ by numerical integration. The result is shown in the inset of Fig. 24. It fits very well to the full numerical calculations and confirms again that a narrow "saddle" around the equator can considerably reduce the saddle-splay energy.

For the liquid crystal compound 5CB we determined the stable configuration as a function of K_{24}/K_3 and ξ_S/a. The phase diagram is presented in Fig. 25. With its help, we can derive a lower bound for the surface constant W at the interface of water and 5CB when the surfactant sodium dodecyl sulfate is involved. As the experiments by Poulin et al. clearly demonstrate, water droplets dispersed in 5CB do assume the dipole configuration. From the phase diagram we conclude $\xi_S/a < 0.09$ as a necessary condition for the existence of the dipole. With $a \approx 1\,\mu\text{m}$, $K_3 = 0.53 \times 10^{-6}\,\text{dyn}$, and definition (2.11) for ξ_S we arrive at

$$W > 0.06\,\text{erg/cm}^2\,. \tag{4.11}$$

If we assume the validity of the Cauchy relation (2.5), which for 5CB gives $K_{24}/K_3 = 0.61$, we conclude that $W > 0.15\,\text{erg/cm}^2$. Recently, Mondain-Monval et al. were able to observe an equatorial ring structure by changing the composition of a surfactant mixture containing sodium dodecyl sulfate (SDS) and a copolymer of ethylene and propylene oxide (Pluronic F 68) [153]. We conclude from our numerical investigation that they observed the surface-ring configuration.

4.4. Conclusions

In this section we presented a detailed study of the three director field configurations around a spherical particle by both analytical and numerical means. We clearly find that for large particles and sufficiently strong surface anchoring, the dipole is the preferred configuration. For conventional calamitic liquid crystals, where $K_2 < K_1$, the dipole should always exhibit a twist around the hyperbolic hedgehog. It should not occur in discotic liquid crystals where $K_2 > K_1$. According to our calculations, the bend constant K_3 plays only a minor role in the twist transition. The Saturn ring appears for sufficiently small particles provided that one can realize a sufficiently strong surface anchoring. According to our investigation, for 200 nm particles the surface constant has to be larger than $W = 0.3\,\text{erg/cm}^2$. However, the dipole can be transformed into the Saturn ring by means of a magnetic field if the Saturn ring is metastable at $H = 0$. Otherwise a hysteresis is visible. For the liquid crystal compound 5CB, we find the Saturn ring

to be metastable at a particle size $a = 1$ μm. Increasing the radius a, this metastability will vanish in analogy with our calculations within the one-constant approximation (see Fig. 19). Lowering the surface-anchoring strength W, the surface-ring configuration with a quadrupolar symmetry becomes absolutely stable. We never find a stable structure with dipolar symmetry where the surface ring possesses a general angular position θ_d or is even shrunk to a point at $\theta_d = 0, \pi$. The surface ring is clearly favored by a large saddle-splay constant K_{24}.

The dispersion of spherical particles in a nematic liquid crystal is always a challenge to experimentalists. The clearest results are achieved in inverted nematic emulsions [182,179,183,153,184]. However, alternative experiments with silica or latex spheres do also exist [181,188,189,153, 180,98] and produce impressive results [97]. We hope that the summary of our research stimulates further experiments which probe different liquid crystals as a host fluid [180], manipulate the anchoring strength [153,97,98], and investigate the effect of external fields [97,98].

5. Two-particle interactions

To understand the properties of, e.g., multi-droplet emulsions, we need to determine the nature of particle–particle interactions. These interactions are mediated by the nematic liquid crystal in which they are embedded and are in general quite complicated. Since interactions are determined by distortions of the director field, there are multi-body as well as two-body interactions. We will content ourselves with calculations of some properties of the effective two-particle interaction. To determine the position-dependent interaction potential between two particles, we should solve the Euler–Lagrange equations, as a function of particle separation, subject to the boundary condition that the director be normal to each spherical object. Solving completely these non-linear equations in the presence of two particles is even more complicated than solving them with one particle, and again we must resort to approximations. Fortunately, interactions at large separations are determined entirely by the far-field distortions and the multipole moments of an individual topological dipole or Saturn ring, which we studied in Section 4.1. The interactions can be derived from a phenomenological free energy. We will present such an approach in this section [190,182,140].

5.1. Formulating a phenomenological theory

In Section 4, we established that each spherical particle creates a hyperbolic hedgehog to which it binds tightly to create a stable topological dipole. The original spherical inclusion is described by three translational degrees of freedom. Out of the nematic it draws a hedgehog, which itself has three translational degrees of freedom. The two combine to produce a dipole with six degrees of freedom, which can be parametrized by three variables specifying the position of the particle, two angles specifying the orientation of the dipole, and one variable specifying the magnitude of the dipole. As we have seen, the magnitude of the dipole does not fluctuate much and can be regarded as a constant. The direction of the dipole is also fairly strongly constrained. It can, however, deviate from the direction of locally preferred orientation (parallel to a local director to be defined in more detail below) when many particles are present. The particle–defect pair is in addition characterized by its higher multipole

moments. The direction of the principal axes of these moments is specified by the direction of the dipole as long as director configurations around the dipole remain uniaxial. The magnitudes of all the uniaxial moments like the strengths p and c of the dipole and quadrupole moment (see Section 4.1) are energetically fixed, as we have shown in Section 4.2. When director configurations are not uniaxial, the multipole tensors will develop additional components, which we will not consider here. We can thus parametrize topological dipoles by their position and orientation and a set of multipole moments, which we regard as fixed. Let $\boldsymbol{e}^\alpha$ be the unit vector specifying the direction of the dipole moment associated with droplet α. Its dipole and quadrupole moments are then $\boldsymbol{p}^\alpha = p\boldsymbol{e}^\alpha$ and $\boldsymbol{c}^\alpha = c(\boldsymbol{e}^\alpha \otimes \boldsymbol{e}^\alpha - \mathbf{1}/3)$, where p and c are the respective magnitudes of the dipole and quadrupole moments calculated, e.g., by analytical means in Section 4.2. The symbol $\otimes$ means tensor product, and $\mathbf{1}$ is the second-rank unit tensor. Note, that this approach also applies to the Saturn-ring and surface-ring configuration but with a vanishing dipole moment $p = 0$. It even applies to particles with tangential boundary conditions where two surfaces defects, called boojums [145,26,120], are located at opposite points of the sphere and where the director field possesses a uniaxial symmetry, too. We now introduce dipole- and quadrupole-moment densities, $\boldsymbol{P}(\boldsymbol{r})$ and $\boldsymbol{C}(\boldsymbol{r})$, in the usual way. Let $\boldsymbol{r}^\alpha$ denote the position of droplet α, then

$$\boldsymbol{P}(\boldsymbol{r}) = \sum_\alpha \boldsymbol{p}^\alpha \delta(\boldsymbol{r} - \boldsymbol{r}^\alpha) \quad \text{and} \quad \boldsymbol{C}(\boldsymbol{r}) = \sum_\alpha \boldsymbol{c}^\alpha \delta(\boldsymbol{r} - \boldsymbol{r}^\alpha)\ . \tag{5.1}$$

In the following, we construct an effective free energy for director and particles valid at length scales large compared to the particle radius. At these length scales, we can regard the spheres as point objects (as implied by the definitions of the densities given above). At each point in space, there is a local director $\boldsymbol{n}(\boldsymbol{r})$ along which the topological dipoles or, e.g., the Saturn rings wish to align. In the more microscopic picture, of course, the direction of this local director corresponds to the far-field director $\boldsymbol{n}_0$. The effective free energy is constructed from rotationally invariant combinations of $\boldsymbol{P}$, $\boldsymbol{C}$, $\boldsymbol{n}$, and the gradient operator ∇ that are also even under $\boldsymbol{n} \to -\boldsymbol{n}$. It can be expressed as a sum of terms

$$F = F_{\mathrm{el}} + F_p + F_C + F_{\mathrm{align}}\ , \tag{5.2}$$

where F_{el} is the Frank free energy, F_p describes interactions between $\boldsymbol{P}$ and $\boldsymbol{n}$, F_C describes interactions between $\boldsymbol{C}$ and $\boldsymbol{n}$ involving gradient operators, and

$$F_{\mathrm{align}} = -D \int \mathrm{d}^3 r\, C_{ij}(\boldsymbol{r}) n_i(\boldsymbol{r}) n_j(\boldsymbol{r}) = -DQ \sum_\alpha \{[\boldsymbol{e}^\alpha \cdot \boldsymbol{n}(\boldsymbol{r}^\alpha)]^2 - 1/3\} \tag{5.3}$$

forces the alignment of the axes $\boldsymbol{e}^\alpha$ along the local director $\boldsymbol{n}(\boldsymbol{r}^\alpha)$. The leading contribution to F_p is identical to the treatment of the flexoelectric effect in a nematic [147,51]

$$F_p = 4\pi K \int \mathrm{d}^3 r[\, -\boldsymbol{P}\cdot\boldsymbol{n}(\nabla\cdot\boldsymbol{n}) + \beta\boldsymbol{P}\cdot(\boldsymbol{n}\times\nabla\times\boldsymbol{n})]\ , \tag{5.4}$$

where β is a material-dependent unitless parameter. The leading contribution to F_C is

$$F_C = 4\pi K \int \mathrm{d}^3 r[(\nabla\cdot\boldsymbol{n})\boldsymbol{n}\cdot\nabla(n_i C_{ij} n_j) + \nabla(n_i C_{ij} n_j)\cdot(\boldsymbol{n}\times\nabla\times\boldsymbol{n})]\ . \tag{5.5}$$

There should also be terms in F_C like $C_{ij}\nabla_k n_i \nabla_k n_j$. These terms can be shown to add contributions to the effective two-particle interaction that are higher order in separation than those arising

from Eq. (5.5). One coefficient in F_p and all coefficients in F_C are fixed by the requirement that the phenomenological theory yields the far field of one particle given by Eq. (4.2) (see next subsection). Eq. (5.5) is identical to that introduced in Ref. [190] to discuss interactions between Saturn rings, provided $n_i C_{ij} n_j$ is replaced by a scalar density $\rho(\boldsymbol{r}) = \sum_\alpha \delta(\boldsymbol{r} - \boldsymbol{r}^\alpha)$. The two energies are absolutely equivalent to leading order in the components n_μ of $\boldsymbol{n}$ perpendicular to $\boldsymbol{n}_0$ provided all $\boldsymbol{e}^\alpha$ are restricted to be parallel to $\boldsymbol{n}_0$.

Since $\boldsymbol{P}$ prefers to align along the local director $\boldsymbol{n}$, the dipole-bend coupling term in Eq. (5.4) can be neglected to leading order in deviations of the director from uniformity. The $-\boldsymbol{P}\cdot\boldsymbol{n}(\nabla\cdot\boldsymbol{n})$ term in Eq. (5.4) shows that dipoles aligned along $\boldsymbol{n}$ create local splay as is evident from the dipole configuration depicted in Fig. 12. In addition, this term says that dipoles can lower their energy by migrating to regions of maximum splay while remaining aligned with the local director. Experiments on multiple nematic emulsions [182,183] support this conclusion. Indeed, the coupling of the dipole moment to a strong splay distortion explains the chaining of water droplets in a large nematic drop whose observation we reported in Section 3.2. We return to this observation in Section 7.

5.2. Effective pair interactions

In the following we assume that the far-field director $\boldsymbol{n}_0$ and all the multipole moments of the particles point along the z axis, i.e., $\boldsymbol{e}^\alpha = \boldsymbol{e}_z = \boldsymbol{n}_0$. Hence, we are able to write the dipole and quadrupole densities as

$$\boldsymbol{P}(\boldsymbol{r}) = P(\boldsymbol{r})\boldsymbol{n}_0 \quad \text{and} \quad \boldsymbol{C}(\boldsymbol{r}) = \tfrac{3}{2}C(\boldsymbol{r})(\boldsymbol{n}_0 \otimes \boldsymbol{n}_0 - \mathbf{1}/3)\,, \tag{5.6}$$

where $P(\boldsymbol{r})$ and $C(\boldsymbol{r})$ can be both positive and negative. We are interested in small deviations from $\boldsymbol{n}_0$, $\boldsymbol{n} = (n_x, n_y, 1)$, and formulate the effective energy of Eq. (5.2) up to harmonic order in n_μ:

$$F = K\int \mathrm{d}^3 r[\tfrac{1}{2}(\nabla n_\mu)^2 - 4\pi P\partial_\mu n_\mu + 4\pi(\partial_z C)\partial_\mu n_\mu]\,. \tag{5.7}$$

The dipole-bend coupling term of Eq. (5.4) does not contribute because $\boldsymbol{P}$ is aligned along the far-field director. The Euler–Lagrange equations for the director components are

$$\nabla^2 n_\mu = 4\pi\partial_\mu[P(\boldsymbol{r}) - \partial_z C(\boldsymbol{r})]\,, \tag{5.8}$$

which possess the solution

$$n_\mu(\boldsymbol{r}) = -\int \mathrm{d}^3 r' \frac{1}{|\boldsymbol{r} - \boldsymbol{r}'|}\partial'_\mu[P(\boldsymbol{r}') - \partial'_z C(\boldsymbol{r}')]\,. \tag{5.9}$$

For a single droplet at the origin, $P(\boldsymbol{r}) = p\delta(\boldsymbol{r})$ and $C(\boldsymbol{r}) = \frac{2}{3}c\delta(\boldsymbol{r})$, and the above equation yields exactly the far field of Eq. (4.2). This demonstrates the validity of our phenomenological approach.

Particles create far-field distortions of the director, which to leading order at large distances are determined by Eq. (5.8). These distortions interact with the director fields of other particles which leads to an effective particle–particle interaction that can be expressed to leading order

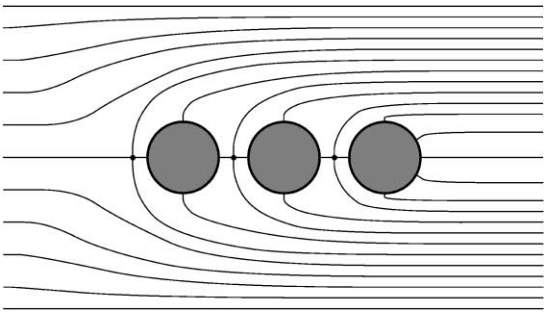

Fig. 26. A chain of three topological dipoles formed due to their dipolar interaction.

as pairwise interactions between dipole and quadrupole densities. Using Eq. (5.9) in Eq. (5.7), we obtain

$$\frac{F}{4\pi K} = \frac{1}{2}\int \mathrm{d}^3 r\, \mathrm{d}^3 r' [P(\boldsymbol{r}) V_{PP}(\boldsymbol{r}-\boldsymbol{r}') P(\boldsymbol{r}') + C(\boldsymbol{r}) V_{CC}(\boldsymbol{r}-\boldsymbol{r}') C(\boldsymbol{r}') + V_{PC}(\boldsymbol{r}-\boldsymbol{r}')][C(\boldsymbol{r})P(\boldsymbol{r}') - P(\boldsymbol{r})C(\boldsymbol{r}')] \,, \tag{5.10}$$

with

$$\begin{aligned} V_{PP}(\boldsymbol{r}) &= \partial_\mu \partial_\mu \frac{1}{r} = \frac{1}{r^3}(1 - 3\cos^3\theta) \\ V_{CC}(\boldsymbol{r}) &= -\partial_z^2 \partial_\mu \partial_\mu \frac{1}{r} = \frac{1}{r^5}(9 - 90\cos^2\theta + 105\cos^4\theta) \\ V_{PC}(\boldsymbol{r}) &= \partial_z \partial_\mu \partial_\mu \frac{1}{r} = \frac{\cos\theta}{r^4}(15\cos^2\theta - 9) \,, \end{aligned} \tag{5.11}$$

where θ is the angle enclosed by the separation vector $\boldsymbol{r}$ and $\boldsymbol{n}_0$. The interaction energy between droplets at positions $\boldsymbol{r}$ and $\boldsymbol{r}'$ with respective dipole and quadrupole moments p, p', c, and c' is thus

$$U(\boldsymbol{R}) = 4\pi K \left[p\,p' V_{PP}(\boldsymbol{R}) + \frac{4}{9} c c' V_{CC}(\boldsymbol{R}) + \frac{2}{3}(c\,p' - c' p) V_{PC}(\boldsymbol{R}) \right] \,, \tag{5.12}$$

where $\boldsymbol{R} = \boldsymbol{r} - \boldsymbol{r}'$. The leading term in the potential $U(\boldsymbol{R})$ is the dipole–dipole interaction which is identical to the analogous problem in electrostatics. Minimizing it over the angle θ, one finds that the dipoles prefer to form chains along their axes, i.e., $pp' > 0$, $\theta = 0, \pi$. Such a chain of dipoles is illustrated in Fig. 26. It is similar to configurations seen in other dipolar systems such as magnetorheological fluids and in magnetic emulsions under the influence of an external field [90,133]. The chaining was observed by Poulin et al. in inverted emulsions [179,183] or in a suspension of micron-size latex particles in a lyotropic discotic nematic [180]. Both systems were placed in a thin rectangular cell of approximate dimensions $20\,\mu\mathrm{m} \times 1\,\mathrm{cm} \times 1\,\mathrm{cm}$. The upper and lower plates were treated to produce tangential boundary conditions. Thus the total topological charge in the cell was zero. The dipolar forces were measured recently by a method introduced by Poulin et al. [179]. When small droplets are filled with a magnetorheological fluid instead of pure water, a small magnetic field of about 100 G, applied perpendicular to the

chain axis, induces parallel magnetic dipoles. Since they repel each other, the droplets in the chain are forced apart. When the magnetic field is switched off, the droplets move towards each other to reach the equilibrium distance. In a chain of two moving droplets, the dipolar force on one droplet has to be balanced by the Stokes drag,

$$24\pi K \frac{p\,p'}{R^4} = 6\pi\eta_{\text{eff}} a v \,, \tag{5.13}$$

where v is the velocity of one particle, and η_{eff} is an effective viscosity, which we will address in Section 6. Inertial effects can be neglected since the movement is overdamped. By measuring the velocity as a function of R, Poulin et al. could show that the origin of the attractive force is indeed of dipolar nature down to a separation of approximately $4a$. Furthermore, they found that the prefactor of the dipolar force scales as a^4, as expected since both the dipole moments p and p' scale as a^2 (see Section 4.1). In Section 6 we will calculate the Stokes drag of a spherical particle.

If $p, p' = 0$, the quadrupolar interaction is dominant. A minimization over θ predicts that the quadrupoles should chain under an angle of $\theta = 49^\circ$ [190]. In experiments with tangential boundary conditions at the droplet surface, where a quadrupolar structure with two opposite surface defects (boojums) forms, the chaining occurred under an angle of $\theta = 30^\circ$, probably due to short-range effects [183]. A similar observation was made in a suspension of 50 nm latex particles in a lyotropic discotic nematic [153], where one expects a surface-ring configuration because of the homeotropic surface anchoring (see Section 4.3.4).

Finally, we discuss the coupling between dipoles and quadrupoles in Eq. (5.12). Their moments scale, respectively, as a^2 or a^3. The coupling is only present when the particles have different radii. Furthermore, for fixed angle θ, the sign of the interaction depends on whether the small particle is on the right or left side of the large one. With this rather subtle effect, which is not yet measured, we close the section about two-particle interactions.

6. The Stokes drag of spherical particles

In Section 2.3 we introduced the Ericksen–Leslie equations that govern the hydrodynamics of a nematic liquid crystal. Due to the director as a second hydrodynamic variable besides the fluid velocity, interesting new dynamical phenomena arise. With the Mięsowicz viscosities and Helfrich's permeation, we presented two of them in Section 2.3. Here we deal with the flow of a nematic around a spherical particle in order to calculate the Stokes drag, which is a well-known quantity for an isotropic liquid [217,202].[2] Via the celebrated Stokes–Einstein relation [63–65], it determines the diffusion constant of a Brownian particle, and it is, therefore, crucial for a first understanding of the dynamics of colloidal suspensions [202].

In Section 6.1 the existing work on the Stokes drag, which has a long-standing tradition in liquid crystals, is reviewed. Starting from the Ericksen–Leslie equations, we introduce the theoretical concepts for its derivation in Section 6.2. We calculate the Stokes drag for three director configurations; a uniform director field, the topological dipole, and the Saturn-ring

[2] We cite here on purpose the excellent course of Sommerfeld on continuum mechanics. An English edition of his lectures on theoretical physics is available.

structure. Since a full analytical treatment is not possible, we have performed a numerical investigation. A summary of its details is presented in Section 6.3. Finally, we discuss the results and open problems in Section 6.4.

6.1. Motivation

Due to the complexity of the Ericksen–Leslie equations, only few examples with an analytical solution exist, e.g., the flow between two parallel plates, which defines the different Mięsowicz viscosities [47], the Couette flow [8,46], the Poiseuille flow [7], which was first measured by Cladis et al. [234], or the back flow [176]. Besides the exploration of new effects, resulting from the coupling between the velocity and director field, solutions to the Ericksen–Leslie equations are also of technological interest. They are necessary to determine the switching times of liquid crystal displays.

A common way to measure viscosities of liquids is the falling-ball method, where the velocity of the falling particle is determined by a balance of the gravitational, the buoyancy, and Stokes's friction force. Early experiments in nematic liquid crystals measured the temperature and pressure dependence of the effective viscosity η_{eff} in the Stokes drag [234,122]. Cladis et al. [234] argued that η_{eff} is close to the Mięsowicz shear viscosity η_b, i.e., to the case where the fluid is flowing parallel to the director (see Fig. 3 in Section 2.3). Nearly twenty years later, Poulin et al. used the Stokes drag to verify the dipolar force between two topological dipoles in inverted nematic emulsions [179]. Böttger et al. [19] observed the Brownian motion of particles above the nematic-isotropic phase transition. Measuring the diffusion constant with the help of dynamic light scattering, they could show that close to the phase transition the effective viscosity in the Stokes drag increases due to surface-induced nematic order close to the particle.

It is obvious that the hydrodynamic solution for the flow of a nematic liquid crystal around a particle at rest, which is equivalent to the problem of a moving particle, presents a challenge to theorists. Diogo [57] assumed the velocity field to be the same as the one for an isotropic fluid and calculated the drag force for simple director configurations. He was interested in the case where the viscous forces largely exceed the elastic forces of director distortions, i.e., Ericksen numbers much larger than one, as we shall explain in the next subsection. Roman and Terentjev, concentrating on the opposite case, obtained an analytical solution for the flow velocity in a spatially uniform director field, by an expansion in the anisotropy of the viscosity [194]. Heuer et al. presented analytical and numerical solutions for both the velocity field and the Stokes drag again assuming a uniform director field [112,105]. They were first investigating a cylinder of infinite length [104]. Ruhwandl and Terentjev allowed for a non-uniform but fixed director configuration, and they numerically calculated the velocity field and the Stokes drag of a cylinder [198] or a spherical particle [199]. The particle was surrounded by the Saturn-ring configuration (see Fig. 12 of Section 4.1), and the cylinder was accompanied by two disclination lines. Billeter and Pelcovits used molecular dynamics simulations to determine the Stokes drag of very small particles [10]. They observed that the Saturn ring is strongly deformed due to the motion of the particles. The experiments on inverted nematic emulsions [182,179] motivated us to perform analogous calculations for the topological dipole [228], which we present in the next subsections. Recently, Chono and Tsuji performed a numerical solution of the Ericksen–Leslie equations around a cylinder determining both the velocity and director field [32]. They could show that

the director field strongly depends on the Ericksen number. However, for homeotropic anchoring their director fields do not show any topological defects required by the boundary conditions.

The Stokes drag of a particle surrounded by a disclination ring strongly depends on the presence of line defects. There exist a few studies, which determine both experimentally [37] and theoretically [107,49,203] the drag force of a moving disclination. In the multi-domain cell, a novel liquid crystal display, the occurrence of twist disclinations is forced by boundary conditions [206,205,192]. It is expected that the motion of these line defects strongly determines the switching time of the display.

6.2. Theoretical concepts

We first review the Stokes drag in an isotropic liquid and then introduce our approach for the nematic environment.

6.2.1. The Stokes drag in an isotropic fluid

The Stokes drag in an isotropic fluid follows from a solution of the Navier–Stokes equations. Instead of considering a moving sphere, one solves the equivalent problem of the flow around a sphere at rest [217]. An incompressible fluid ($\operatorname{div} \boldsymbol{v}=\boldsymbol{0}$) and a stationary velocity field ($\partial \boldsymbol{v}/\partial t=0$) are assumed, so that the final set of equations reads

$$\operatorname{div} \boldsymbol{v} = 0 \quad \text{and} \quad -\nabla p' + \operatorname{div} \boldsymbol{T}' = \boldsymbol{0} \,. \tag{6.1}$$

In an isotropic fluid the viscous stress tensor $\boldsymbol{T}'$ is proportional to the symmetrized velocity gradient $\boldsymbol{A}$, $\boldsymbol{T}' = 2\eta \boldsymbol{A}$, where η denotes the usual shear viscosity. We have subdivided the pressure $p = p_0 + p'$ in a static (p_0) and a hydrodynamic (p') part. The static pressure only depends on the constant mass density ϱ and, therefore, does not appear in the momentum-balance equation of the set (6.1). The hydrodynamic contribution p' is a function of the velocity. It can be chosen zero at infinity. Furthermore, under the assumption of creeping flow, we have neglected the non-linear velocity term in the momentum-balance equation resulting from the convective part of the total time derivative $\mathrm{d}\boldsymbol{v}/\mathrm{d}t$. That means, the ratio of inertial ($\varrho v^2/a$) and viscous ($\eta v/a^2$) forces, which defines the *Reynolds number* $Re = \varrho v a/\eta$, is much smaller than one. To estimate the forces, all gradients are assumed to be of the order of the inverse particle radius a^{-1}, the characteristic length scale of our problem. Eqs. (6.1) are solved analytically for the non-slip condition at the surface of the particle [$\boldsymbol{v}(r=a)=\boldsymbol{0}$], and for a uniform velocity $\boldsymbol{v}_\infty$ at infinity. Once the velocity and pressure fields are known, the drag force F_S follows from an integration of the total stress tensor $-p\boldsymbol{1} + \boldsymbol{T}'$ over the particle surface. An alternative method demands that the dissipated energy per unit time, $\int (\boldsymbol{T}' \cdot \boldsymbol{A})\, \mathrm{d}^3 r$, which we introduced in Eq. (2.27) of Section 2.3, should be $F_S v_\infty$ [11]. The final result is the famous Stokes formula for the drag force:

$$F_S = \gamma v_\infty \quad \text{with } \gamma = 6\pi\eta a \,. \tag{6.2}$$

The symbol γ is called the friction coefficient. The Einstein–Stokes relation relates it to the diffusion constant D of a Brownian particle [63–65]:

$$D = \frac{k_\mathrm{B} T}{6\pi\eta a} \,, \tag{6.3}$$

where k_B is the Boltzmann constant and T is temperature.

We can also calculate the Stokes drag for a finite spherical region of radius $r = a/\varepsilon$ with the particle at its center [228]. The result is

$$F_S = \gamma_\varepsilon v_\varepsilon \quad \text{with } \gamma_\varepsilon = 6\pi\eta a \frac{1 - 3\varepsilon/2 + \varepsilon^3 - \varepsilon^5/2}{(1 - 3\varepsilon/2 + \varepsilon^3/2)^2} , \tag{6.4}$$

where v_ε denotes the uniform velocity at $r = a/\varepsilon$. The correction term is a monotonically increasing function in ε on the interesting interval $[0, 1]$. Hence, the Stokes drag increases when the particle is confined to a finite volume. For $\varepsilon = 1/32$ the correction is about 5%.

6.2.2. The Stokes drag in a nematic environment

To calculate the Stokes drag in a nematic environment, we have to deal with the Ericksen–Leslie equations, which couple the flow of the fluid to the director motion. We do not attempt to solve these equations in general. Analogous to the Reynolds number, we define the *Ericksen number* [49] as the ratio of viscous ($\eta v_\infty/a^2$) and elastic (K/a^3) forces in the momentum balance of Eq. (2.18):

$$Er = \frac{\eta v_\infty a}{K} . \tag{6.5}$$

The elastic forces are due to distortions in the director field, where K stands for an average Frank constant. In the following, we assume $Er \ll 1$, i.e., the viscous forces are too weak to distort the director field, and we will always use the static director field for $\boldsymbol{v} = \mathbf{0}$ in our calculations. The condition $Er \ll 1$ constrains the velocity v_∞. Using typical values of our parameters, i.e., $K = 10^{-6}$ dyn, $\eta = 0.1$ P, and $a = 10\,\mu$m, we find

$$v_\infty \ll 100 \frac{\mu\text{m}}{\text{s}} . \tag{6.6}$$

Before we proceed, let us check for three cases if this constraint is fulfilled. First, in the measurements of the dipolar force by Poulin et al., the velocities of the topological dipole are always smaller than $10\,\mu$m/s [179]. Secondly, in a falling-ball experiment the velocity v of the falling particle is determined by a balance of the gravitational, the buoyancy, and Stokes's friction force, i.e., $6\pi\eta_{\text{eff}} a v = (4\pi/3)a^3(\varrho - \varrho_{\text{fl}})g$, and we obtain

$$v = \frac{2}{9} \frac{(\varrho - \varrho_{\text{fl}})a^2 g}{\eta_{\text{eff}}} \to 10 \frac{\mu\text{m}}{\text{s}} . \tag{6.7}$$

To arrive at the estimate, we choose $\eta_{\text{eff}} = 0.1$ P and $a = 10\,\mu$m. We take $\varrho = 1$ g/cm^3 as the mass density of the particle and $\varrho - \varrho_{\text{fl}} = 0.01$ g/cm^3 as its difference to the surrounding fluid [202]. Thirdly, we consider the Brownian motion of a suspended particle. With the time $t = a^2/6D$ that the particle needs to diffuse a distance equal to the particle radius a [202], we define an averaged velocity

$$v = \frac{a}{t} = \frac{6D}{a} \to 10^{-3} \frac{\mu\text{m}}{\text{s}} . \tag{6.8}$$

The estimate was calculated using the Stokes–Einstein relation of Eq. (6.3) with thermal energy $k_B T = 4 \times 10^{-14}$ erg at room temperature and the same viscosity and particle radius as above.

After we have shown that $Er \ll 1$ is a reasonable assumption, we proceed as follows. We first calculate the static director field around a sphere from the balance of the elastic torques, $\boldsymbol{n} \times \boldsymbol{h}^0 = \boldsymbol{0}$ [see Eqs. (2.19) and (2.25)]. It corresponds to a minimization of the free energy. For $\boldsymbol{v} = \boldsymbol{0}$, the static director field defines a static pressure p_0 via the momentum balance, $-\nabla p_0 + \operatorname{div} \boldsymbol{T}^0 = 0$, where the elastic stress tensor $\boldsymbol{T}^0$ depends on the gradient of $\boldsymbol{n}$ [see Eqs. (2.18) and (2.11)]. If we again divide the total pressure into its static and hydrodynamic part, $p = p_0 + p'$, the velocity field is determined from the same set of equations as in (6.1), provided that we employ the viscous stress tensor $\boldsymbol{T}'$ of a nematic liquid crystal [see Eq. (2.22)]. In the case of an inhomogeneous director field, both the different shear viscosities and the rotational viscosity γ_1, discussed in Section 2.3, contribute to the Stokes drag.

In general, the friction force $\boldsymbol{F}_S$ does not point along $\boldsymbol{v}_\infty$, and the friction coefficient is now a tensor $\boldsymbol{\gamma}$. In the following, all our configurations are rotationally symmetric about the z axis, and the Stokes drag assumes the form

$$\boldsymbol{F}_S = \boldsymbol{\gamma} \boldsymbol{v}_\infty \quad \text{with } \boldsymbol{\gamma} = \gamma_\perp \boldsymbol{1} + (\gamma_\parallel - \gamma_\perp) \boldsymbol{e}_z \otimes \boldsymbol{e}_z \, . \tag{6.9}$$

There only exist two independent components $\gamma_\parallel$ and $\gamma_\perp$ for a respective flow parallel or perpendicular to the symmetry axis. In these two cases, the Stokes drag is parallel to $\boldsymbol{v}_\infty$. Otherwise, a component perpendicular to $\boldsymbol{v}_\infty$, called *lift force*, appears. In analogy with the isotropic fluid, we introduce effective viscosities $\eta_{\text{eff}}^\parallel$ and $\eta_{\text{eff}}^\perp$ via

$$\gamma_\parallel = 6\pi\eta_{\text{eff}}^\parallel a \quad \text{and} \quad \gamma_\perp = 6\pi\eta_{\text{eff}}^\perp a \, . \tag{6.10}$$

It is sufficient to determine the velocity and pressure fields for two particular geometries with $\boldsymbol{v}_\infty$ either parallel or perpendicular to the z axis. Then, the friction coefficients are calculated with the help of the dissipated energy per unit time [see Eq. (2.27)] [11,57]:

$$F_S^{\parallel/\perp} v_\infty = \int (\boldsymbol{T}' \cdot \boldsymbol{A} + \boldsymbol{h}' \cdot \boldsymbol{N}) \, \mathrm{d}^3 r \, . \tag{6.11}$$

It turns out that the alternative method via an integration of the stress tensor at the surface of the particle is numerically less reliable. Note that the velocity and pressure fields for an arbitrary angle between $\boldsymbol{v}_\infty$ and $\boldsymbol{e}_z$ follow from superpositions of the solutions for the two selected geometries. This is due to the linearity of our equations.

It is clear that the Brownian motion in an environment with an overall rotational symmetry is governed again by two independent diffusion constants. The generalized Stokes–Einstein formula of the diffusion tensor $\boldsymbol{D}$ takes the form

$$\boldsymbol{D} = D_\perp \boldsymbol{1} + (D_\parallel - D_\perp) \boldsymbol{e}_z \otimes \boldsymbol{e}_z \quad \text{with } D_{\parallel/\perp} = \frac{k_\mathrm{B} T}{\gamma_{\parallel/\perp}} \, . \tag{6.12}$$

At the end, we add some critical remarks about our approach which employs the static director field. From the balance equation of the elastic and viscous torques [see Eqs. (2.19), (2.25) and (2.26)], we derive that the change $\delta \boldsymbol{n}$ of the director due to the velocity $\boldsymbol{v}$ is of the order of the Ericksen number: $\delta n \sim Er$. This adds a correction $\delta \boldsymbol{T}^0$ to the elastic stress tensor $\boldsymbol{T}^0$ in the momentum balance equation. In the case of a spatially uniform director field, the correction $\delta \boldsymbol{T}^0$ is by a factor Er smaller than the viscous forces, and it can be neglected. However, for a non-uniform director field, it is of the same order as the viscous term, and, strictly speaking,

should be taken into account. Since our problem is already very complex, even when the directors are fixed, we keep this approximation for a first approach to the Stokes drag. How the friction force changes when the director field is allowed to relax, must be investigated by even more elaborate calculations. Two remarks support the validity of our approach. First, far away from the sphere, $\delta \boldsymbol{n}$ has to decay at least linearly in $1/r$, and $\delta \boldsymbol{T}_0$ is negligible against the viscous forces. Secondly, the non-linear term in the Navier–Stokes equations usually is omitted for $Re \ll 1$. However, whereas the friction and the pressure force for the Stokes problem decay as $1/r^3$, the non-linear term is proportional to $1/r^2$, exceeding the first two terms in the farfield. Nevertheless, performing extensive calculations, Oseen could prove that the correction of the non-linear term to the Stokes drag is of the order of Re [217]. One might speculate that the full relaxation of the director field introduces a correction of the order of Er to the Stokes drag.

6.3. Summary of numerical details

In this subsection we only review the main ideas of our numerical method. A detailed account will be given in Ref. [228].

The numerical investigation is performed on a grid which is defined by modified spherical coordinates. Since the region outside the spherical particle is infinitely extended, we employ a reduced radial coordinate $\xi = a/r$. The velocity and director fields are expressed in the local spherical coordinate basis. With this choice of coordinates, the momentum balance of Eqs. (6.1) with the viscous stress tensor of a nematic becomes very complex. We, therefore, used the algebraic program Maple to formulate it.

The two equations in (6.1) are treated by different numerical techniques. Given an initial velocity field, the momentum balance including the inertial term $\partial \boldsymbol{v}/\partial t$ can be viewed as a relaxation equation towards the stationary velocity field, which we aim to determine. The Newton–Gauss–Seidel method, introduced in Section 2.2, provides an effective tool to implement this relaxation. Employing the discretized version of the momentum balance equation, the velocity at the grid point $\boldsymbol{r}$ relaxes according to

$$v_i^{\mathrm{new}}(\boldsymbol{r}) = v_i^{\mathrm{old}}(\boldsymbol{r}) - \frac{[-\nabla p' + \operatorname{div} \boldsymbol{T}']_i}{[\partial(-\nabla p' + \operatorname{div} \boldsymbol{T})]_i/\partial v_i(\boldsymbol{r})} \,. \tag{6.13}$$

Note that the denominator can be viewed as the inverse of a variable time step for the fictitious temporal dynamics of $\boldsymbol{v}$.

A relaxation equation for the pressure involving $\operatorname{div} \boldsymbol{v} = 0$ is motivated by the method of artificial compressibility [33]. Let us consider the complete mass-balance equation. For small variations of the density, we obtain

$$\frac{\partial p}{\partial t} = -\frac{\varrho}{c^2} \operatorname{div} \boldsymbol{v} \quad \text{with } c = \sqrt{\frac{\partial p}{\partial \varrho}} \,. \tag{6.14}$$

The quantity c denotes the sound velocity for constant temperature, and c^2/ϱ is the isothermal compressibility. In discretized form we have

$$p^{\mathrm{new}} = p^{\mathrm{old}} - \frac{\varrho}{c^2} \Delta t \operatorname{div} \boldsymbol{v} \,. \tag{6.15}$$

Note that the reduced fictitious time step $\varrho\,\Delta t/c^2$ cannot be chosen according to the Newton–Gauss–Seidel method since $\operatorname{div} \boldsymbol{v}$ does not contain the pressure p. Instead, it should be as large as possible to speed up the calculations. In Ref. [187] upper bounds are given beyond which the numerical scheme becomes unstable.

To obtain the friction coefficient $\gamma_{\|}$, an effective two-dimensional problem has to be solved due to the rotational symmetry of the director configurations about the z axis. In the case of $\gamma_{\perp}$ ($\boldsymbol{v}_{\infty} \perp \boldsymbol{e}_z$), the velocity field possesses at least two mirror planes which are perpendicular to each other and whose line of intersection is the z axis. As a result, the necessary three-dimensional calculations can be reduced to one quadrant of the real space. A description of all the boundary conditions will be presented in Ref. [228].

The director fields for the topological dipole and the Saturn ring are provided by the respective ansatz functions of Eqs. (22) and (33) in Ref. [140]. The parameters of minimum free energy are chosen. In Section 4 we showed that these ansatz functions give basically the same results as the numerical investigation.

We checked our programs in the isotropic case. It turned out that the three-dimensional version is not completely stable for an infinitely extended integration area. We therefore solved Eqs. (6.1) in a finite region of reduced radius $r/a = 1/\varepsilon = 32$. For $\varepsilon = 1/32$, our programs reproduced the isotropic Stokes drag, calculated from Eq. (6.4), with an error of 1%.

6.4. Results, discussion, and open problems

We begin with an investigation of the stream line patterns, discuss the effective viscosities, and formulate some open problems at the end.

6.4.1. Stream line patterns

In Fig. 27 we compare the stream line patterns around a spherical particle for an isotropic liquid and a spatially uniform director field parallel to $\boldsymbol{v}_{\infty}$. A uniform $\boldsymbol{n}$ can be achieved by weak surface anchoring and application of a magnetic field with a magnetic coherence length smaller than the particle radius. In the isotropic fluid the bent stream lines occupy more space around the particle, whereas for a uniform director configuration they seem to follow the vertical director field lines as much as possible. This can be understood from a minimum principle. In Section 2.3 we explained that a shear flow along the director possesses the smallest shear viscosity, called η_b. Hence, in such a geometry the smallest amount of energy is dissipated. Indeed, for a uniform director field, one can derive the momentum balance from a minimization of the dissipation function stated in Eq. (2.27) [104]. A term $-2p\operatorname{div}\boldsymbol{v}$ has to be added because of the incompressibility of the fluid. It turns out that the Lagrange multiplier $-2p$ is determined by the pressure p.

In the case of the topological dipole parallel to $\boldsymbol{v}_{\infty}$, we observe a clear asymmetry in the stream lines as illustrated in Fig. 28. The dot indicates the position of the point defect. It breaks the mirror symmetry of the stream line pattern, which exists, e.g., in an isotropic liquid relative to a plane perpendicular to the vertical axis. In the farfield of the velocity, the splay deformation in the dipolar director configuration is clearly recognizable. Since we use the linearized momentum balance in $\boldsymbol{v}$, the velocity field is the same no matter if the fluid flows upward or downward. The stream line pattern of the Saturn ring [see Fig. 29 (right)] exhibits the mirror symmetry,

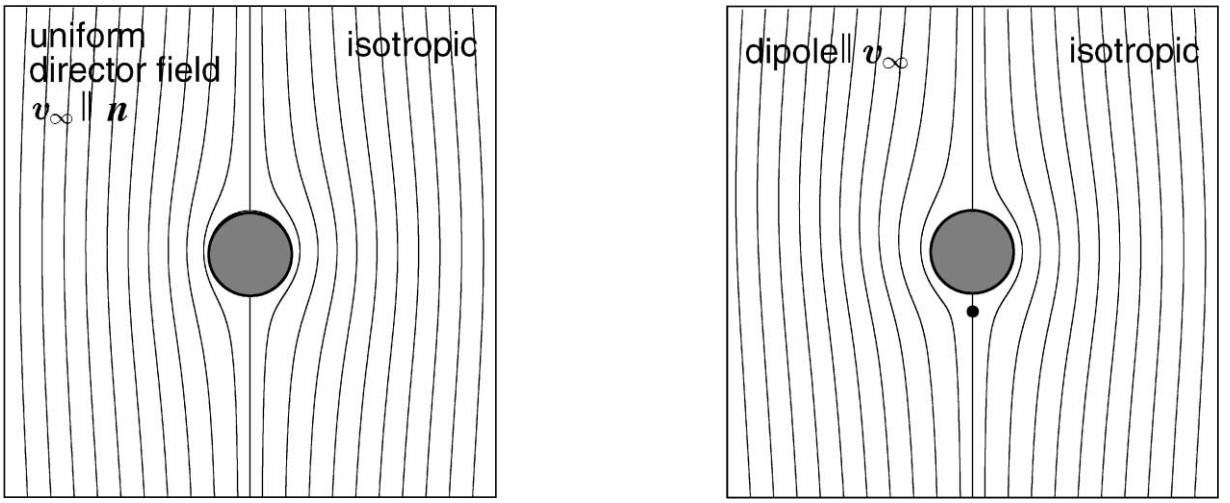

Fig. 27. Stream line pattern around a spherical particle for an isotropic liquid (right) and a uniform director field parallel to $\boldsymbol{v}_\infty$ (left).

Fig. 28. Stream line pattern around a spherical particle for an isotropic liquid (right) and the topological dipole parallel to $\boldsymbol{v}_\infty$ (left).

and the position of the ring disclination is visible by a dip in the stream line close to the equator of the sphere.

If $\boldsymbol{v}_\infty$ is perpendicular to the dipole axis, the missing mirror plane of the dipole configuration is even more pronounced in the stream line pattern. It is illustrated in Fig. 30, where the point defect is indicated by a dip in the stream line. Although the pattern resembles the one of the Magnus effect [217], symmetry dictates that $F_S^\perp \| \boldsymbol{v}_\infty$. A lift force perpendicular to $\boldsymbol{v}_\infty$ does not exist. We find a non-zero viscous torque acting on the particle whose direction for a fluid flow from left to right is indicated in Fig. 30. Symmetry allows such a torque $\boldsymbol{M}$ since the cross product of the dipole moment $\boldsymbol{p}$ and $\boldsymbol{v}_\infty$ gives an axial or pseudovector $\boldsymbol{M} \propto \boldsymbol{p} \times \boldsymbol{v}_\infty$. In the Saturn-ring configuration a non-zero dipole moment and, therefore, a non-zero torque cannot occur.

6.4.2. Effective viscosities

In Table 1 we summarize the effective viscosities of the Stokes drag, defined in Eq. (6.10), for a uniform director field, the dipole and the Saturn-ring configuration. The values are calculated for the two compounds MBBA and 5CB. For a reference, we include the three Mięsowicz viscosities. In the case of $\boldsymbol{v}_\infty$ parallel to the symmetry axis of the three configurations, we might expect that $\eta_{\text{eff}}^{\parallel}$ is close to η_b as argued by Cladis et al. [234]. For a uniform director field, $\eta_{\text{eff}}^{\parallel}$ exceeds η_b by 30% or 60%, respectively. The increase originates in the stream lines bending around the particle. The effective viscosity $\eta_{\text{eff}}^{\parallel}$ of the dipole and the Saturn ring are larger than η_b by an approximate factor of two. In addition to the bent stream lines, there exist

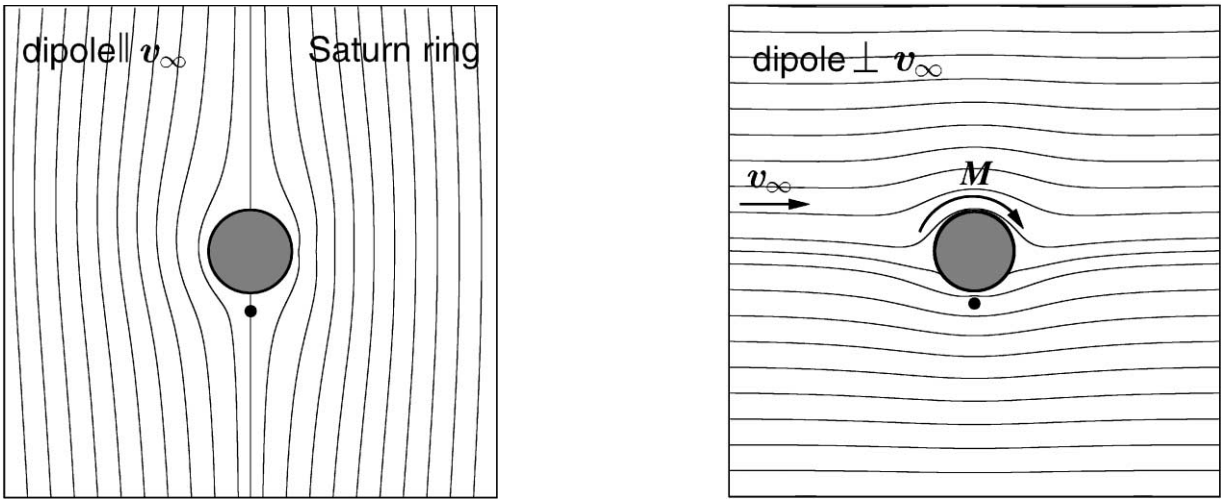

Fig. 29. Stream line pattern around a spherical particle for the Saturn ring (right) and the topological dipole (left) with their respective symmetry axis parallel to $\boldsymbol{v}_\infty$.

Fig. 30. Stream line pattern around a spherical particle for the topological dipole perpendicular to $\boldsymbol{v}_\infty$.

Table 1
Effective viscosities of the Stokes drag for the two compounds MBBA and 5CB and for three different director configurations. As a reference, the three Mięsowicz viscosities are included

	MBBA: $\eta_a = 0.416\,\mathrm{P}$, $\eta_b = 0.283\,\mathrm{P}$, $\eta_c = 1.035\,\mathrm{P}$			5CB: $\eta_a = 0.374\,\mathrm{P}$, $\eta_b = 0.229\,\mathrm{P}$, $\eta_c = 1.296\,\mathrm{P}$		
	Uniform $\boldsymbol{n}$	Dipole	Saturn ring	Uniform $\boldsymbol{n}$	Dipole	Saturn ring
$\eta_{\mathrm{eff}}^{\parallel}$ (P)	0.380	0.517	0.493	0.381	0.532	0.501
$\eta_{\mathrm{eff}}^{\perp}$ (P)	0.684	0.767	0.747	0.754	0.869	0.848
$\eta_{\mathrm{eff}}^{\perp}/\eta_{\mathrm{eff}}^{\parallel}$	1.80	1.48	1.51	1.98	1.63	1.69

strong director distortions close to the particle which the fluid has to flow through constantly changing the local direction of the moving molecules. Recalling our discussion of the permeation in Section 2.3, a contribution from the rotational viscosity γ_1 arises which does not exist in a uniform director field. In all three cases, we find $\eta_{\mathrm{eff}}^{\parallel}$ either close to or larger than η_a, so that η_b is not the only determining quantity of $\eta_{\mathrm{eff}}^{\parallel}$, as argued by Cladis et al. [234]. For $\boldsymbol{v}_\infty$ perpendicular to the symmetry axis, $\eta_{\perp}^{\mathrm{eff}}$ assumes a value between η_a and η_c, which is understandable since the flow velocity is mainly perpendicular to the director field.

The ratio $\eta_{\mathrm{eff}}^{\perp}/\eta_{\mathrm{eff}}^{\parallel}$ for the uniform director field is the largest since the extreme cases of a respective flow parallel or perpendicular to the director field is realized the best in this configuration. Furthermore, both the dipole and the Saturn ring exhibit nearly the same anisotropy, and we conclude that they cannot be distinguished from each other in a falling-ball experiment.

The ratios $\eta_{\mathrm{eff}}^{\perp}/\eta_{\mathrm{eff}}^{\parallel}$ that we determine for the Saturn ring and the uniform director field in the case of the compound MBBA agree well with the results of Ruhwandl and Terentjev who find $\eta_{\mathrm{eff}}^{\perp}/\eta_{\mathrm{eff}}^{\parallel}|_{\mathrm{uniform}} = 1.69$ and $\eta_{\mathrm{eff}}^{\perp}/\eta_{\mathrm{eff}}^{\parallel}|_{\mathrm{Saturn}} = 1.5$ [199]. However, they differ from the findings of Billeter and Pelcovits in their molecular dynamics simulations [10].

In the ansatz function of the dipolar configuration, we vary the separation r_{d} between the hedgehog and the center of the particle. Both the effective viscosities increase with r_{d} since the non-uniform director field with its strong distortions occupies more space. However, the ratio $\eta_{\mathrm{eff}}^{\perp}/\eta_{\mathrm{eff}}^{\parallel}$ basically remains the same. For the Saturn ring, $\eta_{\mathrm{eff}}^{\parallel}$ increases stronger with the radius r_{d} than does $\eta_{\mathrm{eff}}^{\perp}$. This seems to be reasonable since a flow perpendicular to the plane of the Saturn ring experiences more resistance than a flow parallel to the plane. As a result, $\eta_{\mathrm{eff}}^{\perp}/\eta_{\mathrm{eff}}^{\parallel}$ decreases when the ring radius r_{d} is enlarged.

6.4.3. Open problems

One should try to perform a complete solution of the Ericksen–Leslie equations including a relaxation of the static director field for $\boldsymbol{v} \neq \boldsymbol{0}$. In the case of $Er \ll 1$, a linearization in the small deviation $\delta\boldsymbol{n}$ from the static director field would suffice. Such a procedure helps to gain insight into several open problems. First, it verifies or falsifies the hypothesis that the correction to the Stokes drag is of the order of Er. Secondly, the Stokes drag of the topological dipole is the same whether the flow is parallel or anti-parallel to the dipole moment. This is also true for an object with a dipolar shape in an isotropic fluid. If such an object is slightly turned away from its orientation parallel to $\boldsymbol{v}_\infty$, it will experience a viscous torque and either relax back or reverse its direction to find its absolute stable orientation. The topological dipole will not turn around since it experiences an elastic torque towards its initial direction, as explained in Section 5.1. Nevertheless, a full solution of the Ericksen–Leslie equations would show whether and how much the dipole deviates from its preferred direction under the influence of a velocity field. It would also clarify its orientation when $\boldsymbol{v}_\infty$ is perpendicular to the dipolar axis. Furthermore, we speculate that the non-zero viscous torque, discussed in Section 6.4.1, is cancelled by elastic torques.

Preliminary results [228] for the two-dimensional problem with the relaxation of the director field included show that the Stokes drag of the dipolar configuration varies indeed linearly in Er for $Er < 1$. Furthermore, it is highly non-linear depending on $\boldsymbol{v}_\infty$ being either parallel or anti-parallel to the topological dipole.

The Stokes drag of particles in a nematic environment still presents a challenging problem to theorists. On the other hand, clear measurements of, e.g., the anisotropy in Stokes's friction force are missing.

7. Colloidal dispersions in complex geometries

In this section we present a numerical investigation of water droplets in a spherically confined nematic solvent. It is motivated by experiments on multiple nematic emulsions which we reported in Section 3.2. However, it also applies to solid spherical particles. Our main purpose is to demonstrate that the topological dipole provides a key unit for the understanding of multiple emulsions. In Sections 7.1–7.3 we first state the questions and main results of our investigation.

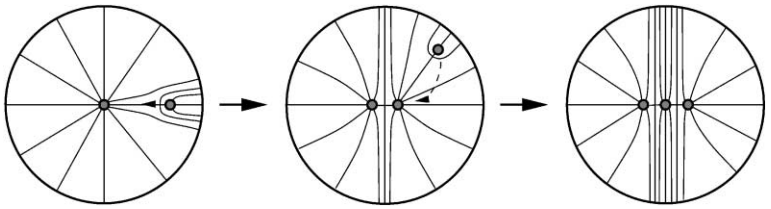

Fig. 31. Scenario to explain the chaining of water droplets in a large nematic drop. The right water droplet and its companion hyperbolic hedgehog form a dipole, which is attracted by the strong splay deformation around the droplet in the center (left picture). The dipole moves towards the center until at short distances the repulsion mediated by the point defect sets in (middle picture). A third droplet moves to the region of maximum splay to form a linear chain with the two other droplets.

Then we define the geometry of our problem and summarize numerical details. In particular, we employ the numerical method of finite elements [227] which is most suitable for non-trivial geometries. Finally we present our results in detail and discuss them. The last subsection contains an analytical treatment of the twist transition of a radial director field enclosed between two concentric spheres. It usually occurs when the inner sphere is not present. We perform a linear stability analysis and thereby explain the observation that a small water droplet at the center of a large nematic drop suppresses the twisting.

7.1. Questions and main results

In our numerical investigation we demonstrate that the dipolar configuration formed by one spherical particle and its companion hyperbolic point defect also exists in more complex geometries, e.g., nematic drops. This provides an explanation for the chaining reported in Section 3.2 and in Refs. [182,183]. One water droplet fits perfectly into the center of a large nematic drop, which has a total topological charge $+1$. Any additional water droplet has to be accompanied by a hyperbolic hedgehog in order not to change the total charge. If the dipole forms (see Fig. 31, left), it is attracted by the strong splay deformation in the center, as predicted by the phenomenological theory of Section 5.1 and in Refs. [182,140], until the short-range repulsion mediated by the defect sets in (see Fig. 31, middle). Any additional droplet seeks the region of maximum splay and forms a linear chain with the two other droplets. In the following we present a detailed study of the dipole formation in spherical geometries. For example, when the two water droplets in the middle picture of Fig. 31 are moved apart symmetrically about the center of the large drop, the dipole forms via a second-order phase transition. We also identify the dipole in a bipolar configuration which occurs for planar boundary conditions at the outer surface of the nematic drop. Two boojums, i.e., surface defects appear [145,26,120], and the dipole is attracted by the strong splay deformation in the vicinity of one of them [182,183,140]. Besides the dipole we find another stable configuration in this geometry, where the hyperbolic hedgehog sits close to one of the boojums, which leads to a hysteresis in the formation of the dipole.

In the experiment it was found that the distance d of the point defect from the surface of a water droplet scales with the radius r of the droplet like $d \approx 0.3r$ [182,183]. In the following we will call this relation the scaling law. By our numerical investigations, we confirm this scaling

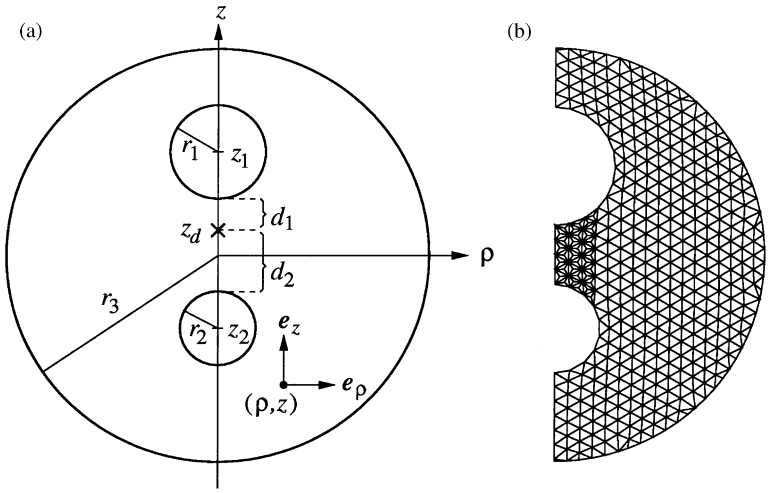

Fig. 32. (a) Geometry parameters for two water droplets with respective radii r_1 and r_2 in a large nematic drop with radius r_3. The system is axially symmetric about the z axis, and cylindrical coordinates ρ,z are used. The coordinates z_1, z_2, and z_d are the respective positions of the two droplets and the hyperbolic hedgehog. The two distances of the hedgehog from the surfaces of the droplets are d_1 and d_2. From Ref. [220]. (b) Triangulation of the integration area (lattice constant: $b = 0.495$). Between the small spheres a refined net of triangles is chosen. From Ref. [220].

law within an accuracy of ca. 15%, and we discuss the influence of the outer boundary of the large drop. Finally, we show that water droplets can repel each other without a hyperbolic defect placed between them.

7.2. Geometry and numerical details

We numerically investigate two particular geometries of axial symmetry. The first problem is defined in Fig. 32a. We consider two spherical water droplets with respective radii r_1 and r_2 in a large nematic drop with radius r_3. The whole system possesses axial symmetry, so that the water droplets and the hyperbolic hedgehog, indicated by a cross, are located always on the z axis. We employ a cylindrical coordinate system. The coordinates z_1, z_2, and z_d denote, respectively, the positions of the centers of the droplets and of the hyperbolic hedgehog on the z axis. The distances of the hedgehog from the surfaces of the two water droplets are, respectively, d_1 and d_2. Then, the quantity $d_1 + d_2$ means the distance of the two small spheres, and the point defect is situated in the middle between them if $d_1 = d_2$. We, furthermore, restrict the nematic director to the (ρ,z) plane, which means that we do not allow for twist deformations. [3]

[3] In nematic droplets with homeotropic anchoring a twist in the director field is usually observed (see [26] and Section 7.4). In Section 4.3.2 we demonstrated that it even appears in the dipole configuration close to the hyperbolic hedgehog. However, for the Frank elastic constants of 5CB, the distance of the defect from the surface of the water droplet differs only by 10% if the director field is not allowed to twist. We do not expect a different behavior in the geometry under consideration in this section. Here, we want to concentrate, as a first step, on the principal features of the system. Therefore, we neglect twist deformations to simplify the numerics. The same simplification to catch the main behavior of nematic drops in a magnetic field was used by other authors, see, e.g., [115,114].

The director is expressed in the local coordinate basis of the cylindrical coordinate system, $\boldsymbol{n}(\rho,z)=\sin\Theta(\rho,z)\boldsymbol{e}_\rho+\cos\Theta(\rho,z)\boldsymbol{e}_z$, where we introduced the *tilt angle* Θ. It is always restricted to the range $[-\pi/2,\pi/2]$ to ensure the $\boldsymbol{n}\rightarrow-\boldsymbol{n}$ symmetry of the nematic phase. At all the boundaries we assume a rigid homeotropic anchoring of the director, which allows us to omit any surface term in the free energy. In Ref. [140] it was shown that rigid anchoring is justified in our system and that any deformation of the water droplets can be neglected.

In the second problem we have only one water droplet insider a large nematic drop. We use the same coordinates and lengths as described in Fig. 32a, but omit the second droplet. The anchoring of the director at the outer surface of the large nematic sphere is rigid planar. At the surface of the small sphere we again choose a homeotropic boundary condition.

Because of the non-trivial geometry of our problem, we decided to employ the method of finite elements [227], where the integration area is covered with triangles. We construct a net of triangles by covering our integration area with a hexagonal lattice with lattice constant b. Vertices of triangles that only partially belong to the integration area are moved onto the boundary along the radial direction of the appropriate sphere. As a result, extremely obtuse triangles occur close to the boundary. We use a relaxation mechanism to smooth out these irregularities. The final triangulation is shown in Fig. 32b. In the area between the small spheres, where the hyperbolic hedgehog is situated, the grid is further subdivided to account for the strong director deformations close to the point defect. The local refinement helps us to locate the minimum position of the defect between the spheres within a maximum error of 15% by keeping the computing time to a reasonable value [220].

In the following, we express the Frank free energy, introduced in Section 2.1, in units of K_3a and denote it by the symbol $\bar{F}$. The quantity a is the characteristic length scale of our system, typically several microns. The saddle-splay term, a pure surface term, is not taken into account. The Frank free energy is discretized on the triangular net. For details, we refer the reader to Ref. [220]. To find a minimum of the free energy, we start with a configuration that already possesses the hyperbolic point defect at a fixed position z_d and let it relax via the standard Newton–Gauss–Seidel method [187], which we illustrate in Eq. (2.16) of Section 2.2.

Integrating the free energy density over one triangle yields a line energy, i.e., an energy per unit length. As a rough estimate for its upper limit we introduce the line tension $F_l=(K_1+K_3)/2$ of the isotropic core of a disclination [51]. Whenever the numerically calculated local line energy is larger than F_l, we replace it by F_l. Note that F_l differs from Eq. (2.34). However, its main purpose is to stabilize the hyperbolic point defect against opening up to a disclination ring whose radius would be unphysical, i.e., larger than the values discussed in Section 2.4.2.

All our calculations are performed for the nematic liquid crystal pentylcyanobiphenyl (5CB), for which the experiments were done [182,183]. Its respective bend and splay elastic constants are $K_3=0.53\times10^{-6}$ dyn and $K_1=0.42\times10^{-6}$ dyn. The experimental ratio $r_3/r_{1/2}$ of the radii of the large and small drops is in the range 10–50 [182,183]. The difficulty is that we want to investigate details of the director field close to the small spheres which requires a fine triangulation on the length scale given by $r_{1/2}$. To keep the computing time to a reasonable value we choose the following lengths: $r_3=7$, $r_{1/2}=0.5$–2, and $b=0.195$ for the lattice constant of the grid. In addition, we normally use one step of grid refinement between the small spheres (geometry 1) or between the small sphere and the south pole of the large nematic drop (geometry 2). With such parameters we obtain a lattice with 2200–2500 vertices.

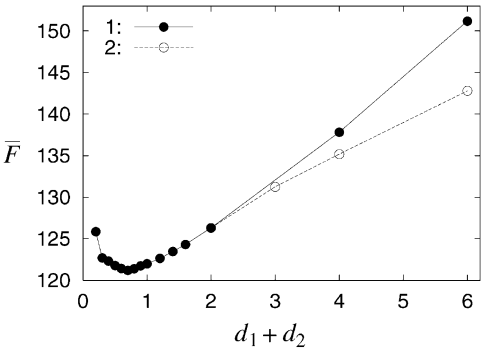

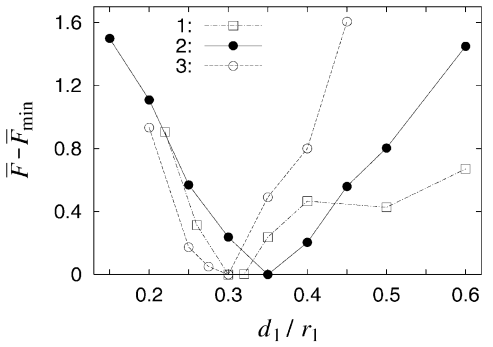

Fig. 33. The free energy $\bar{F}$ as a function of the distance $d_1 + d_2$ between the small spheres which are placed symmetrically about $z = 0$ ($r_1 = r_2 = 1$). Curve 1: $z_d = 0$, curve 2: position z_d of the defect can relax along the z axis. From Ref. [220].

Fig. 34. The free energy $\bar{F} - \bar{F}_{\min}$ as a function of $d_1/r_1 = d_2/r_2$. The small spheres are placed symmetrically about $z = 0$. Curve 1: $r_1 = r_2 = 0.5$, curve 2: $r_1 = r_2 = 1$, and curve 3: $r_1 = r_2 = 2$. From Ref. [220].

7.3. Results and discussion of the numerical study

In this subsection we discuss the results from our numerical investigation. First, we confirm the scaling law $d_{1/2} \approx 0.3 r_{1/2}$, which was observed in experiment, by varying the different lengths in our geometry. Secondly, we demonstrate that the topological dipole is also meaningful in complex geometries. Finally, we show that the hyperbolic hedgehog is not necessary to mediate a repulsion between the water droplets.

7.3.1. Scaling law

In Fig. 33 we plot the reduced free energy $\bar{F}$ as a function of the distance $d_1 + d_2$ between the surfaces of the small spheres, which are placed symmetrically about the center, i.e., $z_2 = -z_1$. Their radii are $r_1 = r_2 = 1$. Curve 1 shows a clear minimum at $d_1 + d_2 \approx 0.7$, the defect stays in the middle between the two spheres at $z_d = 0$. In curve 2 we move the defect along the z axis and plot the minimum free energy for each fixed distance $d_1 + d_2$. It is obvious that beyond $d_1 + d_2 = 2$ the defect moves to one of the small spheres. We will investigate this result in more detail in the following subsection.

In Fig. 34 we take three different radii for the small spheres, $r_1 = r_2 = 0.5, 1, 2$, and plot the free energy versus d_1/r_1 close to the minimum. Recall that d_1 is the distance of the hedgehog from the surface of sphere 1. Since for such small distances $d_1 + d_2$ the defect always stays at $z_d = 0$, i.e., in the middle between the two spheres, we have $d_1/r_1 = d_2/r_2$. The quantity $\bar{F}_{\min}$ refers to the minimum free energy of each curve. For each of the three radii we obtain an energetically preferred distance d_1/r_1 in the range of $[0.3, 0.35]$, which agrees well with the experimental value of 0.3. Why does a scaling law of the form $d_{1/2} = (0.325 \pm 0.025) r_{1/2}$ occur? When the small spheres are far away from the surface of the large nematic drop, its finite radius r_3 should hardly influence the distances d_1 and d_2. Then, the only length scale in the system is $r_1 = r_2$, and we expect $d_{1/2} \propto r_{1/2}$. However, in Fig. 34 the influence from the boundary of the

large sphere is already visible. Let us take curve 2 for spheres with radii $r_{1/2}=1$ as a reference. It is approximately symmetric about $d_1/r_1=0.35$. The slope of the right part of curve 3, which corresponds to larger spheres of radii $r_{1/2}=2$, is steeper than in curve 2. Also, the location of the minimum clearly tends to values smaller than 0.3. We conclude that the small spheres are already so large that they are strongly repelled by the boundary of the nematic drop. On the other hand, the slope of the right part of curve 1, which was calculated for spheres of radii $r_{1/2}=0.5$, if less steep than in curve 2. This leads to the conclusion that the boundary of the nematic drop has only a minor influence on such small spheres.

When we move the two spheres with radii $r_{1/2}=1$ together in the same direction along the z axis, the defect always stays in the middle between the droplets and obeys the scaling law. We have tested its validity within the range $[0,3]$ for the defect position z_d. Of course, the absolute minimum of the free energy occurs in the symmetric position of the two droplets, $z_2=-z_1$.

We further check the scaling law for $r_1\neq r_2$. We investigate two cases. When we choose $r_1=2$ and $r_2=0.6$, we obtain $d_{1/2}\approx 0.3r_{1/2}$. In the second case, $r_1=2$ and $r_2=1$, we find $d_1\approx 0.37r_1$ and $d_2\approx 0.3r_2$. As observed in the experiment, the defect sits always closer to the smaller sphere. There is no strong deviation from the scaling law $d_{1/2}=(0.325\pm 0.025)r_{1/2}$, although we would allow for it, since $r_1\neq r_2$.

7.3.2. *Identification of the dipole*

In this subsection we demonstrate that the topological dipole is meaningful in our geometry. We place sphere 2 with radius $r_2=1$ in the center of the nematic drop at $z_2=0$. Then, we determine the energetically preferred position of the point defect for different locations z_1 of sphere 1 ($r_1=1$). The position of the hedgehog is indicated by $\Delta=(d_2-d_1)/(d_1+d_2)$. If the defect is located in the middle between the two spheres, Δ is zero since $d_1=d_2$. On the other hand, if it sits at the surface of sphere 1, $d_1=0$, and Δ becomes one. In Fig. 35 we plot the free energy $\bar{F}$ versus Δ. In curve 1, where the small spheres are farthest apart from each other ($z_1=5$), we clearly find the defect close to sphere 1. This verifies that the dipole is existing. It is stable against fluctuations since a rough estimate of the thermally induced mean displacement of the defect yields 0.01. The estimate is performed in full analogy to Eq. (4.6) of Section 4.2. When sphere 1 is approaching the center (curve 2: $z_1=4$ and curve 3: $z_1=3.5$), the defect moves away from the droplet until it nearly reaches the middle between both spheres (curve 4: $z_1=3$). This means, the dipole vanishes gradually until the hyperbolic hedgehog is shared by both water droplets.

An interesting situation occurs when sphere 1 and 2 are placed symmetrically about $z=0$. Then, the defect has two equivalent positions on the positive and negative part of the z axis. In Fig. 36 we plot again the free energy $\bar{F}$ versus the position Δ of the defect. From curve 1 to 3 ($z_1=z_2=4,3,2.5$) the minimum in $\bar{F}$ becomes broader and more shallow. The defect moves closer towards the center until at $z_1=-z_2\approx 2.3$ (curve 4) it reaches $\Delta=0$. This is reminiscent to a symmetry-breaking second-order phase transition [27,124] which occurs when, in the course of moving the water droplets apart, the dipole starts to form. We take Δ as an order parameter, where $\Delta=0$ and $\Delta\neq 0$ describe, respectively, the high- and the low-symmetry phase. A Landau expansion of the free energy yields

$$\bar{F}(\Delta)=\bar{F}_0(z_1)+a_0[2.3-z_1]\Delta^2+c(z_1)\Delta^4\,, \tag{7.1}$$

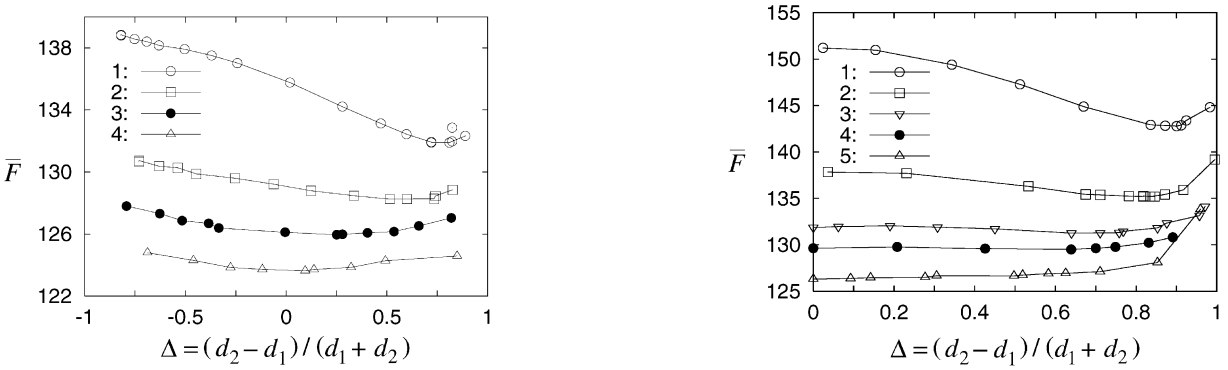

Fig. 35. The free energy $\bar{F}$ as a function of $\Delta = (d_2 - d_1)/(d_1 + d_2)$. Sphere 2 is placed at $z_2 = 0$. The position z_1 of sphere 1 is the parameter. Curve 1: $z_1 = 5$, curve 2: $z_1 = 4$, curve 3: $z_1 = 3.5$, and curve 4: $z_1 = 3$. The radii are $r_1 = r_2 = 1$. From Ref. [220].

Fig. 36. The free energy $\bar{F}$ as a function of $\Delta = (d_2 - d_1)/(d_1 + d_2)$. The small spheres are placed symmetrically about $z = 0$. Curve 1: $z_1 = -z_2 = 4$, curve 2: $z_1 = -z_2 = 3$, curve 3: $z_1 = -z_2 = 2.5$, curve 4: $z_1 = -z_2 = 2.3$, curve 5: $z_1 = -z_2 = 2$. The radii are $r_1 = r_2 = 1$. From Ref. [220].

where $z_1 = -z_2$ plays the role of the temperature. Odd powers in Δ are not allowed because of the required symmetry, $\bar{F}(\Delta) = \bar{F}(-\Delta)$. This free energy qualitatively describes the curves in Fig. 36. It should be possible to observe such a "second-order phase transition"[4] with a method introduced recently by Poulin et al. [179] to measure dipolar forces in inverted nematic emulsion. We already explained the method in Section 5.2 after Eq. (5.12). Two small droplets filled with a magnetorheological fluid are forced apart when a small magnetic field of about 100 G is applied perpendicular to the z axis. When the magnetic field is switched off, the two droplets move towards each other to reach the equilibrium distance. In the course of this process the phase transition for the dipole should be observable.

7.3.3. The dipole in a bipolar configuration

It is possible to change the anchoring of the director at the outer surface of the large nematic drop from homeotropic to planar by adding some amount of glycerol to the surrounding water phase [182]. Then the bipolar configuration for the director field appears [26,120], where two boojums [145], i.e., surface defects of charge 1 are situated at the north and south pole of the large nematic drop (see configuration (1) in Fig. 37). The topological point charge of the interior of the nematic drop is zero, and every small water droplet with homeotropic boundary condition has to be accompanied by a hyperbolic hedgehog. In the experiment the hedgehog sits close to the water droplet, i.e., the dipole exists and it is attracted by the strong splay deformation

[4] There is strictly speaking no true phase transition since our investigated system has finite size. However, we do not expect a qualitative change in Fig. 36, when the nematic drop is much larger than the enclosed water droplets ($r_3 \gg r_1, r_2$), i.e., when the system reaches the limit of infinite size.

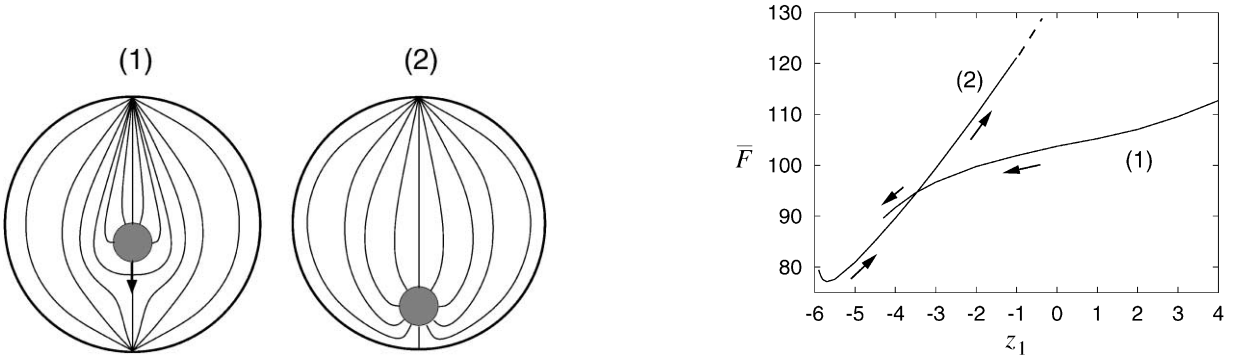

Fig. 37. Planar boundary conditions at the outer surface of the large sphere create boojums, i.e., surface defects at the north and the south pole. A water droplet with homeotropic boundary conditions nucleates a hyperbolic hedgehog. Two configurations exist that are either stable or metastable depending on the position of the water droplet; (1) the dipole, (2) the hyperbolic hedgehog sitting at the surface. From Ref. [220].

Fig. 38. The free energy $\bar{F}$ as a function of the position z_1 of the water droplet for the configurations (1) and (2). For $z_1 > -3.5$, (1) is stable, and (2) is metastable. The situation is reversed for $-4.3 < z_1 < -3.5$. Configuration (1) loses its metastability at $z_1 = -4.3$. From Ref. [220].

close to the south pole [182], as predicted by the phenomenological theory of Section 5 and Refs. [182,140].

A numerical analysis of the free energy $\bar{F}$ is in agreement with experimental observations but also reveals some interesting details which have to be confirmed. In Fig. 38 we plot $\bar{F}$ as a function of the position z_1 of the small water droplet with radius $r_1 = 1$. The diagram consists of curves (1) and (2), which correspond, respectively, to configurations (1) and (2) in Fig. 37. The free energy possesses a minimum at around $z_1 = -5.7$. The director field assumes configuration (2), where the hyperbolic hedgehog is situated at the surface of the nematic drop. Moving the water droplet closer to the surface, induces a repulsion due to the strong director deformations around the point defect. When the water droplet is placed far away from the south pole, i.e., at large z_1, the dipole of configuration (1) forms and represents the absolute stable director field. At $z_1 = -3.5$ the dipole becomes metastable but the system does not assume configuration (2) since the energy barrier the system has to overcome by thermal activation is much too high. By numerically calculating the free energy for different positions of the hedgehog, we have, e.g., at $z_1 = -4.0$, determined an energy barrier of $K_3 a \approx 1000 k_B T$, where k_B is the Boltzmann constant, T the room temperature, and $a \approx 1\,\mu m$. At $z_1 = -4.3$, the dipole even loses its metastability, the hyperbolic defect jumps to the surface at the south pole and the water droplet follows until it reaches its energetically preferred position. On the other hand, if it were possible to move the water droplet away from the south pole, the hyperbolic hedgehog would stay at the surface, since configuration (2) is always metastable for $z_1 \geqslant -3.5$. The energy barrier for a transition to the dipole is again at least $1000 k_B T$. We have also investigated the distance d_1 of the defect from the surface of the water droplet. For $z_1 \in [-2, 4]$, d_1 fluctuates between 0.3 and 0.35. For $z_1 < -2$, it increases up to 0.5 at $z_1 = -4.3$, where the dipole loses its metastability.

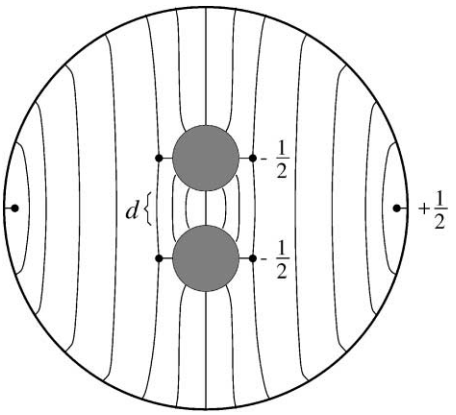

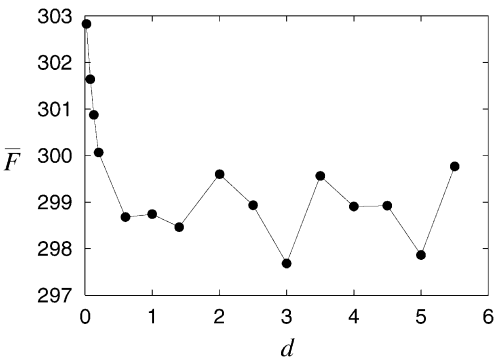

Fig. 39. An alternative, metastable configuration. Both droplets are surrounded by a $-1/2$ disclination ring which compensates the topological charge $+1$ of each droplet. An additional $+1/2$ disclination ring close to the surface of the nematic drop satisfies the total topological charge $+1$. From Ref. [220].

Fig. 40. The free energy $\bar{F}$ as a function of the distance d of the droplets. A repulsion for $d < 0.6$ is clearly visible. From Ref. [220].

7.3.4. Repulsion without defect

We return to the first geometry with two water droplets and homeotropic boundary conditions at all the surfaces. When we take either a uniform director field or randomly oriented directors as a starting configuration, our system always relaxes into the configuration sketched in Fig. 39. Both water droplets are surrounded in their equatorial plane by a $-1/2$ disclination ring which compensates the point charge $+1$ carried by each droplet. That means, each droplet creates a Saturn-ring configuration around it, which we introduced in Section 4.1 (see also Refs. [225,119]). To obtain the total point charge $+1$ of the nematic drop there has to be an additional topological defect with a point charge $+1$. In the numerically relaxed director field, we find a $+1/2$ disclination ring close to the outer surface. This configuration has a higher energy than the one with the hyperbolic hedgehog. It is only metastable. Since a transition to the stable configuration needs a complete rearrangement of the director field, the energy barrier is certainly larger than $K_{33}a \approx 1000 k_B T$. We, therefore, expect the configuration of Fig. 39 to be stable against thermal fluctuations. It would be interesting to search for it in an experiment.

We use the configuration to demonstrate that even without the hyperbolic hedgehog the two water droplets experience some repulsion when they come close to each other. In Fig. 40 we plot the free energy $\bar{F}$ versus the separation d of the two spheres. For large d, the free energy oscillates which we attribute to numerical artifacts. For decreasing d, the free energy clearly increases, and the water droplets repel each other due to the strong deformation of the director field lines connecting the two droplets.

7.4. Coda: twist transition in nematic drops

Already thirty years ago, in connection with nematic emulsions, the two main director configurations in a nematic drop were discussed both experimentally and theoretically [147,61]: for

homeotropic boundary conditions, a radial hedgehog at the center of the drop appears, whereas tangential surface anchoring leads to the bipolar structure already discussed above. The simple picture had to be modified when it was found that nematic drops in both cases also exhibit a twisted structure [26]. For the bipolar configuration, a linear stability analysis of the twist transition was performed [237]. A numerical study of the twisting in the radial structure of capillaries was presented in Refs. [185,186]. Lavrentovich and Terentjev proposed that the twisted director field in a nematic drop with homeotropic surface anchoring is given by a combination of a hyperbolic hedgehog at the center of the drop and a radial one at its periphery [126] as illustrated in Fig. 7 of Section 2.4.1. This configuration was analyzed by means of an ansatz function, and a criterion for the twist transition was given [126].

In this subsection we focus on the director field between two concentric spheres with perpendicular anchoring at both the surfaces and present a stability analysis for the radial configuration against axially symmetric deformations. In particular, we will derive a criterion for the twist transition, and we will show that even small spheres inside a large one are sufficient to avoid twisted configurations. This has been recently observed in the experiments on multiple nematic emulsions [182,183].

Throughout the paper we assume rigid surface anchoring of the molecules. In nematic emulsions it can be achieved by a special choice of the surfactant [182,183]. For completeness we note that in a single droplet for sufficiently weak anchoring strength an axial structure with an equatorial disclination ring appears [66,60].

In the following three subsections, we first expand the Frank free energy into small deviations from the radial configuration up to second order. Then, we formulate and solve the corresponding eigenvalue equation arising from a linear stability analysis. The lowest eigenvalue leads to a criterion for the twist transition. We close with a discussion of our results.

7.4.1. Expansion of the elastic energy

We consider the defect-free radial director configuration between two concentric spheres of radii $r_{\min}$ and $r_{\max}$ and assume rigid radial surface anchoring at all the surfaces. If the smaller sphere is missing, the radial director configuration exhibits a point defect at the center. We will argue below that this situation, $r_{\min} = 0$, is included in our treatment.

The twist transition reduces the $SO(3)$ symmetry of the radial director configuration to an axial C_∞ symmetry. In order to investigate the stability of the radial configuration $\boldsymbol{n}_0 = \boldsymbol{e}_r$ against a twist transition, we write the local director in a spherical coordinate basis, allowing for small deviations along the polar (θ) and the azimuthal (ϕ) direction:

$$\boldsymbol{n}(r,\theta) = (1 - \tfrac{1}{2}b^2 f^2 - \tfrac{1}{2}a^2 g^2)\boldsymbol{e}_r + ag\boldsymbol{e}_\theta + bf\boldsymbol{e}_\phi \ . \tag{7.2}$$

$f(r,\theta)$ and $g(r,\theta)$ are general functions which do not depend on ϕ due to our assumption of axial symmetry. The amplitudes a and b describe the magnitude of the polar and azimuthal deviation from the radial configuration. The second-order terms in a and b result from the normalization of the director.

The radial director field between the spheres only involves a splay distortion, and its Frank free energy is

$$F_{\text{radial}} = 8\pi K_{11}(r_{\max} - r_{\min}) \ , \tag{7.3}$$

where we did not include the saddle-splay energy. If an azimuthal ($b \neq 0$) or a polar component ($a \neq 0$) of the director is introduced, the splay energy can be reduced at costs of non-zero twist and bend contributions depending on the values of the Frank elastic constants K_1, K_2, and K_3. We expand the Frank free energy of the director field in Eq. (7.2) up to second order in a and b and obtain

$$\Delta F = 2\pi b^2 \int \mathrm{d}r \int \mathrm{d}\cos\theta[-4K_1(f^2 + r f_r f) + K_2(\cot\theta f + f_\theta)^2 + K_3(f + r f_r)^2] + 2\pi a^2 \int \mathrm{d}r \int \mathrm{d}\cos\theta[-4K_1(g^2 + r g_r g) + K_1(\cot\theta g + g_\theta)^2 + K_3(g + r g_r)^2] \quad (7.4)$$

as the deviation from F_{radial}. The respective subscripts $_r$ and $_\theta$ denote partial derivatives with respect to the corresponding coordinates. Note that there are no linear terms in a or b, i.e., the radial director field is always an extremum of the Frank free energy. Furthermore, there is no cross-coupling term ab in Eq. (7.4), and the stability analysis for polar and azimuthal perturbations can be treated separately. For example, for any function $f(r,\theta)$ leading to a negative value of the first integral in Eq. (7.4), the radial configuration ($a = b = 0$) is unstable with respect to a small azimuthal deformation ($b \neq 0$), which introduces a twist into the radial director field. Therefore, we will call it the twist deformation in the following. An analogous statement holds for $g(r,\theta)$ which introduces a pure bend into the radial director field. We are now determining the condition the elastic constants have to fulfil in order to allow for such functions $f(r,\theta)$ and $g(r,\theta)$. As we will demonstrate in the next subsection, the solution of this problem is equivalent to solving an eigenvalue problem.

7.4.2. Formulating and solving the eigenvalue problem

In a first step, we focus on the twist deformation ($b \neq 0$). We are facing the problem to determine for which values of K_1, K_2, and K_3 the functional inequality

$$\int \mathrm{d}r \int \mathrm{d}x \{K_2(1-x^2)[x f/(1-x^2) - f_x]^2 + (K_3 - 4K_1) f^2 + (2K_3 - 4K_1) r f_r f + K_3 r^2 f_r^2\} < 0 \quad (7.5)$$

possesses solutions $f(r,x)$. The left-hand side of the inequality is the first integral of Eq. (7.4) after substituting $x = \cos\theta$. After some manipulations (see Ref. [197]), we obtain

$$\frac{\int \mathrm{d}r \int \mathrm{d}x\,(K_2 f \mathscr{D}^{(x)} f + K_3 f \mathscr{D}^{(r)} f)}{\int \mathrm{d}r \int \mathrm{d}x\, f^2} < 2K_1\,, \quad (7.6)$$

where the second-order differential operators $\mathscr{D}^{(x)}$ and $\mathscr{D}^{(r)}$ are given by

$$\mathscr{D}^{(x)} = (1-x^2)\frac{\partial^2}{\partial x^2} + 2x\frac{\partial}{\partial x} + \frac{1}{1-x^2} \quad \text{and} \quad \mathscr{D}^{(r)} = -r^2\frac{\partial^2}{\partial r^2} - 2r\frac{\partial}{\partial r}\,. \quad (7.7)$$

The inequality in Eq. (7.6) is fulfilled the best when the left-hand side assumes a minimum. According to the Ritz principle in quantum mechanics, this minimum is given by the lowest

eigenvalue of the operator

$$K_2\mathscr{D}^{(x)} + K_3\mathscr{D}^{(r)} \tag{7.8}$$

on the space of square-integrable functions with $f(r_{\min},\theta)=f(r_{\max},\theta)=0$ for $0 \leqslant \theta \leqslant \pi$ (fixed boundary condition) and $f(r,0)=f(r,\pi)=0$ for $r_{\min} \leqslant r \leqslant r_{\max}$.

The eigenvalue equation of the operator $K_2\mathscr{D}^{(x)}+K_3\mathscr{D}^{(r)}$ separates into a radial and an angular part. The radial part is an Eulerian differential equation [20] with the lowest eigenvalue

$$\lambda_0^{(r)} = \frac{1}{4} + \left(\frac{\pi}{\ln(r_{\max}/r_{\min})}\right)^2 \tag{7.9}$$

and the corresponding eigenfunction

$$f^{(r)}(r) = \frac{1}{\sqrt{r}}\sin\left(\pi\frac{\ln(r/r_{\min})}{\ln(r_{\max}/r_{\min})}\right) . \tag{7.10}$$

The angular part of the eigenvalue equation is solved by the associated Legendre functions $P_n^{m=1}$. The lowest eigenvalue is $\lambda_0^{(x)}=2$, and the corresponding eigenfunction is $f^{(x)}(\theta)=P_1^1(\theta)=\sin\theta$.

With both these results, we obtain the instability condition for a twist deformation:

$$\frac{1}{2}\frac{K_3}{K_1}\left[\frac{1}{4} + \left(\frac{\pi}{\ln(r_{\max}/r_{\min})}\right)^2\right] + \frac{K_2}{K_1} < 1 . \tag{7.11}$$

This inequality is the main result of the paper. If it is fulfilled, the radial director field no longer minimizes the Frank free energy. Therefore it is a sufficient condition for the radial configuration to be unstable against a twist deformation. It is not a necessary condition since we have restricted ourselves to second-order terms in the free energy, not allowing for large deformations of the radial director field. Hence, we cannot exclude the existence of further configurations which, besides the radial, produce local minima of the free energy.

To clarify our last statement, we take another view. The stability problem can be viewed as a phase transition. Let us take K_3 as the "temperature". Then condition (7.11) tells us that for large K_3 the radial state is the (linearly) stable one. If the phase transition is second-order-like, the radial state loses its stability exactly at the linear stability boundary, while for a first-order-like transition the system can jump to the new state (due to non-linear fluctuations) even well inside the linear stability region. Thus, as long as the nature of the transition is not clear, linear stability analysis cannot predict for sure that the radial state will occur in the linear stability region. Furthermore, if the transition line is crossed, the linear stability analysis breaks down, and there could be a transition from the twisted to a new configuration. However, there is no experimental indication for such a new structure. Keeping this in mind, we will discuss the instability condition (7.11) in the next subsection.

We finish this subsection by noting that the elastic energy for a bend deformation ($a \neq 0$) has the same form as the one for the twist deformation ($b \neq 0$), however, with K_2 replaced by K_1. Therefore, we immediately conclude from (7.11) that the instability condition for a polar component ($a \neq 0$) in the director field (7.2) cannot be fulfilled for positive elastic constants. A director field with vanishing polar component is always stable in second order.

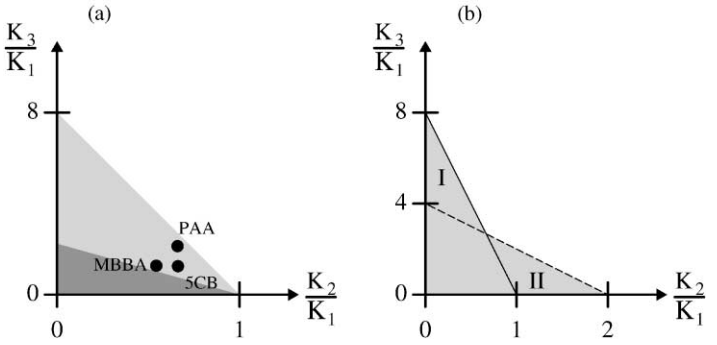

Fig. 41. (a) Stability diagram for the twist transition [cf. Eq. (7.11)]. The dark grey corresponds to the ratios of Frank constants where the radial configuration is unstable for a ratio $r_{max}/r_{min} = 50$. The light grey triangle is the region where the radial configuration is unstable for $r_{max}/r_{min} \geqslant 50$. The circles represent the elastic constants for the liquid crystal compounds MBBA, 5CB, and PAA. (b) A comparison between the regions of instability for a radial director field against twisting derived in this work (full line) and by Lavrentovich and Terentjev (dashed line) for $r_{max}/r_{min} \to \infty$. The regions differ by the areas I and II.

7.4.3. Discussion[5]

The instability condition (7.11) indicates for which values of the elastic constants K_1, K_2, and K_3 the radial configuration is expected to be unstable with respect to a twist deformation. The instability domain is largest for $r_{max}/r_{min} \to \infty$ and decreases with decreasing ratio r_{max}/r_{min}, i.e., a water droplet inside a nematic drop can stabilize the radial configuration.

In Fig. 41a, the instability condition (7.11) is shown. If the ratios of the Frank elastic constants define a point in the grey triangles, the radial configuration can be unstable depending on the ratio r_{max}/r_{min}. The dark grey area gives the range of the elastic constants where a twisted structure occurs for $r_{max}/r_{min} = 50$. With increasing ratio r_{max}/r_{min} the instability domain enlargens until it is limited by $K_3/(8K_1)+K_2/K_1 = 1$ for $r_{max}/r_{min} \to \infty$. The light grey triangle is the region where the radial configuration is unstable for $r_{max}/r_{min} > 50$ but where it is stable for $r_{max}/r_{min} < 50$.

The circles in Fig. 41a, represent, respectively, the elastic constants for the liquid crystal compounds MBBA, 5CB, and PAA. For 5CB the elastic constants are in the light grey domain, i.e., a twisted structure is expected for $r_{max}/r_{min} \to \infty$ (no inner sphere) but not for $r_{max}/r_{min} < 50$. Such a behavior has been recently observed in multiple nematic emulsions [182]. It has been found that a small water droplet inside a large nematic drop prevents the radial configuration from twisting.

Two examples of nematic drops observed under the microscope between crossed polarizers can be seen in Fig. 42. In the left image the director configuration is pure radial, in the right one it is twisted. The left drop contains a small water droplet that stabilizes the radial configuration according to Eq. (7.11). The water droplet is not visible in this image because of the limited resolution. A better image is presented in [182]. We have calculated the polarizing microscope picture of the twisted configuration by means of the 2×2 Jones matrix formalism [60]. We took the director field of Eq. (7.2) and used the eigenfunction of Eq. (7.10) with an amplitude

[5] Reprinted with permission from A. Rüdinger, H. Stark, Twist transition in nematic droplets: A stability analysis, Liq. Cryst. 26 (1999) 753. Copyright 1999 Taylor and Francis, http://www.tandf.co.uk.

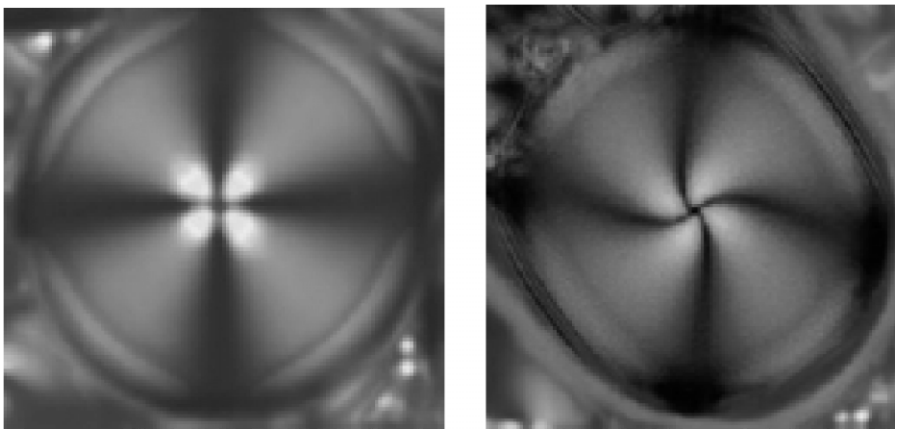

Fig. 42. Radial (left) and twisted (right) configuration of the director field in a nematic drop (diameter $\approx 20\,\mu m$) of 5CB observed under the microscope between crossed polarizers. In the radial configuration there is a small isotropic liquid droplet in the center of the nematic drop (invisible in this image).

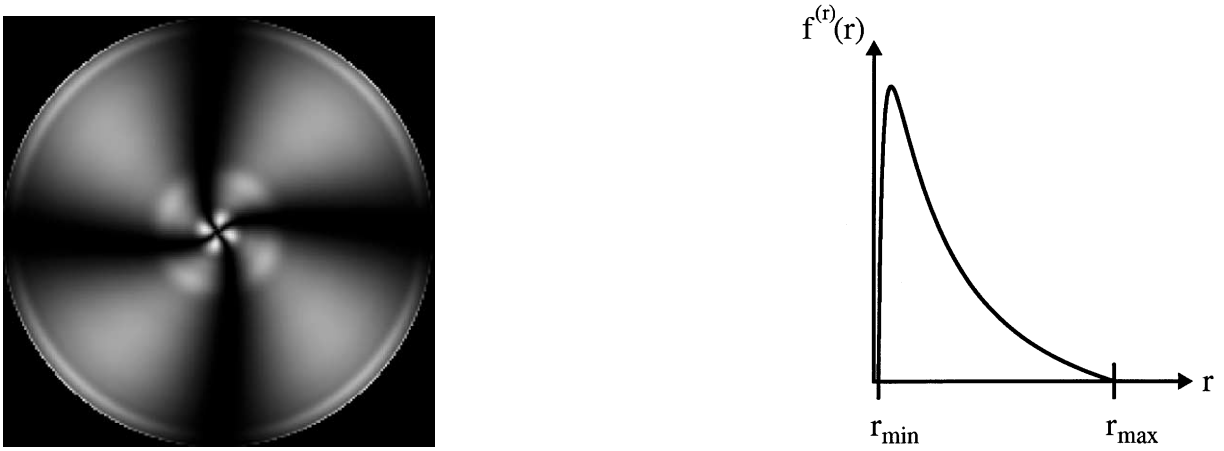

Fig. 43. Calculated transmission for the twisted configuration of the director field in a nematic drop whose diameter is 20 μm. The transmission amplitude was obtained by summing over 20 wave lengths between 400 and 800 nm. The amplitude b of the twist deformation was set to 0.15. This figure has to be compared to the right image of Fig. 42.

Fig. 44. Radial dependence of $f^{(r)}(r)$ [cf. Eq. (7.10)] for $r_{max}/r_{min} = 50$. The function is strongly peaked close to r_{min}.

$b = 0.15$. The result shown in Fig. 43 is in qualitative agreement with the experimental image on the right in Fig. 42.

In Fig. 44 we plot the radial part $f^{(r)}(r)$ [see Eq. (7.10)] of the eigenfunction $f(r,\theta) = f^{(r)}(r)f^{(x)}(\theta)$ governing the twist deformations. For large values of r_{max}/r_{min} it is strongly

peaked near $r_{\min}$. The maximum of $f^{(r)}(r)$ occurs at a radius r_0 which is given by

$$\ln \frac{r_0}{r_{\min}} = \frac{\ln(r_{\max}/r_{\min})}{\pi} \arctan \frac{2\pi}{\ln(r_{\max}/r_{\min})} . \tag{7.12}$$

Hence, for $r_{\max}/r_{\min} \gg 1$ the maximal azimuthal component $bf(r_0, \theta)$ of the director field is located at $r_0/r_{\min} = e^2 \approx 7.39$, i.e., close to the inner sphere. From the polarizing microscope pictures it can be readily seen that the twist deformation is largest near the center of the nematic drop. In the opposite limit, $r_{\max}/r_{\min} \approx 1$, the position of maximal twist is at the geometric mean of $r_{\min}$ and $r_{\max}$: $r_0 = (r_{\min} r_{\max})^{1/2}$.

In the limit $r_{\min} \to 0$, where the inner sphere is not existing, a point defect with a core radius r_c is located at $r = 0$. In this case our boundary condition, $f^{(r)}(r_{\min}) = 0$, makes no sense since the director is not defined for $r < r_c$. Fortunately, for $r_{\min} \to 0$ the lowest eigenvalue of the operator (7.8) and therefore the instability condition is insensitive to a change of the boundary condition. Furthermore, the shape of the eigenfunction is also independent of the boundary condition, in particular its maximum is always located close to $r_{\min}$.

A last comment concerns the work of Lavrentovich and Terentjev [126]. In Fig. 41b, we plot as a dashed line the criterion, $K_3/(4K_1) + K_2/(2K_1) = 1$, which the authors of Ref. [126] derived for the twist transition in the case $r_{\max}/r_{\min} \to 0$. They constructed an ansatz function which connects a hyperbolic hedgehog at the center via a twist deformation to a radial director field at the periphery of a nematic drop. Then they performed a stability analysis for an appropriately chosen order parameter. The region of instability calculated in this article and their result differ by the areas I and II. This is due to the complementarity of the two approaches. While the authors of Ref. [126] allow for large deviations with respect to the radial configuration at the cost of fixing an ansatz function, we allow the system to search the optimal configuration (i.e., eigenfunction) for small deformations. We conclude that both results together give a good approximation of the region of instability for the radial configuration against twisting. However, we cannot exclude that a full non-linear analysis of the problem leads to a change in the stability boundaries.

In conclusion, we have performed a stability analysis of the radial configuration in nematic drops with respect to a twist deformation. Assuming strong perpendicular anchoring at all the surfaces, we have derived an instability condition in terms of the Frank constants. We could show that a small water droplet inside the nematic drop stabilizes the radial configuration.

8. Temperature-induced flocculation above the nematic-isotropic phase transition

Ping Sheng [210,211] was the first to study the consequences of surface-induced liquid crystalline order above the nematic-isotropic phase transition. He introduced the notion *paranematic order* in analogy to the paramagnetic phase, in which a magnetic field causes a non-zero magnetization. He realized that the bounding surfaces of a restricted geometry influence the bulk transition temperature T_c. In nematic films, e.g., the phase transition even vanishes below a critical thickness [210]. Sheng's work was extended by Poniewierski and Sluckin [177], who studied two plates immersed in a liquid crystal above T_c and who calculated an attractive force

between the two plates due to the surface-induced order. This force was investigated in detail by Borštnik and Žumer [18].

The work presented in this section explores the liquid crystal mediated interaction between spherical particles immersed into a liquid crystal above T_c. It has to be added to the conventional van der Waals, electrostatic, and steric interactions as a new type of interparticle potential. Its strength can be controlled by temperature, and close to the clearing temperature T_c, it can induce a flocculation transition in an otherwise stabilized colloidal dispersion.

In Section 8.1 we review the Landau–de Gennes theory, which describes liquid crystalline order close to the phase transition, and we present Euler–Lagrange equations for the director and the Maier–Saupe order parameter to be defined below. Section 8.2 illustrates paranematic order in simple plate geometries and introduces the liquid crystal mediated interaction of two parallel plates. In Section 8.3 we extend it to spherical particles and investigate its consequences when combined with van der Waals and electrostatic interactions.

8.1. Theoretical background

We start with a review of the Landau–de Gennes theory and then formulate the Euler–Lagrange equations for restricted geometries with axial symmetry.

8.1.1. Landau–de Gennes theory in a nutshell

The director $\boldsymbol{n}$, a unit vector, only indicates the average direction of the molecules. It tells nothing about how well the molecules are aligned. To quantify the degree of liquid crystalline order, we could just vary the magnitude of $\boldsymbol{n}$, i.e., choose a polar vector as an order parameter. However, all nematic properties are invariant under inversion of the director, thus every polar quantity has to be zero. The next choice is any second-rank tensor, e.g., the magnetic susceptibility tensor $\boldsymbol{\chi}$. The order parameter $\boldsymbol{Q}$ is defined by the relation

$$\boldsymbol{Q} = \frac{9}{2\,\mathrm{tr}\,\boldsymbol{\chi}}\left(\boldsymbol{\chi} - \frac{1}{3}\mathbf{1}\,\mathrm{tr}\,\boldsymbol{\chi}\right) , \tag{8.1}$$

where $\mathrm{tr}\,\boldsymbol{\chi} = \chi_{ii}$ stands for the trace of a tensor, and Einstein's summation convention over repeated indices is always assumed in the following. We subtract the isotropic part $\mathbf{1}\,\mathrm{tr}\,\boldsymbol{\chi}/3$ from $\boldsymbol{\chi}$, in order that $\boldsymbol{Q}$ vanishes in the isotropic liquid. The prefactor is convention. The order parameter $\boldsymbol{Q}$ describes, in general, biaxial liquid crystalline ordering through its eigenvectors and eigenvalues. The uniaxial symmetry of the nematic phase demands that two eigenvalues of $\boldsymbol{Q}$ are equal, which then assumes the form

$$\boldsymbol{Q} = \frac{3}{2}S\left(\boldsymbol{n}\otimes\boldsymbol{n} - \frac{1}{3}\mathbf{1}\right) \quad \text{with } S = \frac{3(\chi_{\parallel} - \chi_{\perp})}{2\chi_{\perp} + \chi_{\parallel}} . \tag{8.2}$$

The Maier–Saupe or scalar order parameter S indicates the degree of nematic order through the magnetic anisotropy $\Delta\chi = \chi_{\parallel} - \chi_{\perp}$. It was first introduced by Maier and Saupe in a microscopic treatment of the nematic phase [142]. The microscopic approach was generalized by Lubensky to describe biaxial order [138].

In his seminal publication (see Ref. [48]) de Gennes was interested in pretransitional effects above the nematic-isotropic phase transition. He constructed a free energy in $\boldsymbol{Q}$ and $\nabla_i Q_{jk}$ in the spirit of Landau and Ginzburg, commonly known as Landau–de Gennes theory:

$$F_{\mathrm{LG}} = \int \mathrm{d}^3 r \, (f_{\mathrm{b}} + f_{\nabla Q}) \, , \tag{8.3}$$

with

$$f_{\mathrm{b}} = \tfrac{1}{2} a_0 (T - T^*) \operatorname{tr} \boldsymbol{Q}^2 - \tfrac{1}{3} b \operatorname{tr} \boldsymbol{Q}^3 + \tfrac{1}{4} c (\operatorname{tr} \boldsymbol{Q}^2)^2 \, , \tag{8.4}$$

$$f_{\nabla Q} = \tfrac{1}{2} L_1 (\nabla_i Q_{jk})^2 + \tfrac{1}{2} L_2 (\nabla_i Q_{ij})^2 \, . \tag{8.5}$$

The quantity f_{b} introduces a Landau-type free energy density which describes a first-order phase transition, and $f_{\nabla Q}$ is necessary to treat, e.g., fluctuations in $\boldsymbol{Q}$, as noticed by Ginzburg. Both free energy densities are Taylor expansions in $\boldsymbol{Q}$ and $\nabla_i Q_{jk}$, and each term is invariant under the symmetry group $O(3)$ of the isotropic liquid, i.e., the high-symmetry phase. The Landau parameters of the compound 5CB are $a_0 = 0.087 \times 10^7 \, \mathrm{erg/cm^3\,K}$, $b = 2.13 \times 10^7 \, \mathrm{erg/cm^3}$, $c = 1.73 \times 10^7 \, \mathrm{erg/cm^3}$, and $T^* = 307.15 \, \mathrm{K}$ [38]. The elastic constants L_1 and L_2 are typically of the order of 10^{-6} dyn.

It can be shown unambiguously that f_{b} is minimized by the uniaxial order parameter of Eq. (8.2), for which the free energies f_{b} and $f_{\nabla Q}$ take the form

$$f_{\mathrm{b}} = \frac{3}{4} a_0 (T - T^*) S^2 - \frac{1}{4} b S^3 + \frac{9}{16} c S^4 \, , \tag{8.6}$$

$$f_{\nabla Q} = \frac{3}{4} L_1 (\nabla_i S)^2 + \frac{9}{4} L_1 S^2 (\nabla_i n_j)^2 \, . \tag{8.7}$$

To arrive at Eq. (8.7), we set $L_2 = 0$ in order to simplify the free energy as much as possible for our treatment in Sections 8.2 and 8.3. $L_2 \neq 0$ merely introduces some anisotropy, as shown by de Gennes [48]. Assume, e.g., that S is fixed to a non-zero value at a space point $\boldsymbol{r}_s$ in the isotropic fluid, then the nematic order around $\boldsymbol{r}_s$ decays exponentially on a characteristic length scale called nematic coherence length. If $L_2 \neq 0$, the respective coherence lengths along and perpendicular to $\boldsymbol{n}$ are different. In Fig. 45 we plot f_{b} as a function of S using the parameters of 5CB. Above the *superheating* temperature $T^\dagger = T^* + b^2/(24 a_0 c)$, there exists only one minimum at $S = 0$ for the thermodynamically stable isotropic phase. At $T^\dagger$ a second minimum for the metastable nematic phase evolves, which becomes absolutely stable at the *clearing* temperature $T_{\mathrm{c}} = T^* + b^2/(27 a_0 c)$. A first-order phase transition occurs, and the order parameter as a function of temperature assumes the form

$$S(T) = \frac{1}{6} \frac{b}{c} + \sqrt{\frac{2a}{3c} (T^\dagger - T)} \, . \tag{8.8}$$

Finally, at the *supercooling* temperature T^* the curvature of f_{b} at $S = 0$ changes sign, and the isotropic fluid becomes absolutely unstable. For the compound 5CB, we find $T_{\mathrm{c}} - T^* = 1.12 \, \mathrm{K}$ and $T^\dagger - T_{\mathrm{c}} = 0.14 \, \mathrm{K}$.

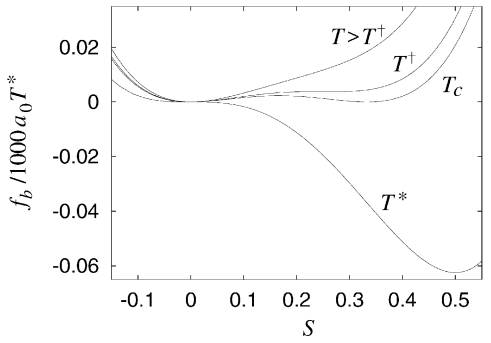

Fig. 45. The free energy density f_b in units of $1000a_0T^*$ as a function of the Maier–Saupe order parameter S for various temperatures. The Landau coefficients of the compound 5CB are employed. A first-order transition occurs at T_c.

8.1.2. Euler–Lagrange equations for restricted geometries

In the following, we determine the surface-induced liquid crystalline order above T_c. As usual, it follows from a minimization of the total free energy,

$$F = F_{LG} + F_{sur} , \tag{8.9}$$

where we have added a surface term F_{sur} to the Landau–de Gennes free energy F_{LG}. We restrict ourselves to uniaxial order and employ a generalization of the Rapini–Papoular potential, introduced in Section 2.1,

$$F_{sur} = \int dA \, \frac{3}{4}(W_S(S - S_0)^2 + 3W_{\boldsymbol{n}}SS_0[1 - (\boldsymbol{n}\cdot\hat{\boldsymbol{\nu}})^2]) , \tag{8.10}$$

where dA is the surface element. The quantity S_0 denotes the preferred Maier–Saupe parameter at the surface, and $\hat{\boldsymbol{\nu}}$ is the surface normal since we always assume homeotropic anchoring. The surface-coupling constants W_S and $W_{\boldsymbol{n}}$ penalize a respective deviation of S from S_0 and of the director $\boldsymbol{n}$ from $\hat{\boldsymbol{\nu}}$. In recent experiments, anchoring and orientational wetting transitions of liquid crystals, confined to cylindrical pores of alumina membranes, were analyzed [42,43]. It was found that W_S and $W_{\boldsymbol{n}}$ vary between 10^{-1} and 5, with the ratio $W_{\boldsymbol{n}}/W_S$ not being larger than five. If $W_S = W_{\boldsymbol{n}} = W$, the intergrand in Eq. (8.10) is equivalent to the intuitive form $W\,\mathrm{tr}(\boldsymbol{Q} - \boldsymbol{Q}_0)^2/2$ with the uniaxial $\boldsymbol{Q}$ from Eq. (8.2) and $\boldsymbol{Q}_0 = \frac{3}{2}S_0(\hat{\boldsymbol{\nu}} \otimes \hat{\boldsymbol{\nu}} - \frac{1}{3}\mathbf{1})$. It was introduced by Nobili and Durand [165]. In formulating the elastic free energy density $f_{\nabla Q}$ of Eq. (8.5), one also identifies a contribution which can be written as a total divergence, $\nabla_i(Q_{ij}\nabla_k Q_{jk} - Q_{jk}\nabla_k Q_{ij})$. When transformed into a surface term and when a uniaxial $\boldsymbol{Q}$ is inserted, it results in the saddle-splay energy of Eq. (2.4). To simplify our calculations, we will neglect this term. It is not expected to change the qualitative behavior of our system for strong surface coupling.

In what follows, we assume rotational symmetry about the z axis. We introduce cylindrical coordinates and write the director in the local coordinate basis, $\boldsymbol{n}(\rho,z) = \sin\Theta(\rho,z)\boldsymbol{e}_\rho + \cos\Theta(\rho,z)\boldsymbol{e}_z$, restricting it to the (ρ,z) plane. The same is assumed for the surface normal $\hat{\boldsymbol{\nu}}(\rho,z) = \sin\Theta_0(\rho,z)\boldsymbol{e}_\rho + \cos\Theta_0(\rho,z)\boldsymbol{e}_z$. Expressing and minimizing the total free energy under

all these premises, we obtain the Euler–Lagrange equations for S and the tilt angle Θ in the bulk,

$$\nabla^2 S - \frac{1}{\xi_N^2} S + \frac{b}{2L_1} S^2 - \frac{3c}{2L_1} S^3 - 3S \left((\nabla \Theta)^2 + \frac{\sin^2 \Theta}{\rho^2} \right) = 0 \,, \tag{8.11}$$

$$\nabla^2 \Theta - \frac{\sin \Theta \cos \Theta}{\rho^2} = 0 \,, \tag{8.12}$$

and the boundary equations are

$$(\hat{\boldsymbol{v}} \cdot \nabla) S - \frac{1}{\gamma_S \xi_N} (S - S_0) - \frac{3}{2\gamma_{\boldsymbol{n}} \xi_N} S_0 \sin^2(\Theta - \Theta_0) = 0 \,, \tag{8.13}$$

$$(\hat{\boldsymbol{v}} \cdot \nabla) \Theta - \frac{1}{2\gamma_{\boldsymbol{n}} \xi_N} \frac{S_0}{S} \sin[2(\Theta - \Theta_0)] = 0 \,. \tag{8.14}$$

The meaning of the nematic coherence length

$$\xi_N = \sqrt{L_1 / [a_0 (T - T^*)]} \tag{8.15}$$

will be clarified in the next subsection. At the phase transition, $\xi_{NI} = \xi_N(T_c)$ is of the order of 10 nm, as can be checked by the parameters of 5CB. The surface-coupling strengths W_S and $W_{\boldsymbol{n}}$ are characterized by dimensionless quantities

$$\gamma_S = \frac{1}{\xi_N} \frac{L_1}{W_S} = \frac{\sqrt{a_0 (T - T^*) L_1}}{W_S} \quad \text{and} \quad \gamma_{\boldsymbol{n}} = \frac{1}{\xi_N} \frac{L_1}{W_{\boldsymbol{n}}} = \frac{\sqrt{a_0 (T - T^*) L_1}}{W_{\boldsymbol{n}}} \,, \tag{8.16}$$

which compare the respective surface extrapolation lengths L_1/W_S and $L_1/W_{\boldsymbol{n}}$ to the nematic coherence length ξ_N. For $W = 1\,\mathrm{erg/cm^2}$ and $L_1 = 10^{-6}\,\mathrm{dyn}$, the extrapolation lengths are of the same order as ξ_N at T_c, i.e., 10 nm.

8.2. Paranematic order in simple geometries

In the first two subsections we study the paranematic order in a liquid crystal compound above T_c for simple plate geometries. It is induced by a coupling between the surfaces and the molecules. We disregard the non-harmonic terms in S in Eq. (8.11) to simplify the problem as much as possible and to obtain an overall view of the system. In Section 8.2.3 the effect of the non-harmonic terms is reviewed.

8.2.1. One plate

We assume that an infinitely extended plate, which induces a homeotropic anchoring of the director, is placed at $z = 0$. Its surface normals are $\pm \boldsymbol{e}_z$, and its thickness should be negligibly small. A uniform director field along the z axis obeys Eqs. (8.12) and (8.14), and the Maier–Saupe order parameter S follows from a solution of Eqs. (8.11) and (8.13),

$$S(z) = \frac{S_0}{1 + \gamma_S} \exp[-|z|/\xi_N] \,. \tag{8.17}$$

The order parameter S decays exponentially along the z axis on a characteristic length scale given by the nematic coherence length ξ_N. The value of S at $z = 0$ depends on the strength γ_S

of the surface coupling, i.e., on the ratio of the surface extrapolation length L_1/W and ξ_N. The plate is surrounded by a layer of liquid crystalline order whose thickness ξ_N decreases with increasing temperature since $\xi_N \propto (T - T^*)^{-1/2}$. The total free energy per unit surface, F/A, consisting of the Landau–de Gennes and the surface free energy, is

$$\frac{F}{A} = \frac{3}{2} W_S S_0^2 \frac{\gamma_S}{1+\gamma_S} \,. \tag{8.18}$$

Note that the energy increases with temperature since $\gamma_S \propto \sqrt{T - T^*}$. The whole theory certainly becomes invalid when ξ_N approaches molecular dimensions. For 10 K above T_c, we find $\xi_N \approx 3$ nm, i.e., the theory is valid several Kelvin above T_c. Finally, we notice that a nematic wetting layer can be probed by the evanescent wave technique [214].

8.2.2. Two plates

If two plates of the previous subsection are placed at $z = \pm d/2$, the order parameter profile $S(z)$, determined from Eqs. (8.11) and (8.13), is

$$S(z) = S_0 \frac{\cosh(z/\xi_N)}{\cosh(d/2\xi_N) + \gamma_S \sinh(d/2\xi_N)} \,. \tag{8.19}$$

For separations $d \gg 2\xi_N$, the layers of liquid crystalline order around the plates do not overlap, as illustrated in the inset of Fig. 46.[6] If $d \leqslant 2\xi_N$, the whole volume between the plates is occupied by nematic order, which induces an attraction between the plates. The interaction energy per unit area, $\Delta F/A$, is defined as $\Delta F/A = [F(d) - F(d \to \infty)]/A$. It amounts to

$$\frac{\Delta F}{A} = \frac{F(d) - F(d \to \infty)}{A} = \frac{3}{2} W_S S_0^2 \gamma_S \left[\frac{\tanh(d/2\xi_N)}{1 + \gamma_S \tanh(d/\xi_N)} - \frac{1}{1+\gamma_S} \right] \,. \tag{8.20}$$

In Fig. 46 we plot $\Delta F/A$ versus the reduced distance $d/2\xi_{NI}$ for different temperatures at T_c and above T_c. The material parameters of 5CB are chosen; $W_S = 1\,\mathrm{erg/cm^2}$, and $S_0 = 0.3$. The energy unit $3W_S S_0^2/2 = 10^4 k_B T$ is determined at room temperature. Note, that ξ_{NI} is the coherence length at T_c. If $d \gg \xi_N$, the interaction energy decays exponentially in d, $\Delta F/A \propto \exp(d/\xi_N)$. The interaction is always attractive over the whole separation range. This can be understood by a simple argument. Above T_c, the nematic order always possesses higher energy than the isotropic liquid. Therefore, the system can reduce its free energy by moving the plates together. The minimum of the interaction energy occurs at $d = 0$, i.e., when the liquid with nematic order between the plates is completely removed. This simple argument explains the deep potential well in Fig. 46. It extends to a separation of $2\xi_N$ where the nematic layers start to overlap. Since $\xi_N \propto (T - T^*)^{-1/2}$, the range of the interaction decreases with increasing temperature, and the depth of the potential well becomes smaller.

8.2.3. Effect of non-harmonic terms

In this subsection we review the effects on the two-plate geometry when the complete Landau–de Gennes theory including its non-harmonic terms in S is employed. A wealth of

[6] Figs. 46, 47, 51 and 52 are reprinted with permission from A. Borštnik, H. Stark, S. Žumer, Temperature-induced flocculation of colloidal particles above the nematic-isotropic phase transition, Prog. Colloid Polym. Sci. 115 (2000) 353. Copyright 2000 Springer Verlag.

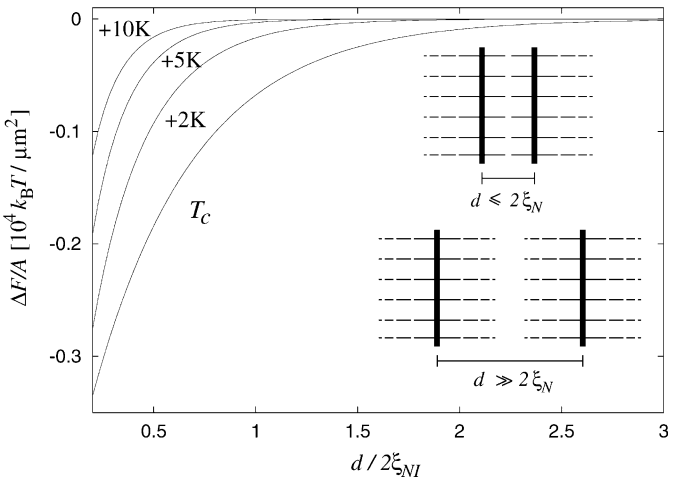

Fig. 46. Interaction energy per unit area, $\Delta F/A$, as a function of the reduced distance $d/2\xi_{\mathrm{NI}}$ for various temperatures. For further explanation see text.

phenomena exists, which we illustrate step by step [210,211]. Their influence on the interaction of two plates was studied in detail by Borštnik and Žumer [18].

First, we assume rigid anchoring at the nematic-plate interfaces, i.e., $S(\pm d/2)$ is fixed to S_0 [210]. For $d \to \infty$, there is a phase transition at the bulk transition temperature $T_{c\infty} = T_c$ from the nematic to the surface-induced paranematic phase, as expected. When the plates are moved together, the transition temperature T_{cd} increases until the first-order transition line in a d–T phase diagram ends in a critical point at $(d_{\mathrm{crit}}, T_{cd}^{\mathrm{crit}})$. For $d < d_{\mathrm{crit}}$, no phase transition between the nematic and the paranematic phase is observed anymore. This is similar to the gas–liquid critical point in an isotropic fluid. For $S_0 = S(\pm d/2) = 0.5 - 1$ and typical values of the Landau parameters, T_{cd}^{crit} is situated approximately 0.2 K above $T_{c\infty} = T_c$ and 0.1 K above the superheating temperature $T^{\dagger}$.

Secondly, we concentrate on a basically infinite separation, $d \gg \xi_{\mathrm{NI}}$, and allow a finite surface-coupling strength W_S [211]. For sufficiently small W_S, both the boundary $[S(\pm d/2)]$ and the bulk $[S(0)]$ value of the scalar order parameter exhibit a jump at T_c. That means, the surface coupling is so small that $S(\pm d/2)$ follows the bulk order parameter. However, in a finite interval $W_{S0} < W_S < W_S^{\mathrm{crit}}$, the discontinuity of $S(\pm d/2)$, which Sheng calls a boundary-layer phase transition, occurs at temperatures T_{bound} above T_c. Beyond the critical strength W_S^{crit}, the boundary transition vanishes completely. Sheng just used the linear term $\propto W_S S$ of our surface potential for his investigation. The separate boundary-layer transition occurred in the approximate interval $0.01\,\mathrm{erg/cm^2} < W_S < 0.2\,\mathrm{erg/cm^2}$. We do not expect a dramatic change of this interval for the potential of Eq. (8.10).

Thirdly, we combine the finite separation of the plates with a finite surface-coupling strength W_S. The boundary-layer transition temperatures T_{bound} and the interval $W_{S0} < W_S < W_S^{\mathrm{crit}}$ are not effected by a finite d. In addition, a jump of $S(\pm d)$ occurs at the bulk transition temperature $T_{cd} \leqslant T_{\mathrm{bound}}$. It evolves gradually with decreasing d. When T_{cd} becomes larger than T_{bound}

in the course of moving the plates together, the separate boundary-layer transition disappears. Finally, at a critical thickness d_{crit} the nematic-paranematic transition vanishes altogether.

All these details occur close to $T_{c\infty} = T_c$ within a range of $T_{cd}^{\mathrm{crit}} - T_{c\infty} = 0.5\,\mathrm{K}$ [211]. The calculations are non-trivial. Since we do not want to render our investigation in the following subsection too complicated, we will skip the non-harmonic terms in the Landau–de Gennes theory. Furthermore, we use a relatively high anchoring strength of about $W_S = 1\,\mathrm{erg/cm^2}$, so that $T_{cd}^{\mathrm{crit}} - T_{c\infty}$ is even smaller than 0.5 K. The simplifications are sufficient to bring out the main features of our system.

8.3. Two-particle interactions above the nematic-isotropic phase transition

In this subsection we present the liquid crystal mediated interaction above T_c as a new type of two-particle potential. We combine it with the traditional van der Waals and electrostatic interaction and explore its consequences, namely the possibility of a temperature-induced flocculation. We start with a motivation, introduce all three types of interactions, and finally discuss their consequences. Our presentation concentrates on the main ideas and results (see also Ref. [17]). Details of the calculations can be found in Refs. [15,16].

8.3.1. Motivation

In Section 3 we already mentioned that the stability of colloidal systems presents a key issue in colloid science since their characteristics change markedly in the transition from the dispersed to the aggregated state. There are always attractive van der Waals forces, which have to be balanced by repulsive interactions to prevent a dispersion of particles from aggregating. This is achieved either by electrostatic repulsion, where the particles carry a surface charge, or by steric stabilization, where they are coated with a soluble polymer brush. Dispersed particles approach each other due to their Brownian motion. They aggregate if the interaction potential is attractive, i.e., if it possesses a potential minimum $U_{\mathrm{min}} < 0$ at finite separations. Two situations are possible. In the case of weak attraction, where $|U_{\mathrm{min}}| \approx 1\text{–}3k_{\mathrm{B}}T$, an equilibrium phase separation of a dilute and an aggregated state exists. The higher interaction energy of the dispersed particles is compensated by their larger entropy in comparison to the aggregated phase. Strong attraction, i.e., $|U_{\mathrm{min}}| > 5 - 10k_{\mathrm{B}}T$, causes a non-equilibrium phase with all the particles aggregated. They cannot escape the attractive potential in the observation time of interest of, e.g., several hours. Due to Chandrasekhar, the escape time t_{esc} can be estimated as [28]

$$t_{\mathrm{esc}} = \frac{a^2}{D_0 \exp(-U_{\mathrm{min}}/k_{\mathrm{B}}T)} \quad \text{with } D_0 = \frac{k_{\mathrm{B}}T}{6\pi\eta a}\,. \tag{8.21}$$

D_0 is the diffusion constant of a non-interacting Brownian particle with radius a, and η is the shear viscosity of the solvent. The quantity t_{esc} approximates the time a particle needs to diffuse a distance a in leaving a potential well of depth U_{min}. More refined theories suggest that the complete two-particle potential has to be taken into account when calculating t_{esc} [131,100].

Here, we study the influence of liquid crystal mediated interactions on colloidal dispersions above T_c, which are stabilized by an electrostatic repulsion. We demonstrate that the main effect of the liquid crystal interaction U_{LC} is an attraction at the length scale of ξ_{N}, whose strength can be controlled by temperature. If the electrostatic repulsion is sufficiently weak, U_{LC} induces

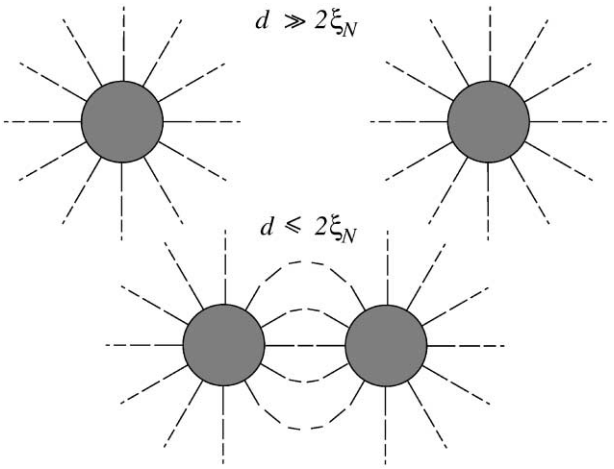

Fig. 47. Two particles at a separation $d \gg 2\xi_N$ do not interact. At $d \approx 2\xi_N$ both a strong attraction and repulsion set in.

a flocculation of the particles within a few Kelvin close to the transition temperature T_c. It is completely reversible. A similar situation is found in polymer stabilized colloids. There, the abrupt change from a dispersed to a fully aggregated state within a few Kelvin is called *critical flocculation* [162,202]. The reversibility of flocculation has interesting technological implications. For example, in "instant" ink, the particles of dried ink redisperse rapidly when put into water [162].

So far, experiments on colloidal dispersions above the clearing temperature T_c are very rare [19,178]. They would help to explore a new class of colloidal interactions. Furthermore, they could provide insight into wetting phenomena above T_c with all its subtleties close to T_c, which we reviewed in Section 8.2.3. Also, experiments by Muševič et al. [158,159], who probe interactions with the help of an atomic force microscope, are promising.

8.3.2. Liquid crystal mediated interaction

One particle suspended in a liquid crystal above the clearing temperature T_c is surrounded by a layer of surface-induced nematic order whose thickness is of the order of the nematic coherence length ξ_N. The director field points radially outward when a homeotropic anchoring at the particle surface is assumed. Two particles with a separation $d \gg 2\xi_N$ do not interact. When the separation is reduced to $d \approx 2\xi_N$, a strong attraction sets in since the total volume of nematic order is decreased as in the case of two plates (see Fig. 47). In addition, a repulsion due to the elastic distortion of the director field lines connecting the two particles occur. In this subsection we quantify the two-particle interaction mediated by a liquid crystal.

In principle, the director field and the Maier–Saupe order parameter S follow from a solution of Eqs. (8.11)–(8.14). Since the geometry of Fig. 48a cannot be treated analytically, we employ two simplifications. First, we approximate each sphere by 72 conical segments, whose cross sections in a symmetry plane of our geometry are illustrated in Fig. 48a. In the following, we assume a particle radius $a = 250\,\text{nm}$, and, therefore, each line segment has a length of

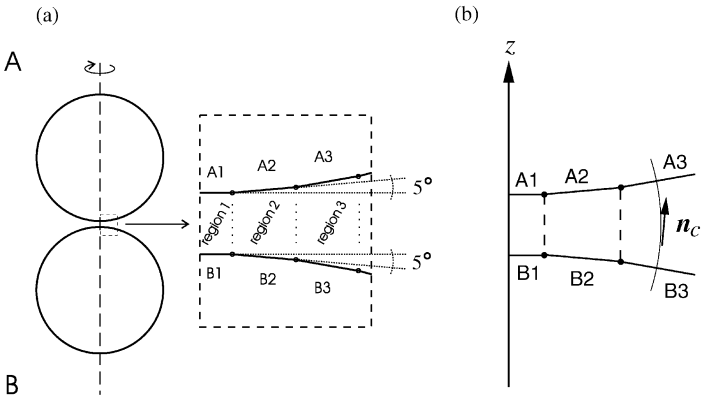

Fig. 48. (a) Two spheres A and B are approximated by conical segments as illustrated in the blowup. From Ref. [15]. (b) At separations $d \approx 2\xi_N$, the director is chosen as a tangent vector $\boldsymbol{n}_c$ of a circular segment whose radius is determined by the boundary condition (8.14).

26 nm. Secondly, we construct appropriate ansatz functions for the fields $S(\boldsymbol{r})$ and $\boldsymbol{n}(\boldsymbol{r})$. To arrive at an ansatz for $S(\boldsymbol{r})$, we approximate the bounding surfaces Ai and Bi of region i by two parallel ring-like plates and employ the order parameter profile of Eq. (8.19), where d is replaced by an average distance d_i of the bounding surfaces. Since the particle radius is an order of magnitude larger than the interesting separations, which do not exceed several coherence lengths, the analogy with two parallel plates is justified. Furthermore, we expect that only a few regions close to the symmetry axis are needed to calculate the interaction energy with a sufficient accuracy. In the limit of large separations ($d \gg 2\xi_N$), the director field around each sphere points radially outward. In the opposite limit ($d \approx 2\xi_N$), the director field lines are strongly distorted, and we approximate them by circular segments as illustrated in Fig. 48b, for the third region. The radius of the circle is determined by the boundary condition (8.14) of the director. With decreasing separation of the two particles, the director field should change continuously from $\boldsymbol{n}_\infty$ at $d \gg 2\xi_N$ to the ansatz $\boldsymbol{n}_c$ at small d. Hence, we choose $\boldsymbol{n}(\boldsymbol{r})$ as a weighted superposition of $\boldsymbol{n}_c$ and $\boldsymbol{n}_\infty$:

$$\boldsymbol{n}(\boldsymbol{r}) \propto \varepsilon_i \boldsymbol{n}_c + (1 - \varepsilon_i)\boldsymbol{n}_\infty \,, \tag{8.22}$$

where the free parameter ε_i follows from a minimization of the free energy in region i with respect to ε_i.

As in the case of two parallel plates, the interaction energy is defined relative to the total free energy of infinite separation:

$$U_{LC}(d) = F(d) - F(d \to \infty) \,. \tag{8.23}$$

In calculating U_{LC}, we employ the free energy densities of Eqs. (8.6) and (8.7) and the surface potential of Eq. (8.10), neglecting the non-harmonic terms in S. The volume integrals cannot be performed analytically without further approximations which we justified by a comparison with a numerical integration. The final expression of U_{LC} is very complicated, and we refer the reader to Ref. [15] for its explicit form. We checked that regions $i = 1, \ldots, 9$ are sufficient to

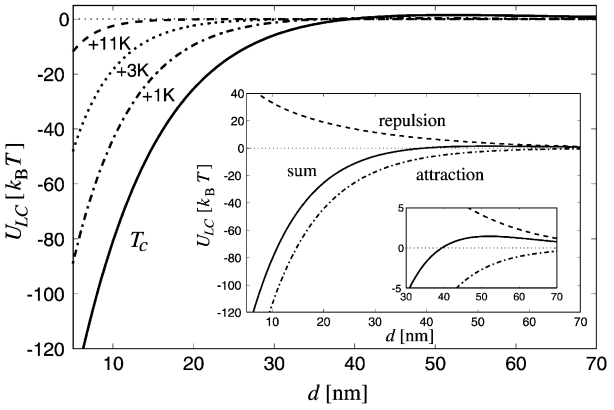

Fig. 49. The liquid crystal mediated interaction U_{LC} in units of $k_{\mathrm{B}}T$ as a function of the particle separation d. The interaction is shown at $T_{\mathrm{c}}, T_{\mathrm{c}}+1\,\mathrm{K}, T_{\mathrm{c}}+3\,\mathrm{K}$, and $T_{\mathrm{c}}+11\,\mathrm{K}$. It strongly depends on temperature. Large inset: U_{LC} is composed of an attractive and repulsive part. Small inset: A weak repulsive barrier occurs at $d\approx 60\,\mathrm{nm}$.

calculate U_{LC}. The contribution of region 9 to the interaction energy is less than 5%. Hence, the orientational order outside these nine regions is not relevant for U_{LC}.

We subdivide the interaction energy in an attractive part which results from all terms in the free energy depending on the order parameter S or its gradient, only. The repulsive part is due to the elastic distortion of the director field and a deviation from the homeotropic orientation at the particle surfaces. All the graphs, which we present in the following, are calculated with the Landau parameters of the compound 8CB [38], i.e., $a_0 = 0.12\times 10^{-7}\,\mathrm{erg/cm^3\,K}$, $b = 3.07\times 10^{-7}\,\mathrm{erg/cm^3}$, $c = 2.31\times 10^{-7}\,\mathrm{erg/cm^3}$, and $L_1 = 1.8\times 10^{-6}\,\mathrm{dyn}$, which gives $T_{\mathrm{c}} - T^* = b^2/(27a_0c) = 1.3\,\mathrm{K}$. The surface-coupling constants are $W_S = 1\,\mathrm{erg/cm^2}$ and $W_{\boldsymbol{n}} = 5\,\mathrm{erg/cm^2}$. In the large inset of Fig. 49 we plot the attractive and repulsive contribution at the clearing temperature T_{c} in units of the thermal energy $k_{\mathrm{B}}T$. As in the case of two parallel plates, the total interaction energy exhibits a deep potential well with an approximate width of $2\xi_{\mathrm{NI}}$. At larger separations, it is followed by a weak repulsive barrier whose height is approximately $1.5k_{\mathrm{B}}T$, as indicated by the small inset in Fig. 49. If $d \gg 2\xi_{\mathrm{N}}$, U_{LC} decays exponentially: $U_{\mathrm{LC}} \propto \exp(-d/\xi_{\mathrm{N}})$. Fig. 49 illustrates further that the depth of the potential well, i.e., the liquid crystal mediated attraction of two particles decreases considerably when the dispersion is heated by several Kelvin. That means, the interaction can be controlled by temperature. It is turned off by heating the dispersion well above T_{c}. The same holds for the weak repulsive barrier. As expected, both the depth of the potential well and the height of the barrier decrease with the surface-coupling constants, where W_S seems to be more important [15].

8.3.3. Van der Waals and electrostatic interactions

The van der Waals interaction of two thermally fluctuating electric dipoles decays with the sixth power of their inverse distance, $1/r^6$. To arrive at the interparticle potential of two macroscopic objects, a summation over all pair-wise interactions of fluctuating charge distributions is performed. In the case of two spherical particles of equal radii a, the following,

always attractive, van der Waals interaction results [202]:

$$U_{\mathrm{W}} = -\frac{A}{6}\left[\frac{2a^2}{d(d+4a)} + \frac{2a^2}{(d+2a)^2} + \ln\frac{d(d+4a)}{(d+2a)^2}\right] . \tag{8.24}$$

Here d is the distance between the surfaces of the particles, and A is the Hamaker constant. For equal particles made of material 1 embedded in a medium 2, it amounts to [202]

$$A = \frac{3}{4}k_{\mathrm{B}}T\left(\frac{\varepsilon_1-\varepsilon_2}{\varepsilon_1+\varepsilon_2}\right)^2 + \frac{3h\nu_{\mathrm{uv}}}{16\sqrt{2}}\frac{(n_1^2-n_2^2)^2}{(n_1^2+n_3^2)^{3/2}} , \tag{8.25}$$

where ε_1 and ε_2 are the static dielectric constants of the two materials, and n_1 and n_2 are the corresponding refractive indices of visible light. The relaxation frequency ν_{uv} belongs to the dominant ultraviolet absorption in the dielectric spectrum of the embedding medium 2. Typical values for silica particles immersed into a nematic liquid crystal are $\varepsilon_1 = 3.8$, $n_1 = 1.45$, $\varepsilon_2 = 11$, $n_2 = 1.57$, and $\nu_{\mathrm{uv}} = 3\times10^{15}\,\mathrm{s}^{-1}$ [15]. As a result, the Hamaker constant equals $A = 1.1\,k_{\mathrm{B}}T$. Note, that for separations $d \gg a$ the particles are point-like, and the van der Waals interaction decays as $1/d^6$. In the opposite limit, $d \ll a$, it diverges as a/d.

We stabilize the colloidal dispersion against the attractive van der Waals forces by employing an electrostatic repulsion. We assume that each particle carries a uniformly distributed surface charge whose density q_s does not change under the influence of other particles. Ionic impurities in the liquid crystal screen the surface charges with which they form the so-called electrostatic double layer. For particles of equal radius a embedded in a medium with dielectric constant ε_2, the electrostatic two-particle potential is described by the following expression [202]:

$$U_{\mathrm{E}} = -\pi k_{\mathrm{B}}T\frac{aq_s^2}{z^2e_0^2n_p}\ln(1-e^{-\kappa d}) . \tag{8.26}$$

Here, e_0 is the fundamental charge, and z is the valence of the ions in the solvent, which have a concentration n_p. The range of the repulsive interaction is determined by the *Debye length*

$$\kappa^{-1} = \sqrt{\varepsilon_2 k_{\mathrm{B}}T/(8\pi e_0^2 z^2 n_p)} , \tag{8.27}$$

whereas the surface-charge density q_s controls its strength. The potential U_{E} decays exponentially at $d \gg \kappa^{-1}$. Expression (8.26) is derived via the *Derjaguin approximation* [53,202], which is only valid for $d, \kappa^{-1} \ll a$. In the following, we take a monovalent salt ($z = 1$), choose $\varepsilon_2 = 11$, and vary n_p between 10^{-4} and 10^{-3} mol/l. Then, at room temperature the Debye length κ^{-1} ranges from 10 to 3.5 nm. Together with typical separations d not larger than a few coherence lengths ξ_{N} and $a = 250\,\mathrm{nm}$, the Derjaguin approximation is justified. Furthermore, we adjust the surface-charge density around $10^4 e_0/\mu\mathrm{m}^2$. The ranges of n_p and q_s are well accessible in an experiment.

In Fig. 50 we plot the electrostatic and the van der Waals interactions and their sum in units of $k_{\mathrm{B}}T$. The surface-charge density q_s is $0.5\times10^4 e_0/\mu\mathrm{m}^2$ and $\kappa^{-1} = 8.3\,\mathrm{nm}$. All further parameters besides the Hamaker constant A are chosen as mentioned above. We increased A from 1.1 to 5.5. Even then it is clearly visible that the strong electrostatic repulsion determines the interaction for $d < 30\,\mathrm{nm}$, the dispersion of particles is stabilized. At about 55 nm, $U_{\mathrm{E}} + U_{\mathrm{W}}$ exhibits a shallow potential minimum (see inset of Fig. 50), and at $d \gg \kappa^{-1}$, the algebraic decay

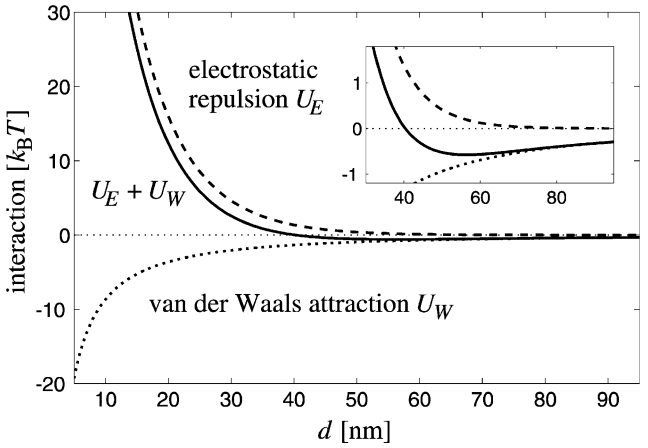

Fig. 50. The electrostatic (dashed) and van der Waals (dotted) interaction and their sum $U_E + U_W$ (full line) in units of k_BT as a function of particle separation d. The parameters are chosen according to the text. Inset: A shallow potential minimum appears at $d \approx 55$ nm.

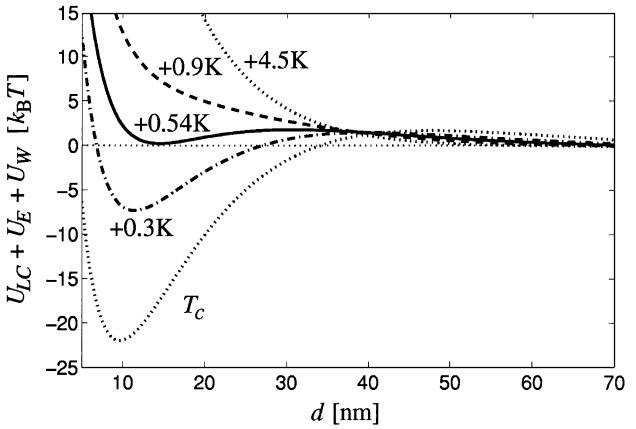

Fig. 51. The total two-particle interaction $U_{LC} + U_E + U_W$ as a function of particle separation d for various temperatures. A complete flocculation of the particles occurs within a temperature range of about 0.3 K. $q_s = 0.5 \times 10^4 e_0/\mu m^2$, $\kappa^{-1} = 8.3$ nm, and further parameters are chosen according to the text.

of the van der Waals interaction takes over. In the following subsection, we investigate the combined effects of all three interactions for the Hamaker constant $A = 1.1$.

8.3.4. Flocculation versus dispersion of particles

In Fig. 51 we plot the total two-particle interaction $U_{LC} + U_E + U_W$ as a function of particle separation d for various temperatures. We choose $q_s = 0.5 \times 10^4 e_0/\mu m^2$ and $\kappa^{-1} = 8.3$ nm. At 4.5 K above the transition temperature T_c, the dispersion is stable. With decreasing temperature, a potential minimum at finite separation develops. At $T_{FD} = T_c + 0.54$ K, the particle doublet or aggregated state becomes energetically preferred. We call T_{FD} the temperature of *flocculation*

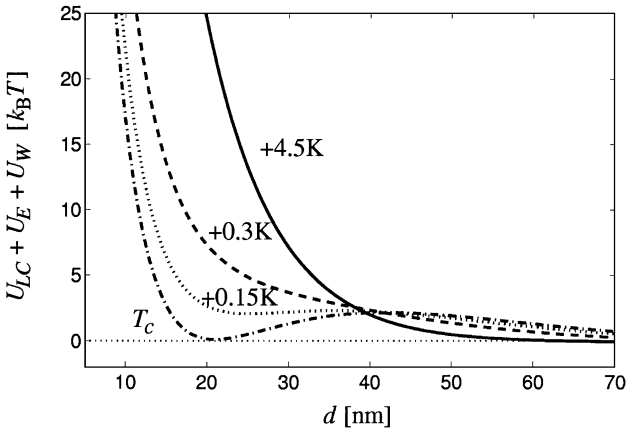

Fig. 52. In comparison to Fig. 51 the surface-charge density is increased to $0.63\times10^4 e_0/\mu m^2$. As a result, flocculation does not occur.

transition. Below T_{FD}, the probability of finding the particles in the aggregated state is larger than the probability that they are dispersed. Already at $T_c + 0.3\,K$ the minimum is $7\,k_BT$ deep, and all particles are condensed in aggregates. That means, within a temperature range of about 0.3 K there is an abrupt change from a completely dispersed to a fully aggregated system, reminiscent to the critical flocculation transition in colloidal dispersions employing polymeric stabilization [162,202]. Between $d = 30$ and 50 nm, the two-particle interaction exhibits a small repulsive barrier of about $1.5\,k_BT$. Such barriers slow down the aggregation of particles, and one distinguishes between *slow* and *rapid flocculation*. The dynamics of rapid flocculation was first studied by Smoluchowski [215]. Fuchs extended the theory to include arbitrary interaction potentials [82]. However, only after Derjaguin and Landau [54] and Verwey and Overbeek [229] incorporated van der Waals and electrostatic interactions into the theory, became a comparison with experiments possible. In our case, the repulsive barrier of $1.5\,k_BT$ slows down the doublet formation by a factor of three, i.e., it does not change very dramatically if the barrier is reduced to zero.

If the surface-charge density q_s is increased to $0.63 \times 10^4 e_0/\mu m^2$, the dispersed state is thermodynamically stable at all temperatures above T_c, as illustrated in Fig. 52. An increase of the Debye length κ^{-1}, i.e., the range of the electrostatic repulsion, has the same effect.

In Fig. 53 we present flocculation phase diagrams as a function of temperature and surface-charge density for various Debye lengths κ^{-1}. The inset shows one such diagram for $\kappa^{-1} = 8.3$ nm. The full line represents the flocculation temperature T_{FD} as a function of q_s. For temperatures above T_{FD}, the particles stay dispersed while for temperatures below T_{FD} the system is flocculated. To characterize the aggregated state further, we have determined lines in the phase diagram of $\kappa^{-1} = 8.3$ nm, where the escape time t_{esc} of Eq. (8.21) is, respectively, ten (dash-dotted) or hundred (dotted) times larger than in the case of zero interaction. These lines are close to the transition temperature T_{FD}, and indicate again that the transition from the dispersed to a completely aggregated state takes place within less than one Kelvin. The large plot of Fig. 53 illustrates the flocculation temperature T_{FD} as a function of q_s for various Debye

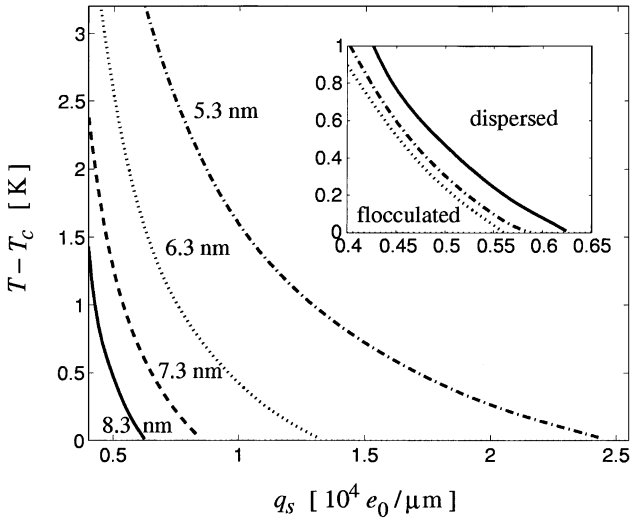

Fig. 53. Flocculation phase diagrams as a function of temperature and surface-charge density for various Debye lengths κ^{-1}. Inset: Phase diagram for $\kappa^{-1} = 8.3\,\text{nm}$. The full line represents the flocculation temperature T_{FD} as a function of q_s. The dash-dotted and dotted lines indicate escape times from the minimum of the interparticle potential which are, respectively, ten or hundred times larger than in the case of zero interaction. From Ref. [16].

lengths κ^{-1}. T_{FD} increases when the strength (q_s) or the range (κ^{-1}) of the electrostatic repulsion is reduced. The intersections of the transition lines with the $T = T_c$ axis define the "flocculation end line". In the parameter space of the electrostatic interaction (surface charge density q_s versus Debye length κ^{-1}), this line separates the region where we expect the flocculation to occur from the region where the system is dispersed for all temperatures above T_c (see Ref. [16]).

8.3.5. Conclusions

Particles dispersed in a liquid crystal above the nematic-isotropic phase transition are surrounded by a surface-induced nematic layer whose thickness is of the order of the nematic coherence length. The particles experience a strong liquid crystal mediated attraction when their nematic layers start to overlap since then the effective volume of liquid crystalline ordering and therefore the free energy is reduced. A repulsive correction results from the distortion of the director field lines connecting two particles. The new colloidal interaction is easily controlled by temperature. In this section we have presented how it can be probed with the help of electrostatically stabilized dispersions.

For sufficiently weak and short-ranged electrostatic repulsion, we observe a sudden flocculation within a few tenth of a Kelvin close to T_c. It is reminiscent to the critical flocculation transition in polymer stabilized colloidal dispersions [202]. The flocculation is due to a deep potential minimum in the total two-particle interaction followed by a weak repulsive barrier. Thermotropic liquid crystals represent polar organic solvents, and one could wonder if electrostatic repulsion is realizable in such systems. In Ref. [101] complex salt is dissolved in nematic liquid crystals and ionic concentrations of up to 10^{-4} mol/l are reported which give

rise to Debye lengths employed in this section. Furthermore, when silica spheres are coated with silanamine, the ionogenic group [$=NH_2^+OH^-$] occurs at the particle surface with a density of 3×10^6 mol/μm^2. It dissociates to a large amount in a liquid crystal compound [59]. In addition, the silan coating provides the required perpendicular boundary condition for the liquid crystal molecules. These two examples illustrate that electrostatic repulsion should be accessible in conventional thermotropic liquid crystals, and we hope to initiate experimental studies which probe the new colloidal force. Our work directly applies to lyotropic liquid crystals [51], i.e., aqueous solutions of non-spherical micelles, when the nematic-isotropic phase transition is controlled by temperature [181,180]. They are appealing systems since electrostatic stabilization is more easily achieved. When the phase transition is controlled by the micelle concentration ρ_m, as it is usually done, then our diagrams are still valid but with temperature replaced by ρ_m.

In polymer stabilized dispersions, we find that the aggregation of particles sets in gradually when cooling the dispersion down towards T_c. This is in contrast to electrostatic stabilization where flocculation occurs in a very narrow temperature interval (see Ref. [16]).

9. Final remarks

In this article we have demonstrated that the combination of two soft materials, nematic liquid crystals and colloidal dispersions, creates a novel challenging system for discovering and studying new physical effects and ideas.

Colloidal dispersions in a nematic liquid crystal introduce a new class of long-range two-particle interactions mediated by the distorted director field. They are of either dipolar or quadrupolar type depending on whether the single particles exhibit the dipole, Saturn-ring or surface-ring configuration. The dipolar forces were verified in an excellent experiment by Poulin et al. [179]. Via the well-known flexoelectric effect [147], strong director distortions in the dipole configuration should induce an electric dipole associated with each particle. It would be interesting to study, both theoretically and experimentally, how this electric dipole contributes to the dipolar force. On the other hand, there exists a strong short-range repulsion between particles due to the presence of a hyperbolic point defect which prevents, e.g., water droplets from coalescing. Even above the nematic-isotropic phase transition, liquid crystals mediate an attractive interaction at a length scale of 10 nm. Its strength is easily controlled by temperature, and it produces an observable effect since it can induce flocculation when the system is close to the phase transition.

To understand colloidal dispersions in nematics in detail, we have performed an extensive study of the three possible director configurations around a single particle. These configurations are ideal objects to investigate the properties of topological point and line defects. The dipolar structure should exhibit a twist in conventional calamitic compounds. The transition from the dipole to the Saturn ring can be controlled, e.g., by a magnetic field which presents a means to access the dynamics of topological defects. Furthermore, we have studied how the strength of surface anchoring influences the director configuration. Surface effects are of considerable importance in display technology, and there is fundamental interest in understanding the coupling between liquid crystal molecules and surfaces. In addition, we have clarified the mechanism due to which the saddle-splay term in the Frank free energy promotes the formation of the

surface-ring structure. The Stokes drag and Brownian motion in nematics have hardly been studied experimentally. Especially the dipole configuration with its vector symmetry presents an appealing object. We have calculated the Stokes drag for a fixed director field. However, we have speculated that for small Ericksen numbers ($Er \ll 1$) flow-induced distortions of the director field result in corrections to the Stokes drag which are of the order of Er. Preliminary studies support this conclusion. Furthermore, for growing Er they reveal a highly non-linear Stokes drag whose consequences seemed to have not been explored in colloidal physics. Finally, we have demonstrated that the dipole, consisting of the spherical particle and its companion point defect, also exists in more complex geometries, and we have studied in detail how it forms.

Acknowledgements

I am grateful to Tom Lubensky, Philippe Poulin and Dave Weitz for their close and inspiring collaboration on nematic emulsions at the University of Pennsylvania which initiated the present work. I thank Anamarija Borštnik, Andreas Rüdinger, Joachim Stelzer, Dieter Ventzki, and Slobodan Žumer for collaborating on different aspects of nematic colloidal dispersions. The results are presented in this review article. A lot of thanks to Eugene Gartland, Thomas Gisler, Randy Kamien, Axel Kilian, R. Klein, G. Maret, R.B. Meyer, Michael Reichenstein, E. Sackmann, Thorsten Seitz, Eugene Terentjev, and H.-R. Trebin for fruitful discussions. Finally, I acknowledge financial assistance from the Deutsche Forschungsgemeinschaft through grants Sta 352/2-1/2 and Tr 154/17-1/2.

References

[1] A.A. Abrikosov, On the magnetic properties of superconductors of the second group, Sov. Phys. JETP 5 (1957) 1174–1182.
[2] A. Ajdari, B. Duplantier, D. Hone, L. Peliti, J. Prost, "Pseudo-Casimir" effect in liquid crystals, J. Phys. II France 2 (1992) 487–501.
[3] A. Ajdari, L. Peliti, J. Prost, Fluctuation-induced long-range forces in liquid crystals, Phys. Rev. Lett. 66 (1991) 1481–1484.
[4] E. Allahyarov, I. D'Amico, H. Löwen, Attraction between like-charged macroions by Coulomb depletion, Phys. Rev. Lett. 81 (1998) 1334–1337.
[5] D.W. Allender, G.P. Crawford, J.W. Doane, Determination of the liquid-crystal surface elastic constant K_{24}, Phys. Rev. Lett. 67 (1991) 1442–1445.
[6] D. Andrienko, G. Germano, M.P. Allen, Computer simulation of topological defects around a colloidal particle or droplet dispersed in a nematic host, Phys. Rev. E., to be published.
[7] R.J. Atkin, Poiseuille flow of liquid crystals of the nematic type, Arch. Rational Mech. Anal. 38 (1970) 224–240.
[8] R.J. Atkin, F.M. Leslie, Couette flow of nematic liquid crystals, Q. J. Mech. Appl. Math. 23 (1970) S3–S24.
[9] G. Barbero, C. Oldano, Derivative-dependent surface-energy terms in nematic liquid crystals, Nuovo Cimento D 6 (1985) 479–493.
[10] J.L. Billeter, R.A. Pelcovits, Defect configurations and dynamical behavior in a Gay-Berne nematic emulsion, Phys. Rev. E 62 (2000) 711–717.
[11] R.B. Bird, W.E. Stewart, E.N. Lightfoot, Transport Phenomena, Wiley, New York, 1960.
[12] C. Blanc, M. Kleman, The confinement of smectics with a strong anchoring, Eur. Phys. J. E., to be published.

[13] G. Blatter, M.V. Feigel'mann, V.B. Geshkenbein, A.I. Larkin, V.M. Vinokur, Vortices in high-temperature superconductors, Rev. Mod. Phys. 66 (1994) 1125–1388.
[14] L.M. Blinov, A.Y. Kabayenkov, A.A. Sonin, Experimental studies of the anchoring energy of nematic liquid crystals, Liq. Cryst. 5 (1989) 645–661.
[15] A. Borštnik, H. Stark, S. Žumer, Interaction of spherical particles dispersed in liquid crystals above the nematic–isotropic phase transition, Phys. Rev. E 60 (4) (1999) 4210–4218. *
[16] A. Borštnik, H. Stark, S. Žumer, Temperature-induced flocculation of colloidal particles immersed into the isotropic phase of a nematic liquid crystal, Phys. Rev. E 61 (3) (2000) 2831–2839. **
[17] A. Borštnik, H. Stark, S. Žumer, Temperature-induced flocculation of colloidal particles above the nematic-isotropic phase transition, Prog. Colloid Polym. Sci. 115 (2000) 353–356.
[18] A. Borštnik, S. Žumer, Forces in an inhomogeneously ordered nematic liquid crystal, Phys. Rev. E 56 (1997) 3021–3027.
[19] A. Böttger, D. Frenkel, E. van de Riet, R. Zijlstra, Diffusion of Brownian particles in the isotropic phase of a nematic liquid crystal, Mol. Cryst. Liq. Cryst. 2 (1987) 539–547. *
[20] W.E. Boyce, R.C. Di Prima, Elementary Differential Equations, Wiley, New York, 1992.
[21] A. Bray, Theory of phase-ordering kinetics, Adv. Phys. 43 (1994) 357–459.
[22] F. Brochard, P.G. de Gennes, Theory of magnetic suspensions in liquid crystals, J. Phys. (Paris) 31 (1970) 691–708. **
[23] R. Bubeck, C. Bechinger, S. Neser, P. Leiderer, Melting and reentrant freezing of two-dimensional colloidal crystals in confined geometry, Phys. Rev. Lett. 82 (1999) 3364–3367.
[24] S.V. Burylov, Y.L. Raikher, Orientation of a solid particle embedded in a monodomain nematic liquid crystal, Phys. Rev. E 50 (1994) 358–367.
[25] H.B. Callen, Thermodynamics and an Introduction to Thermostatistics, 2nd Edition, Wiley, New York, 1985.
[26] S. Candau, P.L. Roy, F. Debeauvais, Magnetic field effects in nematic and cholesteric droplets suspended in an isotropic liquid, Mol. Cryst. Liq. Cryst. 23 (1973) 283–297.
[27] P. Chaikin, T.C. Lubensky, Principles of Condensed Matter Physics, Cambridge University Press, Cambridge, 1995.
[28] S. Chandrasekhar, Stochastic problems in physics and astronomy, Rev. Mod. Phys. 15 (1943) 1–89.
[29] S. Chandrasekhar, Liquid Crystals, 2nd Edition, Cambridge University Press, Cambridge, 1992.
[30] S. Chandrasekhar, G. Ranganath, The structure and energetics of defects in liquid crystals, Adv. Phys. 35 (1986) 507–596.
[31] S.-H. Chen, N.M. Amer, Observation of macroscopic collective behavior and new texture in magnetically doped liquid crystals, Phys. Rev. Lett. 51 (1983) 2298–2301.
[32] S. Chono, T. Tsuji, Numerical simulation of nematic liquid crystalline flows around a circular cylinder, Mol. Cryst. Liq. Cryst. 309 (1998) 217–236.
[33] A.J. Chorin, A numerical method for solving incompressible viscous flow problems, J. Comput. Phys. 2 (1967) 12–26.
[34] I. Chuang, R. Durrer, N. Turok, B. Yurke, Cosmology in the laboratory: defect dynamics in liquid crystals, Science 251 (1991) 1336–1342.
[35] P.E. Cladis, M. Kléman, Non-singular disclinations of strength $S=+1$ in nematics, J. Phys. (Paris) 33 (1972) 591–598.
[36] P.E. Cladis, M. Kléman, P. Piéranski, Sur une nouvelle méthode de décoration de la mésomorphe du *p*, *n*-méthoxybenzilidène *p*-bétylaniline (MBBA), C. R. Acad. Sci. Ser. B 273 (1971) 275–277.
[37] P.E. Cladis, W. van Saarloos, P.L. Finn, A.R. Kortan, Dynamics of line defects in nematic liquid crystals, Phys. Rev. Lett. 58 (1987) 222–225.
[38] H.J. Coles, Laser and electric field induced birefringence studies on the cyanobiphenyl homologues, Mol. Cryst. Liq. Cryst. Lett. 49 (1978) 67–74.
[39] P. Collings, Private communication, 1995.
[40] G.P. Crawford, D.W. Allender, J.W. Doane, Surface elastic and molecular-anchoring properties of nematic liquid crystals confined to cylindrical cavities, Phys. Rev. A 45 (1992) 8693–8708.
[41] G.P. Crawford, D.W. Allender, J.W. Doane, M. Vilfan, I. Vilfan, Finite molecular anchoring in the escaped-radial nematic configuration: A ^{2}H-NMR study, Phys. Rev. A 44 (1991) 2570–2576.

[42] G.P. Crawford, R. Ondris-Crawford, S. Žumer, J.W. Doane, Anchoring and orientational wetting transitions of confined liquid crystals, Phys. Rev. Lett. 70 (1993) 1838–1841.
[43] G.P. Crawford, R.J. Ondris-Crawford, J.W. Doane, S. Žumer, Systematic study of orientational wetting and anchoring at a liquid-crystal–surfactant interface, Phys. Rev. E 53 (1996) 3647–3661.
[44] G.P. Crawford, S. Žumer (Eds.), Liquid Crystals in Complex Geometries, Taylor & Francis, London, 1996.
[45] J.C. Crocker, D.G. Grier, When like charges attract: The effects of geometrical confinement on long-range colloidal interactions, Phys. Rev. Lett. 77 (1996) 1897–1900.
[46] P.K. Currie, Couette flow of a nematic liquid crystal in the presence of a magnetic field, Arch. Rational Mech. Anal. 37 (1970) 222–242.
[47] P.K. Currie, Apparent viscosity during viscometric flow of nematic liquid crystals, J. Phys. (Paris) 40 (1979) 501–505.
[48] P.G. de Gennes, Short range order effects in the isotropic phase of nematics and cholesterics, Mol. Cryst. Liq. Cryst. 12 (1971) 193–214.
[49] P.G. de Gennes, Nematodynamics, in: R. Balian, G. Weill (Eds.), Molecular Fluids, Gordon and Breach, London, 1976, pp. 373–400.
[50] P.G. de Gennes, Interactions between solid surfaces in a presmectic fluid, Langmuir 6 (1990) 1448–1450.
[51] P.G. de Gennes, J. Prost, The Physics of Liquid Crystals, 2nd Edition, International Series of Monographs on Physics, Vol. 83, Oxford Science, Oxford, 1993.
[52] S.R. de Groot, Thermodynamics of Irreversible Processes, Selected Topics in Modern Physics, North-Holland, Amsterdam, 1951.
[53] B.V. Derjaguin, Friction and adhesion. IV: The theory of adhesion of small particles, Kolloid Z. 69 (1934) 155–164.
[54] B.V. Derjaguin, L. Landau, Theory of the stability of strongly charged lyophobic sols and the adhesion of strongly charged particles in solutions of electrolytes, Acta Physicochim. URSS 14 (1941) 633–662.
[55] A.D. Dinsmore, D.T. Wong, P. Nelson, A.G. Yodh, Hard spheres in vesicles: Curvature-induced forces and particle-induced curvature, Phys. Rev. Lett. 80 (1998) 409–412.
[56] A.D. Dinsmore, A.G. Yodh, D.J. Pine, Entropic control of particle motion using passive surface microstructures, Nature 383 (1996) 239–244.
[57] A.C. Diogo, Friction drag on a sphere moving in a nematic liquid crystal, Mol. Cryst. Liq. Cryst. 100 (1983) 153–165.
[58] J.W. Doane, N.A. Vaz, B.G. Wu, S. Žumer, Field controlled light scattering from nematic microdroplets, Appl. Phys. Lett. 48 (1986) 269–271.
[59] I. Dozov, Private communication, 1999.
[60] P.S. Drzaic, Liquid Crystal Dispersions, Series on Liquid Crystals, Vol. 1, World Scientific, Singapore, 1995.
[61] E. Dubois-Violette, O. Parodi, Émulsions nématiques. Effects de champ magnétiques et effets piézoélectriques, J. Phys. (Paris) Coll. C4 30 (1969) 57–64.
[62] R. Eidenschink, W.H. de Jeu, Static scattering in filled nematic: new liquid crystal display technique, Electron. Lett. 27 (1991) 1195. ∗
[63] A. Einstein, Über die von der molekularkinetischen Theorie der Wärme geforderte Bewegung von in ruhenden Flüssigkeiten suspendierten Teilchen, Ann. Phys. (Leipzig) 17 (1905) 549–560.
[64] A. Einstein, Eine neue Bestimmung der Moleküldimensionen, Ann. Phys. (Leipzig) 19 (1906) 289–306.
[65] A. Einstein, Zur Theorie der Brownschen Bewegung, Ann. Phys. (Leipzig) 19 (1906) 371–381.
[66] J.H. Erdmann, S. Žumer, J.W. Doane, Configuration transition in a nematic liquid crystal confined to a small spherical cavity, Phys. Rev. Lett. 64 (1990) 1907–1910.
[67] J.L. Ericksen, Anisotropic fluids, Arch. Rational Mech. Anal. 4 (1960) 231–237.
[68] J.L. Ericksen, Theory of anisotropic fluids, Trans. Soc. Rheol. 4 (1960) 29–39.
[69] J.L. Ericksen, Conservation laws of liquid crystals, Trans. Soc. Rheol. 5 (1961) 23–34.
[70] J.L. Ericksen, Continuum theory of liquid crystals, Appl. Mech. Rev. 20 (1967) 1029–1032.
[71] J.L. Ericksen, Continuum theory of liquid crystals of nematic type, Mol. Cryst. Liq. Cryst. 7 (1969) 153–164.
[72] A.C. Eringen (Ed.), Continuum Physics: Vols. I–IV, Academic Press, New York, 1976.
[73] A.C. Eringen, C.B. Kafadar, Part I: Polar field theories, in: A.C. Eringen (Ed.), Continuum Physics: Polar and Nonlocal Field Theories, Vol. IV, Academic Press, New York, 1976, pp. 1–73.

[74] J. Fang, E. Teer, C.M. Knobler, K.-K. Loh, J. Rudnick, Boojums and the shapes of domains in monolayer films, Phys. Rev. E 56 (1997) 1859–1868.
[75] A.M. Figueiredo Neto, M.M.F. Saba, Determination of the minimum concentration of ferrofluid required to orient nematic liquid crystals, Phys. Rev. A 34 (1986) 3483–3485.
[76] D. Forster, Hydrodynamic Fluctuations, Broken Symmetry, and Correlation Functions, Frontiers in Physics: A Lecture Note and Reprint Series, Vol. 47, W.A. Benjamin, Massachusetts, 1975.
[77] D. Forster, T. Lubensky, P. Martin, J. Swift, P. Pershan, Hydrodynamics of liquid crystals, Phys. Rev. Lett. 26 (1971) 1016–1019.
[78] S. Fraden, Phase transitions in colloidal suspensions of virus particles, in: M. Baus, L.F. Rull, J.P. Ryckaert (Eds.), Observation, Prediction, and Simulation of Phase Transitions in Complex Fluids, NATO Advanced Studies Institute Series C: Mathematical and Physical Sciences, Vol. 460, Kluwer, Dordrecht, 1995, pp. 113–164.
[79] F.C. Frank, I. Liquid Crystals: On the theory of liquid crystals, Discuss. Faraday Soc. 25 (1958) 19–28.
[80] G. Friedel, F. Grandjean, Observation géométriques sur les liquides á coniques focales, Bull. Soc. Fr. Mineral 33 (1910) 409–465.
[81] G. Friedel, Dislocations, Pergamon Press, Oxford, 1964.
[82] N. Fuchs, Über die Stabilität und Aufladung der Aerosole, Z. Phys. 89 (1934) 736–743.
[83] J. Fukuda, H. Yokoyama, Director configuration and dynamics of a nematic liquid crystal around a spherical particle: numerical analysis using adaptive grids, Eur. Phys. J. E., to be published. *
[84] C. Gähwiller, Direct determination of the five independent viscosity coefficients of nematic liquid crystals, Mol. Cryst. Liq. Cryst. 20 (1973) 301–318.
[85] P. Galatola, J.B. Fournier, Nematic-wetted colloids in the isotropic phase, Mol. Cryst. Liq. Cryst. 330 (1999) 535–539.
[86] A. Garel, Boundary conditions for textures and defects, J. Phys. (Paris) 39 (1978) 225–229.
[87] E.C. Gartland, Private communication, 1998.
[88] E.C. Gartland, S. Mkaddem, Instability of radial hedgehog configurations in nematic liquid crystals under Landau–de Gennes free-energy models, Phys. Rev. E 59 (1999) 563–567.
[89] A.P. Gast, W.B. Russel, Simple ordering in complex fluids, Phys. Today 51 (1998) 24–30.
[90] A.P. Gast, C.F. Zukoski, Electrorheological fluids as colloidal suspensions, Adv. Colloid Interface Sci. 30 (1989) 153–202.
[91] A. Glushchenko, H. Kresse, V. Reshetnyak, Yu. Reznikov, O. Yaroshchuk, Memory effect in filled nematic liquid crystals, Liq. Cryst. 23 (1997) 241–246.
[92] J. Goldstone, Field theories with "superconductor" solutions, Nuovo Cimento 19 (1) (1961) 154–164.
[93] J. Goldstone, A. Salam, S. Weinberg, Broken symmetries, Phys. Rev. 127 (1962) 965–970.
[94] J.W. Goodby, M.A. Waugh, S.M. Stein, E. Chin, R. Pindak, J.S. Patel, Characterization of a new helical smectic liquid crystal, Nature 337 (1989) 449–452.
[95] J.W. Goodby, M.A. Waugh, S.M. Stein, E. Chin, R. Pindak, J.S. Patel, A new molecular ordering in helical liquid crystals, J. Am. Chem. Soc. 111 (1989) 8119–8125.
[96] E. Gramsbergen, L. Longa, W.H. de Jeu, Landau theory of the nematic–isotropic phase transition, Phys. Rep. 135 (1986) 195–257.
[97] Y. Gu, N.L. Abbott, Observation of saturn-ring defects around solid microspheres in nematic liquid crystals, Phys. Rev. Lett. 85 (2000) 4719–4722. **
[98] M.J. Guardalben, N. Jain, Phase-shift error as a result of molecular alignment distortions in a liquid–crystal point-diffraction interferometer, Opt. Lett. 25 (2000) 1171–1173.
[99] Groupe d'Etude des Cristaux Liquides, Dynamics of fluctuations in nematic liquid crystals, J. Chem. Phys. 51 (1969) 816–822.
[100] P. Hänggi, P. Talkner, M. Borkovec, Reaction-rate theory: Fifty years after Kramers, Rev. Mod. Phys. 62 (1990) 251–341.
[101] I. Haller, W.R. Young, G.L. Gladstone, D.T. Teaney, Crown ether complex salts as conductive dopants for nematic liquids, Mol. Cryst. Liq. Cryst. 24 (1973) 249–258.
[102] W. Helfrich, Capillary flow of cholesteric and smectic liquid crystals, Phys. Rev. Lett. 23 (1969) 372–374.

[103] G. Heppke, D. Krüerke, M. Müller, Surface anchoring of the discotic cholesteric phase of chiral pentayne systems, in: Abstract Book, Vol. 24, Freiburger Arbeitstagung Flüssigkristalle, Freiburg, Germany, 1995.
[104] H. Heuer, H. Kneppe, F. Schneider, Flow of a nematic liquid crystal around a cylinder, Mol. Cryst. Liq. Cryst. 200 (1991) 51–70.
[105] H. Heuer, H. Kneppe, F. Schneider, Flow of a nematic liquid crystal around a sphere, Mol. Cryst. Liq. Cryst. 214 (1992) 43–61.
[106] R.G. Horn, J.N. Israelachvili, E. Perez, Forces due to structure in a thin liquid crystal film, J. Phys. (Paris) 42 (1981) 39–52.
[107] H. Imura, K. Okano, Friction coefficient for a moving disclination in a nematic liquid crystal, Phys. Lett. A 42 (1973) 403–404.
[108] A. Jákli, L. Almásy, S. Borbély, L. Rosta, Memory of silica aggregates dispersed in smectic liquid crystals: Effect of the interface properties, Eur. Phys. J. B 10 (1999) 509–513.
[109] G.M. Kepler, S. Fraden, Attractive potential between confined colloids at low ionic strength, Phys. Rev. Lett. 73 (1994) 356–359.
[110] R. Klein, Interacting brownian particles – the dynamics of colloidal suspensions, in: F. Mallamace, H.E. Stanley (Eds.), The Physics of Complex Systems, IOS Press, Amsterdam, 1997, pp. 301–345.
[111] M. Kléman, Points, Lines and Walls: in Liquid Crystals, Magnetic Systems, and Various Ordered Media, Wiley, New York, 1983.
[112] H. Kneppe, F. Schneider, B. Schwesinger, Axisymmetrical flow of a nematic liquid crystal around a sphere, Mol. Cryst. Liq. Cryst. 205 (1991) 9–28.
[113] K. Kočevar, R. Blinc, I. Muševič, Atomic force microscope evidence for the existence of smecticlike surface layers in the isotropic phase of a nematic liquid crystal, Phys. Rev. E 62 (2000) R3055–R3058. ∗
[114] S. Komura, R.J. Atkin, M.S. Stern, D.A. Dunmur, Numerical analysis of the radial–axial structure transition with an applied field in a nematic droplet, Liq. Cryst. 23 (1997) 193–203.
[115] S. Kralj, S. Žumer, Fréedericksz transitions in supra-μm nematic droplets, Phys. Rev. A 45 (1992) 2461–2470.
[116] M. Krech, The Casimir Effect in Critical Systems, World Scientific, Singapore, 1994.
[117] M. Kreuzer, R. Eidenschink, Filled nematics, in: G.P. Crawford, S. Žumer (Eds.), Liquid Crystals in Complex Geometries, Taylor & Francis, London, 1996, pp. 307–324.
[118] M. Kreuzer, T. Tschudi, R. Eidenschink, Erasable optical storage in bistable liquid crystal cells, Mol. Cryst. Liq. Cryst. 223 (1992) 219–227. ∗
[119] O.V. Kuksenok, R.W. Ruhwandl, S.V. Shiyanovskii, E.M. Terentjev, Director structure around a colloid particle suspended in a nematic liquid crystal, Phys. Rev. E 54 (1996) 5198–5203. ∗∗
[120] M. Kurik, O. Lavrentovich, Negative-positive monopole transitions in cholesteric liquid crystals, JETP Lett. 35 (1982) 444–447.
[121] M.V. Kurik, O.D. Lavrentovich, Defects in liquid crystals: Homotopy theory and experimental studies, Sov. Phys. Usp. 31 (1988) 196–224.
[122] E. Kuss, pVT-data and viscosity-pressure behavior of MBBA and EBBA, Mol. Cryst. Liq. Cryst. 47 (1978) 71–83.
[123] L.D. Landau, E.M. Lifschitz, Electrodynamics of Continuous Media, Course of Theoretical Physics, Vol. 8, Pergamon Press, Oxford, first English Edition, 1960.
[124] L.D. Landau, E.M. Lifschitz, Statistische Physik, Teil 1, Lehrbuch der Theoretischen Physik, Vol. 5, 6th Edition, Akademie, Berlin, 1984.
[125] A.E. Larsen, D.G. Grier, Like-charge attractions in metastable colloidal crystallites, Nature 385 (1997) 230–233.
[126] O. Lavrentovich, E. Terentév, Phase transition altering the symmetry of topological point defects (hedgehogs) in a nematic liquid crystal, Sov. Phys. JETP 64 (1986) 1237–1244.
[127] O.D. Lavrentovich, Topological defects in dispersed liquid crystals, or words and worlds around liquid crystal drops, Liq. Cryst. 24 (1998) 117–125.
[128] F.M. Leslie, Some constitutive equations for anisotropic fluids, Quart. J. Mech. Appl. Math. 19 (1966) 357–370.
[129] F.M. Leslie, Some constitutive equations for liquid crystals, Arch. Rational Mech. Anal. 28 (1968) 265–283.

[130] B.I. Lev, P.M. Tomchuk, Interaction of foreign macrodroplets in a nematic liquid crystal and induced supermolecular structures, Phys. Rev. E 59 (1999) 591–602.
[131] S. Lifson, J.L. Jackson, On the self-diffusion of ions in a polyelectrolyte solution, J. Chem. Phys. 36 (1962) 2410–2414.
[132] D. Link, N. Clark, Private communication, 1997.
[133] J. Liu, E.M. Lawrence, A. Wu, M.L. Ivey, G.A. Flores, K. Javier, J. Bibette, J. Richard, Field-induced structures in ferrofluid emulsions, Phys. Rev. Lett. 74 (1995) 2828–2831.
[134] H. Löwen, Kolloide – auch für Physiker interessant, Phys. Bl. 51 (3) (1995) 165–168.
[135] H. Löwen, Solvent-induced phase separation in colloidal fluids, Phys. Rev. Lett. 74 (1995) 1028–1031.
[136] H. Löwen, Phase separation in colloidal suspensions induced by a solvent phase transition, Z. Phys. B 97 (1995) 269–279.
[137] J.-C. Loudet, P. Barois, P. Poulin, Colloidal ordering from phase separation in a liquid-crystalline continuous phase, Nature 407 (2000) 611–613. **
[138] T.C. Lubensky, Molecular description of nematic liquid crystals, Phys. Rev. A 2 (1970) 2497–2514.
[139] T.C. Lubensky, Hydrodynamics of cholesteric liquid crystals, Phys. Rev. A 6 (1972) 452–470.
[140] T.C. Lubensky, D. Pettey, N. Currier, H. Stark, Topological defects and interactions in nematic emulsions, Phys. Rev. E 57 (1998) 610–625. ***
[141] I.F. Lyuksyutov, Topological instability of singularities at small distances in nematics, Sov. Phys. JETP 48 (1978) 178–179.
[142] W. Maier, A. Saupe, Eine einfache molekular-statistische Theorie der nematischen kristallinflüssigen Phase. Teil I, Z. Naturforsch. Teil A 14 (1959) 882–889.
[143] S.P. Meeker, W.C.K. Poon, J. Crain, E.M. Terentjev, Colloid-liquid-crystal composites: An unusual soft solid, Phys. Rev. E 61 (2000) R6083–R6086. **
[144] S. Meiboom, M. Sammon, W.F. Brinkman, Lattice of disclinations: The structure of the blue phases of cholesteric liquid crystals, Phys. Rev. A 27 (1983) 438–454.
[145] N. Mermin, Surface singularities and superflow in ^{3}He-A, in: S.B. Trickey, E.D. Adams, J.W. Dufty (Eds.), Quantum Fluids and Solids, Plenum Press, New York, 1977, pp. 3–22.
[146] N.D. Mermin, The topological theory of defects in ordered media, Rev. Mod. Phys. 51 (1979) 591–648.
[147] R.B. Meyer, Piezoelectric effects in liquid crystals, Phys. Rev. Lett. 22 (1969) 918–921.
[148] R.B. Meyer, Point disclinations at a nematic-isotropic liquid interface, Mol. Cryst. Liq. Cryst. 16 (1972) 355–369. *
[149] R.B. Meyer, On the existence of even indexed disclinations in nematic liquid crystals, Philos. Mag. 27 (1973) 405–424.
[150] M. Mięsovicz, Influence of a magnetic field on the viscosity of para-azoxyanisol, Nature 136 (1935) 261.
[151] Mięsowicz, The three coefficients of viscosity of anisotropic liquids, Nature 158 (1946) 27.
[152] V.P. Mineev, Topologically stable defects and solitons in ordered media, in: I.M. Khalatnikov (Ed.), Soviet Scientific Reviews, Section A: Physics Reviews, Vol. 2, Harwood, London, 1980, pp. 173–246.
[153] O. Mondain-Monval, J.C. Dedieu, T. Gulik-Krzywicki, P. Poulin, Weak surface energy in nematic dispersions: saturn ring defects and quadrupolar interactions, Eur. Phys. J. B 12 (1999) 167–170. **
[154] L. Moreau, P. Richetti, P. Barois, Direct measurement of the interaction between two ordering surfaces confining a presmectic film, Phys. Rev. Lett. 73 (1994) 3556–3559.
[155] H. Mori, H. Nakanishi, On the stability of topologically non-trivial point defects, J. Phys. Soc. Japan 57 (1988) 1281–1286.
[156] A.H. Morrish, The Physical Principles of Magnetism, Wiley Series on the Science and Technology of Materials, Wiley, New York, 1965.
[157] V.M. Mostepanenko, N.N. Trunov, The Casimir Effect and its Application, Clarendon Press, Oxford, 1997.
[158] I. Muševič, G. Slak, R. Blinc, Observation of critical forces in a liquid crystal by an atomic force microscope, in: Proceedings of the 16th International Liquid Crystal Conference, Abstract Book, Kent, USA, 1996, p. 91.
[159] I. Muševič, G. Slak, R. Blinc, Temperature controlled microstage for an atomic force microscope, Rev. Sci. Instrum. 67 (1996) 2554–2556.
[160] F.R.N. Nabarro, Theory of Crystal Dislocations, The International Series of Monographs on Physics, Clarendon Press, Oxford, 1967.

[161] H. Nakanishi, K. Hayashi, H. Mori, Topological classification of unknotted ring defects, Commun. Math. Phys. 117 (1988) 203–213.
[162] D.H. Napper, Polymeric Stabilization of Colloidal Dispersions, Colloid Science, Vol. 3, Academic Press, London, 1983.
[163] J. Nehring, A. Saupe, On the elastic theory of uniaxial liquid crystals, J. Chem. Phys. 54 (1971) 337–343.
[164] D.R. Nelson, Defect-mediated Phase Transitions, in: C. Domb, J. Lebowitz (Eds.), Phase Transitions and Critical Phenomena, Vol. 7, Academic Press, New York, 1983, pp. 1–99.
[165] M. Nobili, G. Durand, Disorientation-induced disordering at a nematic-liquid-crystal–solid interface, Phys. Rev. A 46 (1992) R6174–R6177.
[166] C. Oldano, G. Barbero, An ab initio analysis of the second-order elasticity effect on nematic configurations, Phys. Lett. 110A (1985) 213–216.
[167] C.W. Oseen, The theory of liquid crystals, Trans. Faraday Soc. 29 (1933) 883–899.
[168] M.A. Osipov, S. Hess, The elastic constants of nematic discotic liquid crystals with perfect local orientational order, Mol. Phys. 78 (1993) 1191–1201.
[169] S. Ostlund, Interactions between topological point singularities, Phys. Rev. E 24 (1981) 485–488.
[170] O. Parodi, Stress Tensor for a nematic liquid crystal, J. Phys. (Paris) 31 (1970) 581–584.
[171] E. Penzenstadler, H.-R. Trebin, Fine structure of point defects and soliton decay in nematic liquid crystals, J. Phys. France 50 (1989) 1027–1040.
[172] V.M. Pergamenshchik, Surfacelike-elasticity-induced spontaneous twist deformations and long-wavelength stripe domains in a hybrid nematic layer, Phys. Rev. E 47 (1993) 1881–1892.
[173] V.M. Pergamenshchik, P.I. Teixeira, T.J. Sluckin, Distortions induced by the k_{13} surfacelike elastic term in a thin nematic liquid-crystal film, Phys. Rev. E 48 (1993) 1265–1271.
[174] V.M. Pergamenshchik, K_{13} term and effective boundary condition for the nematic director, Phys. Rev. E 58 (1998) R16–R19.
[175] D. Pettey, T.C. Lubensky, D. Link, Topological inclusions in 2D smectic C films, Liq. Cryst. 25 (1998) 579–587. ∗
[176] P. Pieranski, F. Brochard, E. Guyon, Static and dynamic behavior of a nematic liquid crystal in a magnetic field. Part II: Dynamics, J. Phys. (Paris) 34 (1973) 35–48.
[177] A. Poniewierski, T. Sluckin, Theory of the nematic-isotropic transition in a restricted geometry, Liq. Cryst. 2 (1987) 281–311.
[178] P. Poulin, Private communication, 1999.
[179] P. Poulin, V. Cabuil, D.A. Weitz, Direct measurement of colloidal forces in an anisotropic solvent, Phys. Rev. Lett. 79 (1997) 4862–4865. ∗∗
[180] P. Poulin, N. Francès, O. Mondain-Monval, Suspension of spherical particles in nematic solutions of disks and rods, Phys. Rev. E 59 (1999) 4384–4387. ∗
[181] P. Poulin, V.A. Raghunathan, P. Richetti, D. Roux, On the dispersion of latex particles in a nematic solution. I. Experimental evidence and a simple model, J. Phys. II France 4 (1994) 1557–1569. ∗
[182] P. Poulin, H. Stark, T.C. Lubensky, D.A. Weitz, Novel colloidal interactions in anisotropic fluids, Science 275 (1997) 1770–1773. ∗∗∗
[183] P. Poulin, D.A. Weitz, Inverted and multiple emulsions, Phys. Rev. E 57 (1998) 626–637. ∗∗∗
[184] P. Poulin, Novel phases and colloidal assemblies in liquid crystals, Curr. Opinion in Colloid & Interface Science 4 (1999) 66–71.
[185] M.J. Press, A.S. Arrott, Theory and experiment of configurations with cylindrical symmetry in liquid-crystal droplets, Phys. Rev. Lett. 33 (1974) 403–406.
[186] M.J. Press, A.S. Arrott, Elastic energies and director fields in liquid crystal droplets, I. Cylindrical symmetry, J. Phys. (Paris) Coll. C1 36 (1975) 177–184.
[187] W.H. Press, S.A. Teukolsky, W.T. Vetterling, B.P. Flannery, Numerical Recipes in Fortran: The Art of Scientific Computing, Cambridge University Press, Cambridge, 1992.
[188] V.A. Raghunathan, P. Richetti, D. Roux, Dispersion of latex particles in a nematic solution. II. Phase diagram and elastic properties, Langmuir 12 (1996) 3789–3792.
[189] V.A. Raghunathan, P. Richetti, D. Roux, F. Nallet, A.K. Sood, Colloidal dispersions in a liquid-crystalline medium, Mol. Cryst. Liq. Cryst. 288 (1996) 181–187.

[190] S. Ramaswamy, R. Nityananda, V.A. Raghunathan, J. Prost, Power-law forces between particles in a nematic, Mol. Cryst. Liq. Cryst. 288 (1996) 175–180. **
[191] J. Rault, Sur une méthode nouvelle d'étude de l'orientation moléculaire á la surface d'un cholestérique, C. R. Acad. Sci. Ser. B 272 (1971) 1275–1276.
[192] M. Reichenstein, T. Seitz, H.-R. Trebin, Numerical simulations of three dimensional liquid crystal cells, Mol. Cryst. Liq. Cryst. 330 (1999) 549–555.
[193] S.R. Renn, T.C. Lubensky, Abrikosov dislocation lattice in a model of the cholesteric–to–smectic-A transition, Phys. Rev. A 38 (1988) 2132–2147.
[194] V.G. Roman, E.M. Terentjev, Effective viscosity and diffusion tensor of an anisotropic suspension or mixture, Colloid J. USSR 51 (1989) 435–442.
[195] R. Rosso, E.G. Virga, Metastable nematic hedgehogs, J. Phys. A 29 (1996) 4247–4264.
[196] D. Rudhardt, C. Bechinger, P. Leiderer, Direct measurement of depletion potentials in mixtures of colloids and nonionic polymers, Phys. Rev. Lett. 81 (1998) 1330–1333.
[197] A. Rüdinger, H. Stark, Twist transition in nematic droplets: A stability analysis, Liq. Cryst. 26 (1999) 753–758.
[198] R.W. Ruhwandl, E.M. Terentjev, Friction drag on a cylinder moving in a nematic liquid crystal, Z. Naturforsch. Teil A 50 (1995) 1023–1030.
[199] R.W. Ruhwandl, E.M. Terentjev, Friction drag on a particle moving in a nematic liquid crystal, Phys. Rev. E 54 (1996) 5204–5210. **
[200] R.W. Ruhwandl, E.M. Terentjev, Long-range forces and aggregation of colloid particles in a nematic liquid crystal, Phys. Rev. E 55 (1997) 2958–2961. *
[201] R.W. Ruhwandl, E.M. Terentjev, Monte Carlo simulation of topological defects in the nematic liquid crystal matrix around a spherical colloid particle, Phys. Rev. E 56 (1997) 5561–5565. **
[202] W.B. Russel, D.A. Saville, W.R. Schowalter, Colloidal Dispersions, Cambridge University Press, Cambridge, 1995.
[203] G. Ryskin, M. Kremenetsky, Drag force on a line defect moving through an otherwise undisturbed field: Disclination line in a nematic liquid crystal, Phys. Rev. Lett. 67 (1991) 1574–1577.
[204] S.D. Sarma, A. Pinczuk (Eds.), Perspectives in Quantum Hall Fluids, Wiley, New York, 1997.
[205] M. Schadt, Optisch strukturierte Flüssigkristall-Anzeigen mit großem Blickwinkelbereich, Phys. Bl. 52 (7/8) (1996) 695–698.
[206] M. Schadt, H. Seiberle, A. Schuster, Optical patterning of multi-domain liquid-crystal displays with wide viewing angles, Nature 318 (1996) 212–215.
[207] N. Schopohl, T.J. Sluckin, Defect core structure in nematic liquid crystals, Phys. Rev. Lett. 59 (1987) 2582–2584.
[208] N. Schopohl, T.J. Sluckin, Hedgehog structure in nematic and magnetic systems, J. Phys. France 49 (1988) 1097–1101.
[209] V. Sequeira, D.A. Hill, Particle suspensions in liquid crystalline media: Rheology, structure, and dynamic interactions, J. Rheol. 42 (1998) 203–213.
[210] P. Sheng, Phase transition in surface-aligned nematic films, Phys. Rev. Lett. 37 (1976) 1059–1062.
[211] P. Sheng, Boundary-layer phase transition in nematic liquid crystals, Phys. Rev. A 26 (1982) 1610–1617.
[212] P. Sheng, E.B. Priestly, The Landau–de Gennes theory of liquid crystal phase transition, in: E.B. Priestly, P.J. Wojtowicz, P. Sheng (Eds.), Introduction to Liquid Crystals, Plenum Press, New York, 1979, pp. 143–201.
[213] S.V. Shiyanovskii, O.V. Kuksenok, Structural transitions in nematic filled with colloid particles, Mol. Cryst. Liq. Cryst. 321 (1998) 45–56.
[214] R. Sigel, G. Strobl, Static and dynamic light scattering from the nematic wetting layer in an isotropic crystal, Prog. Colloid Polym. Sci. 104 (1997) 187–190.
[215] M. Smoluchowski, Versuch einer mathematischen Theorie der Koagulationkinetik kolloider Lösungen, Z. Phys. Chem. (Leipzig) 92 (1917) 129–168.
[216] K. Sokalski, T.W. Ruijgrok, Elastic constants for liquid crystals of disc-like molecules, Physica A 113A (1982) 126–132.
[217] A. Sommerfeld, Vorlesungen über Theoretische Physik II. Mechanik der deformierbaren Medien, 6th Edition, Verlag Harri Deutsch, Frankfurt, 1978.

[218] A. Sonnet, A. Kilian, S. Hess, Alignment tensor versus director: Description of defects in nematic liquid crystals, Phys. Rev. E 52 (1995) 718–722.
[219] H. Stark, Director field configurations around a spherical particle in a nematic liquid crystal, Eur. Phys. J. B 10 (1999) 311–321. **
[220] H. Stark, J. Stelzer, R. Bernhard, Water droplets in a spherically confined nematic solvent: A numerical investigation, Eur. Phys. J. B 10 (1999) 515–523. *
[221] J. Stelzer, M.A. Bates, L. Longa, G.R. Luckhurst, Computer simulation studies of anisotropic systems. XXVII. The direct pair correlation function of the Gay–Berne discotic nematic and estimates of its elastic constants, J. Chem. Phys. 107 (1997) 7483–7492.
[222] K.J. Strandburg, Two-dimensional melting, Rev. Mod. Phys. 60 (1988) 161–207.
[223] B.D. Swanson, L.B. Sorenson, What forces bind liquid crystal, Phys. Rev. Lett. 75 (1995) 3293–3296.
[224] G.I. Taylor, The mechanism of plastic deformation of crystals, Proc. R. Soc. London, Ser. A 145 (1934) 362–415.
[225] E.M. Terentjev, Disclination loops, standing alone and around solid particles, in nematic liquid crystals, Phys. Rev. E 51 (1995) 1330–1337. **
[226] H.-R. Trebin, The topology of non-uniform media in condensed matter physics, Adv. Phys. 31 (1982) 195–254.
[227] E.H. Twizell, Computational Methods for Partial Differential Equations, Chichester, Horwood, 1984.
[228] D. Ventzki, H. Stark, Stokes drag of particles suspended in a nematic liquid crystal, in preparation.
[229] E.J.W. Verwey, J.T.G. Overbeek, Theory of the Stability of Lyophobic Colloids, Elsevier, Amsterdam, 1948.
[230] D. Vollhardt, P. Wölfle, The Phases of Helium 3, Taylor & Francis, New York, 1990.
[231] G.E. Volovik, O.D. Lavrentovich, Topological dynamics of defects: Boojums in nematic drops, Sov. Phys. JETP 58 (1983) 1159–1168.
[232] T.W. Warmerdam, D. Frenkel, R.J.J. Zijlstra, Measurements of the ratio of the Frank constants for splay and bend in nematics consisting of disc-like molecules—2,3,6,7,10,11-hexakis(*p*-alkoxybenzoyloxy)triphenylenes, Liq. Cryst. 3 (1988) 369–380.
[233] Q.-H. Wei, C. Bechinger, D. Rudhardt, P. Leiderer, Experimental study of laser-induced melting in two-dimensional colloids, Phys. Rev. Lett. 81 (1998) 2606–2609.
[234] A.E. White, P.E. Cladis, S. Torza, Study of liquid crystals in flow: I. Conventional viscometry and density measurements, Mol. Cryst. Liq. Cryst. 43 (1977) 13–31.
[235] J. Wilks, D. Betts, An Introduction to Liquid Helium, Clarendon Press, Oxford, 1987.
[236] C. Williams, P. Pierański, P.E. Cladis, Nonsingular $S = +1$ screw disclination lines in nematics, Phys. Rev. Lett. 29 (1972) 90–92.
[237] R.D. Williams, Two transitions in tangentially anchored nematic droplets, J. Phys. A 19 (1986) 3211–3222.
[238] K. Zahn, R. Lenke, G. Maret, Two-stage melting of paramagnetic colloidal crystals in two dimensions, Phys. Rev. Lett. 82 (1999) 2721–2724.
[239] M. Zapotocky, L. Ramos, P. Poulin, T.C. Lubensky, D.A. Weitz, Particle-stabilized defect gel in cholesteric liquid crystals, Science 283 (1999) 209–212. **
[240] P. Ziherl, R. Podgornik, S. Žumer, Casimir force in liquid crystals close to the nematic-isotropic phase transition, Chem. Phys. Lett. 295 (1998) 99–104.
[241] J. Zinn-Justin, Quantum Field Theory and Critical Phenomena, 3rd Edition, International Series of monographs on Physics, Vol. 92, Oxford Science, Oxford, 1996.
[242] H. Zöcher, The effect of a magnetic field on the nematic state, Trans. Faraday Soc. 29 (1933) 945–957.